

REPORT DOCUMENTATION PAGE				Form Approved OMB No. 0704-0188	
Public reporting burden for this collection of information is estimated to average 1 hour per response, including the time for reviewing instructions, searching existing data sources, gathering and maintaining the data needed, and completing and reviewing the collection of information. Send comments regarding this burden estimate or any other aspect of this collection of information, including suggestions for reducing the burden, to Department of Defense, Washington Headquarters Services, Directorate for Information Operations and Reports (0704-0188), 1215 Jefferson Davis Highway, Suite 1204, Arlington, VA 22202-4302. Respondents should be aware that notwithstanding any other provision of law, no person shall be subject to any penalty for failing to comply with a collection of information if it does not display a currently valid OMB control number. <b>PLEASE DO NOT RETURN YOUR FORM TO THE ABOVE ADDRESS.</b>					
<b>1. REPORT DATE (DD-MM-YYYY)</b> 15-06-2009		<b>2. REPORT TYPE</b> Final Report		<b>3. DATES COVERED (From – To)</b> 25 September 2006 - 28-Jan-10	
<b>4. TITLE AND SUBTITLE</b> Progressive failure analysis of advanced composites			<b>5a. CONTRACT NUMBER</b> FA8655-06-1-3072		
			<b>5b. GRANT NUMBER</b>		
			<b>5c. PROGRAM ELEMENT NUMBER</b>		
<b>6. AUTHOR(S)</b> Dr. Pedro MPRC Camanho			<b>5d. PROJECT NUMBER</b>		
			<b>5d. TASK NUMBER</b>		
			<b>5e. WORK UNIT NUMBER</b>		
<b>7. PERFORMING ORGANIZATION NAME(S) AND ADDRESS(ES)</b> University of Porto Dept. of Mechanical Engineering Porto 4200-465 Portugal				<b>8. PERFORMING ORGANIZATION REPORT NUMBER</b> N/A	
<b>9. SPONSORING/MONITORING AGENCY NAME(S) AND ADDRESS(ES)</b> EOARD Unit 4515 BOX 14 APO AE 09421				<b>10. SPONSOR/MONITOR'S ACRONYM(S)</b>	
				<b>11. SPONSOR/MONITOR'S REPORT NUMBER(S)</b> Grant 06-3072	
<b>12. DISTRIBUTION/AVAILABILITY STATEMENT</b> Approved for public release; distribution is unlimited.					
<b>13. SUPPLEMENTARY NOTES</b>					
<b>14. ABSTRACT</b> <p>This report results from a contract tasking University of Porto as follows: Structural failure of laminated composites is the result of the accumulation of several damage mechanisms such as matrix cracking, fiber fracture, fiber kinking, and delamination. The use of advanced physically-based computational models in the simulation of the mechanical response of laminated composites can reduce the number of experimental tests required to certify the composite structures used in aircraft. To develop robust analysis methods that can predict the strength and damage tolerance of advanced composite structures it is necessary to account for the onset and evolution of damage, and for the corresponding redistribution of internal loads.</p> <p>The objective of the project is to develop accurate, robust analytical and computational tools for calculating the strength and damage tolerance of advanced composite structures.</p> <p>The models to be developed are derived in the context of Continuum Damage Mechanics (CDM), which provides a rigorous framework to define the constitutive model and the corresponding computational implementation. The CDM models are implemented in a non-linear Finite Element code (ABAQUS) and must be able to predict the onset and type of damage, damage propagation, and structural collapse without requiring any intervention of the user during the analysis.</p>					
<b>15. SUBJECT TERMS</b> EOARD, damage models, Composites					
<b>16. SECURITY CLASSIFICATION OF:</b>			<b>17. LIMITATION OF ABSTRACT</b> UL	<b>18. NUMBER OF PAGES</b> 131	<b>19a. NAME OF RESPONSIBLE PERSON</b> WYNN SANDERS, Maj, USAF
<b>a. REPORT</b> UNCLAS	<b>b. ABSTRACT</b> UNCLAS	<b>c. THIS PAGE</b> UNCLAS			<b>19b. TELEPHONE NUMBER</b> <i>(Include area code)</i> +44 (0)1895 616 007



UMEC  
Composite Materials

**Project:** Progressive failure analysis of advanced composites

**Contract:** FA8655-06-1-3072

**Document Reference:** FR-FA8655-06-1-3072

**Date:** 25-07-2008

## Final Report

### Progressive failure analysis of advanced composites

Issue: draft

Date: 25-07-2008

#### Summary:

*This report presents the work performed during the first year of the project Progressive Failure Analysis of Advanced Composites. The computational models developed to predict first ply failure (UVARM), and damage onset and propagation (UMAT and VUMAT) are described. Several examples of application of the computational models in the simulation of the mechanical response of composite structures are presented, as well as the main publications that resulted from the project.*

Document prepared by: PP Camanho

#### Document distribution list

<b>Name</b>	<b>Company</b>	<b>Nº of copies</b>
Wynn S. Sanders	EOARD	1
Pedro Camanho	INEGI	1
Carlos Dávila	NASA – Langley Research Center	1
Joan Andreu Mayugo	University of Girona	1



# Contents

<b>1</b>	<b>Introduction</b>	<b>11</b>
<b>2</b>	<b>UVARM subroutine</b>	<b>13</b>
2.1	Overview . . . . .	13
2.2	In-situ strengths . . . . .	13
2.3	Failure criteria . . . . .	15
2.3.1	Transverse fracture . . . . .	15
2.3.2	Longitudinal failure . . . . .	17
2.4	Input into Abaqus standard . . . . .	17
2.5	Example . . . . .	19
<b>3</b>	<b>UMAT subroutine</b>	<b>23</b>
3.1	Overview . . . . .	23
3.2	Input into Abaqus standard . . . . .	24
3.2.1	Shell elements . . . . .	24
3.2.2	Continuum elements . . . . .	26
3.2.3	Effect of Element Size and Toughness on Degradation Rates .	28
3.2.4	Thermal stresses . . . . .	29
3.3	Example . . . . .	29
<b>4</b>	<b>VUMAT subroutine</b>	<b>35</b>
4.1	Overview . . . . .	35
4.2	Input into Abaqus explicit . . . . .	35
4.2.1	Shell elements . . . . .	35
4.2.2	Continuum elements . . . . .	37
4.3	Example . . . . .	40
<b>5</b>	<b>Conclusions</b>	<b>43</b>
	<b>Bibliography</b>	<b>44</b>





# List of Figures

2-1	In-situ effect in laminated composites (after Dvorak [7]). . . . .	14
2-2	Field variable 1 in a $0^\circ$ ply. . . . .	21
2-3	Field variable 3 in a $0^\circ$ ply. . . . .	21
3-1	Damage evolution in longitudinal tension. . . . .	25
3-2	Coarse mesh - elements with toughness increased. . . . .	32
3-3	Refined mesh - real material properties. . . . .	33
3-4	Onset of damage localization. . . . .	33
3-5	Predicted load-displacement relation. . . . .	34
4-1	Specimen and impactor. . . . .	40
4-2	Predicted delamination. . . . .	41
4-3	Predicted transverse matrix cracking in the laminate back-face. . . .	41
4-4	Predicted transverse matrix cracking in the contact region between the impactor and laminate. . . . .	42



# List of Tables

2.1	Parameters calculated by the subroutine. . . . .	17
2.2	Format required for the jobname.mt file. . . . .	18
2.3	Ply elastic properties for IM7-8552. . . . .	20
2.4	Ply strengths for IM7-8552. . . . .	20
2.5	Calculated in-situ strengths for IM7-8552 (MPa). . . . .	20
3.1	Material properties in the jobname.inp file. . . . .	24
3.2	State variables. . . . .	26
3.3	Material properties in the jobname.inp file. . . . .	27
3.4	Ply elastic properties for IM7-8552. . . . .	30
3.5	Ply strengths for IM7-8552. . . . .	30
3.6	Calculated in-situ strengths for IM7-8552 (MPa). . . . .	30
3.7	Fracture energies for transverse fracture for IM7-8552 (kJ/m <sup>2</sup> ). . . . .	30
3.8	Fracture energies for longitudinal fracture for IM7-8552 (kJ/m <sup>2</sup> ). . . . .	31
4.1	State variables. . . . .	37
4.2	State variables. . . . .	39

# LIST OF SYMBOLS

$E_i$	Young's modulus.
$G_{ij}$	Shear modulus.
$G_M, M = 1+, 1-, 2+, 2-, 6$	Fracture energies per unit area.
$G_{1+}^L$	Fracture energy per unit area for mode I crack propagation perpendicular to the fiber direction - linear softening.
$G_{1+}^E$	Fracture energy per unit area for mode I crack propagation perpendicular to the fiber direction - exponential softening.
$G_{2+}$	Mode I fracture energy per unit area for crack propagation along the fibre direction.
$G_6$	Mode II fracture energy per unit area for crack propagation along the fibre direction.
$G_{1-}$	Fracture energy per unit area for crack propagation perpendicular to the fiber direction (fiber kinking).
$g$	Toughness ratio.
$Y_T$	In-situ ply transverse tensile strength.
$Y_T^{\text{ud}}$	Ply transverse tensile strength measured in an unidirectional specimen.
$Y_C$	Ply transverse compressive strength.
$S_L$	In-situ ply shear strength.
$S_L^{\text{ud}}$	Ply shear strength measured in an unidirectional specimen.
$S_T$	Ply shear strength in the fracture plane.
$X_T$	Ply longitudinal tensile strength.
$X_{PO}$	Transition strength

$X_C$	Ply longitudinal compressive strength.
$\alpha_0$	Fracture angle.
$\alpha_{ii}$	Coefficients of thermal expansion.
$\beta_{ii}$	Coefficients of hygroscopic expansion.
$\beta$	Shear response factor.
$\eta^L$	Coefficient of longitudinal influence.
$\eta^T$	Coefficient of transverse influence.
$\eta^{\text{visc}}$	Viscosity parameter.
$\varepsilon_{ij}$	Strain tensor.
$\sigma_{ij}$	Stress tensor.
$\sigma_{ij}^{(m)}$	Stress tensor in the fiber misalignment frame.
$\nu_{ij}$	Poisson's ratios.
$\Delta M$	Variation in moisture content.
$\Delta T$	Temperature difference.

# ABBREVIATIONS

LaRC    Langley Research Center

CFRP    Carbon-fiber reinforced plastic.

# 1. INTRODUCTION

---

This report presents the formulation and computational implementation of the LaRC ply-based failure criteria for laminated composite materials, and the implementation of a continuum damage model that is able to predict the onset and propagation of ply failure mechanisms as well as the final failure load of composite structures.

The LaRC failure criteria is implemented by means of a **UVARM** ABAQUS® subroutine, whereas the continuum damage model is implemented in both a **UMAT** subroutine for implicit analysis and in a **VUMAT** subroutine for explicit analysis.

This report explains in detail the definition of the required material properties and initial conditions in the ABAQUS® input file. In addition, examples of application of the subroutines developed are presented at the end of each section of the report.

The papers that were published in the context of the project activities are presented in Annexes B and C.





## 2. UVARM SUBROUTINE

---

### 2.1 Overview

This section presents a reference manual for the use of an ABAQUS® user subroutine UVARM [1] with the implementation of the plane-stress LaRC failure criteria [2]-[5]. The basic equations of the LaRC failure criteria and the details of its implementation are presented. An example of the use of the subroutine in the simulation of an open-hole carbon-epoxy quasi-isotropic laminate loaded in tension is presented.

### 2.2 In-situ strengths

The in-situ effect, originally detected in Parvizi's tensile tests of cross-ply glass fiber reinforced plastics [6], is characterized by higher transverse tensile and shear strengths of a ply when it is constrained by plies with different fiber orientations in a laminate, compared with the strength of the same ply in an unidirectional laminate. The in-situ strength depends on the number of plies clustered together, and on the fiber orientation of the constraining plies. The model proposed for the calculation of the in-situ strengths uses the simplifying assumption that the fiber orientation of the constraining layers does not affect the value of the in-situ strength.

The in-situ effect is illustrated in Figure 2-1, where the relation between the in-situ transverse tensile strength experimentally measured and the total number of 90° plies clustered together (2n) is represented.

It is clear that accurate in-situ strengths are necessary for any stress-based failure criterion for matrix cracking in constrained plies. Therefore, the user should calculate the in-situ strengths that are required for the LaRC failure criteria [2]-[5]. The in-situ strengths are an input for the ABAQUS® UVARM subroutine.

The closed-form solutions to predict the in-situ strengths previously proposed can be used [2]. The tensile transverse in-situ strengths are given by [2]:

$$\text{For a thin embedded ply: } Y_T = \sqrt{\frac{8G_{2+}}{\pi t \Lambda_{22}^o}} \quad (2.1)$$

$$\text{For a thin outer ply: } Y_T = 1.79 \sqrt{\frac{G_{2+}}{\pi t \Lambda_{22}^o}} \quad (2.2)$$

$$\text{For a thick ply: } Y_T = 1.12 \sqrt{2} Y_T^{\text{UD}} \quad (2.3)$$

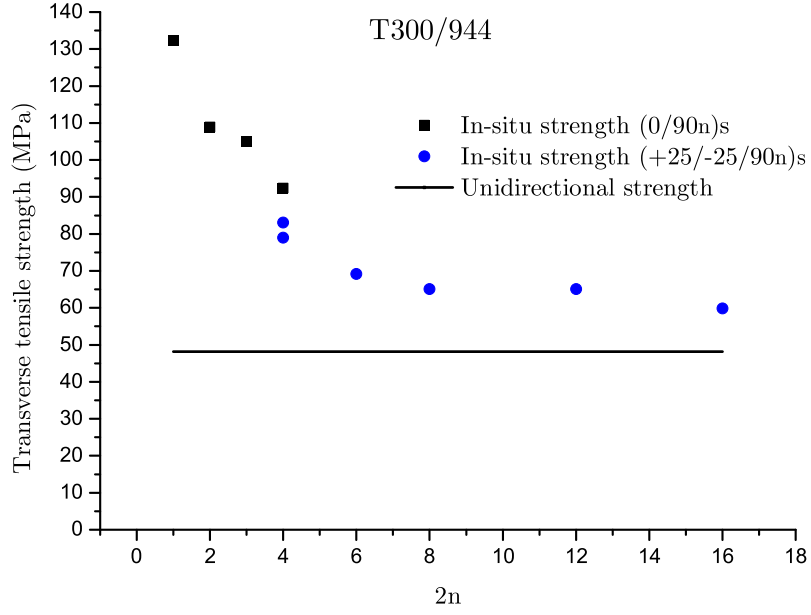


Figure 2-1 In-situ effect in laminated composites (after Dvorak [7]).

where  $Y_T^{UD}$  is the tensile transverse strength measured in an unidirectional test specimen,  $t$  is the ply thickness,  $G_{2+}$  is the mode I fracture toughness, and  $\Lambda_{22}^\circ$  is defined as:

$$\Lambda_{22}^\circ = 2 \left( \frac{1}{E_2} - \frac{\nu_{21}^2}{E_1} \right) \quad (2.4)$$

The in-situ shear strengths are obtained as [2]:

$$S_L = \sqrt{\frac{(1 + \beta \phi G_{12}^2)^{1/2} - 1}{3\beta G_{12}}} \quad (2.5)$$

where  $\beta$  is the shear response factor, and the parameter  $\phi$  is defined according to the configuration of the ply:

$$\begin{aligned} \text{For a thick ply:} \quad \phi &= \frac{12 (S_L^{UD})^2}{G_{12}} + 18\beta (S_L^{UD})^4 \\ \text{For a thin ply:} \quad \phi &= \frac{48G_6}{\pi t} \\ \text{For an outer ply:} \quad \phi &= \frac{24G_6}{\pi t} \end{aligned} \quad (2.6)$$

where  $S_L^{UD}$  is the shear strength measured in an unidirectional test specimen, and  $G_6$  is the mode II fracture toughness.

## 2.3 Failure criteria

### 2.3.1 Transverse fracture

#### Tension

The LaRC criterion to predict failure under transverse tension ( $\sigma_{22} \geq 0$ ) and in-plane shear is defined as:

$$\begin{aligned} (1-g) \frac{\sigma_{22}}{Y_T} + g \left( \frac{\sigma_{22}}{Y_T} \right)^2 + \left( \frac{\sigma_{12}}{S_L} \right)^2 - 1 &\leq 0 \\ (1-g) \frac{\sigma_{22}^{(m)}}{Y_T} + g \left( \frac{\sigma_{22}^{(m)}}{Y_T} \right)^2 + \left( \frac{\sigma_{12}^{(m)}}{S_L} \right)^2 - 1 &\leq 0, \\ \sigma_{11} < 0, |\sigma_{11}| < X_C/2 & \end{aligned} \quad (2.7)$$

where  $g = \frac{G_{2+}}{G_6}$ .

The stresses  $\sigma_{ij}^{(m)}$  are calculated in a frame aligned with the fiber direction according to the following expressions:

$$\begin{aligned} \sigma_{11}^{(m)} &= \sigma_{11} \cos^2 \varphi + \sigma_{22} \sin^2 \varphi + 2 |\sigma_{12}| \sin \varphi \cos \varphi \\ \sigma_{22}^{(m)} &= \sigma_{11} \sin^2 \varphi + \sigma_{22} \cos^2 \varphi - 2 |\sigma_{12}| \sin \varphi \cos \varphi \\ \sigma_{12}^{(m)} &= -\sigma_{11} \sin \varphi \cos \varphi + \sigma_{22} \sin \varphi \cos \varphi + \\ &\quad + |\sigma_{12}| (\cos^2 \varphi - \sin^2 \varphi) \end{aligned} \quad (2.8)$$

where the misalignment angle  $\varphi$  is defined as:

$$\varphi = \frac{|\sigma_{12}| + (G_{12} - X_C) \varphi^c}{G_{12} + \sigma_{11} - \sigma_{22}} \quad (2.9)$$

$$\varphi^c = \tan^{-1} \left[ \frac{1 - \sqrt{1 - 4\varpi \left( \frac{S_L}{X_C} \right)}}{2\varpi} \right] \quad (2.10)$$

with  $\varpi = \frac{S_L}{X_C} + \eta^L$ .

## Compression

The failure criteria used to predict fracture under transverse compression ( $\sigma_{22} < 0$ ) and in-plane shear is defined as:

$$\left(\frac{\tau_e^T}{S_T}\right)^2 + \left(\frac{\tau_e^L}{S_L}\right)^2 - 1 \leq 0, \sigma_{11} \geq -Y_C \quad (2.11)$$

$$\left(\frac{\tau_e^{(m)T}}{S_T}\right)^2 + \left(\frac{\tau_e^{(m)L}}{S_L}\right)^2 - 1 \leq 0, \sigma_{11} < -Y_C \quad (2.12)$$

The effective shear stresses in the fracture plane are defined as:

$$\tau_e^T = \langle |\tau^T| + \eta^T \sigma_n \cos \theta \rangle \quad (2.13)$$

$$\tau_e^L = \langle |\tau^L| + \eta^L \sigma_n \sin \theta \rangle \quad (2.14)$$

with  $\theta = \tan^{-1} \left( \frac{-|\sigma_{12}|}{\sigma_{22} \sin \alpha} \right)$ .  $\langle x \rangle$  is the McAuley operator defined as  $\langle x \rangle := \frac{1}{2} (x + |x|)$ . The components of the stress tensor on the fracture plane are given by:

$$\begin{cases} \sigma_n = \sigma_{22} \cos^2 \alpha \\ \tau^T = -\sigma_{22} \sin \alpha \cos \alpha \\ \tau^L = \sigma_{12} \cos \alpha \end{cases} \quad (2.15)$$

The terms  $\tau_e^{mT}$  and  $\tau_e^{mL}$  are calculated from equations (2.13)-(2.14) using the relevant components of the stress tensor established in a frame representing the fibre misalignment. The fracture plane is defined by the angle  $\alpha$ . The determination of  $\alpha$  is performed numerically maximizing equations (2.11) and (2.12).

The coefficients of transverse and longitudinal influence,  $\eta^T$  and  $\eta^L$  respectively, can be obtained as:

$$\eta^T = \frac{-1}{\tan 2\alpha_0} \quad (2.16)$$

$$\eta^L = -\frac{S_L \cos 2\alpha_0}{Y_C \cos^2 \alpha_0} \quad (2.17)$$

where  $\alpha_0$  is the fracture angle under pure transverse compression ( $\alpha_0 \approx 53^\circ$ ).

In the absence of test data the transverse shear strength can be estimated as:

$$S_T = Y_C \cos \alpha_0 \left( \sin \alpha_0 + \frac{\cos \alpha_0}{\tan 2\alpha_0} \right) \quad (2.18)$$

### 2.3.2 Longitudinal failure

#### Tension

The failure criterion used to predict fiber fracture under longitudinal tension ( $\sigma_{11} \geq 0$ ) is defined as:

$$\frac{\sigma_{11}}{X_T} - 1 \leq 0 \quad (2.19)$$

#### Compression

The failure criterion used to predict fiber fracture under longitudinal compression ( $\sigma_{11} < 0$ ) and in-plane shear (fiber kinking) is given as:

$$\begin{aligned} \left\langle \frac{|\sigma_{12}^{(m)}| + \eta^L \sigma_{22}^{(m)}}{S_L} \right\rangle - 1 &\leq 0, \quad \sigma_{22}^{(m)} < 0 \\ (1 - g) \frac{\sigma_{22}^{(m)}}{Y_T} + g \left( \frac{\sigma_{22}^{(m)}}{Y_T} \right)^2 + \left( \frac{\sigma_{12}^{(m)}}{S_L} \right)^2 - 1 &\leq 0, \\ \sigma_{22}^{(m)} \geq 0, |\sigma_{11}| &\geq X_C/2 \end{aligned} \quad (2.20)$$

Based on the equations outlined above, the subroutine calculates the following parameters that can be used for post-processing:

Table 2.1 Parameters calculated by the subroutine.

UARM(1)	Failure index for transverse tensile failure
UARM(2)	Failure index for transverse compressive failure
UARM(3)	Failure index for longitudinal tensile failure
UARM(4)	Failure index for longitudinal compressive failure

## 2.4 Input into Abaqus standard

The user must create a file with the name `jobname.mt` where the material properties are defined. The file must have the same name as the `.inp` file that defines the model. The file `jobname.mt` must be placed in the same directory where the ABAQUS® input file is located.

The format of the file `jobname.mt` is the shown in Table 3.1.

The symbol `**` means that the corresponding lines can be used to write comments. The name of the material (line 4) must be the same as the one given in the ABAQUS®

Table 2.2 Format required for the jobname.mt file.

Line				Column				
	1	2	3	4	5	6	7	8
1	**							
2	3							
3	**							
4	MATERIAL							
5	**							
6	$E_1$	$E_2$	$E_3$	$v_{21}$	$v_{31}$	$v_{32}$		
7	**							
8	$G_{12}$	$G_{23}$	$G_{31}$	$X_T$	$X_C$	$Y_T$	$Y_C$	$S_L^{\text{ud}}$
9	**							
10	$\alpha_0$	$\beta$	$g$	$S_L$				

jobname.inp file and must be written in CAPITALS. Lines 3 to 10 can be repeated for the definition of other materials. The following is an example of a file with the definition of three materials.

```

** LaRC03 failure criteria: use 3 for LaRC03 and 4 for LaRC04
3
** MAT. #1: IM7-8552-thin: thin embedded ply
IM7-8552-THIN
** E1      , E2      , E3      , nu21 , nu31 , nu32
171420., 9080., 9080., 0.017, 0.017, 0.4
** G12     , G23     , G31     , XT      , XC      , YT      , YC      , SL
5290., 3242.9, 5290., 2323.5, 1200.1, 160.2, 199.8, 92.3
** alphao, beta, g      , SL_IS
53.      , 0.      , 0.5, 130.2
** MAT. #2: IM7-8552-thin: thin outer ply
IM7-8552-THIN-OUTER
** E1      , E2      , E3      , nu21 , nu31 , nu32
171420., 9080., 9080., 0.017, 0.017, 0.4
** G12     , G23     , G31     , XT      , XC      , YT      , YC      , SL
5290., 3242.9, 5290., 2323.5, 1200.1, 101.4, 199.8, 92.3
** alphao, beta, g      , SL_IS
53.      , 0.      , 0.5, 107.
** MAT. #3: IM7-8552-thin-2t: embedded ply with t=2*ply thickness
IM7-8552-THIN-2T
** E1      , E2      , E3      , nu21 , nu31 , nu32
171420., 9080., 9080., 0.017, 0.017, 0.4
** G12     , G23     , G31     , XT      , XC      , YT      , YC      , SL
5290., 3242.9, 5290., 2323.5, 1200.1, 113.3, 199.8, 92.3
** alphao, beta, g      , SL_IS
53.      , 0.      , 0.5, 106.9

```

The user must define consistent material properties in the `jobname.inp` file, and define four user output variables following the example shown below:

```

*MATERIAL, NAME=IM7-8552-thin-outer
*ELASTIC, TYPE=LAMINA
171420., 9080., 0.32, 5290., 5290., 3242.9
*USER OUTPUT VARIABLES
4,

```

## 2.5 Example

An ABAQUS® model with an example of the use of the UVARM subroutine in the prediction of first ply failure of a quasi-isotropic Hexcel IM7-8552 [90/0/ ± 45]<sub>3s</sub> CFRP laminate with a central hole and loaded in tension can be downloaded from the following URL:

```

www.fe.up.pt/~pcamanho/oht3_03.inp
www.fe.up.pt/~pcamanho/model_oht3.inp
www.fe.up.pt/~pcamanho/oht3_03.mt

```



The model uses ABAQUS® S4 shell elements. The specimen is 3mm thick, 150mm long, 36mm wide and has a central hole with a diameter of 6mm.

The material properties used are shown in Tables 3.4-3.6.

Table 2.3 Ply elastic properties for IM7-8552.

Property	Value
$E_1$ (GPa)	171.42
$E_2$ (GPa)	9.08
$G_{12}$ (GPa)	5.29
$\nu_{12}$	0.32

Table 2.4 Ply strengths for IM7-8552.

Property	Value (MPa)
$X_T$	2326.2
$X_C$	1200.1
$Y_T^{\text{ud}}$	62.3
$Y_C$	199.8
$S_L^{\text{ud}}$	92.3

Table 2.5 Calculated in-situ strengths for IM7-8552 (MPa).

Ply configuration	$Y_T$	$S_L$
Thin embedded ply	160.2	130.2
Thin outer ply	101.4	107.0

Figures 2-2 and 2-3 show respectively the field variables **UARM(1)** and **UARM(3)** of the  $0^\circ$  ply for an applied end displacement of 0.5mm.

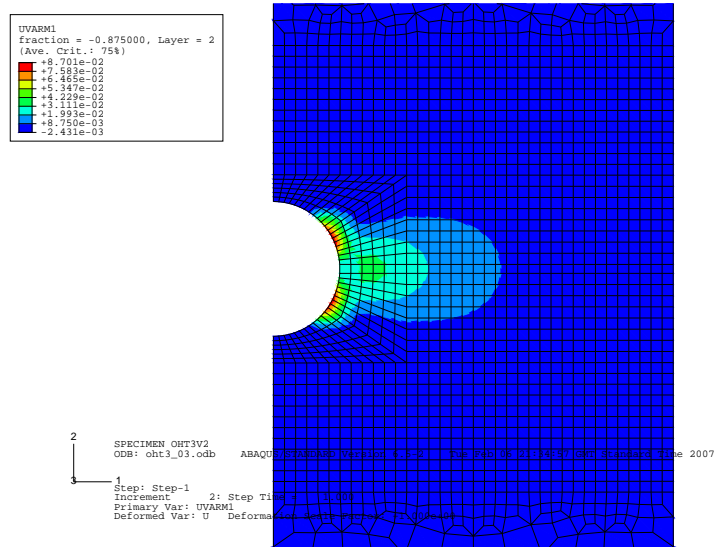


Figure 2-2 Field variable 1 in a 0° ply.

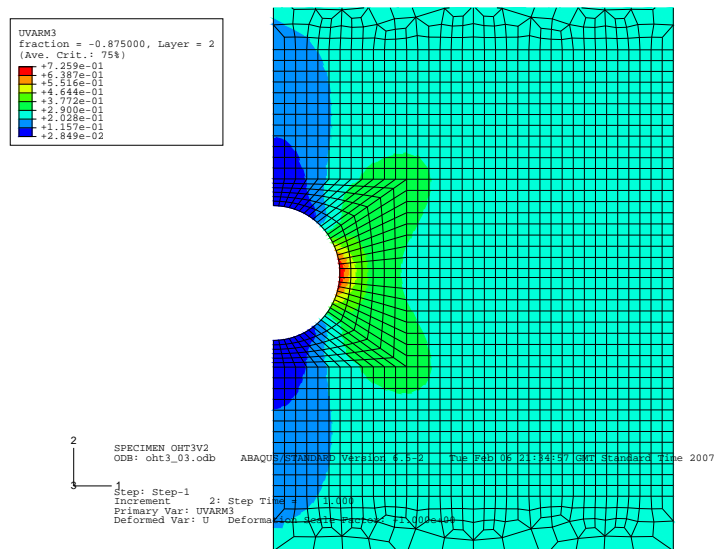


Figure 2-3 Field variable 3 in a 0° ply.



## 3. UMAT SUBROUTINE

---

### 3.1 Overview

The second part of this report is a reference manual for the use of an ABAQUS® user subroutine **UMAT** [1] with the implementation of a continuum damage model for laminated composites.

The plane-stress continuum damage model implemented in ABAQUS® is described in detail in references [8]-[11]. The continuum damage model is defined in the framework of the thermodynamics of irreversible processes. Generally speaking, the formulation of the continuum damage models starts by the definition of a potential (for example, the complementary free energy per unit volume) as a function of the damage variables. The potential is the basis for establishing the relation between the stress and the strain tensors. For the complete definition of the constitutive models it is also necessary to define the damage activation functions, i.e. the conditions that lead to the onset of inelastic response, and the damage evolution functions.

The present continuum damage for ABAQUS® predicts the onset and accumulation of intralaminar damage mechanisms (matrix cracking and fiber fracture) in laminated composites as well as final structural collapse by the propagation of a macro-crack. The macro-crack is represented by a line of localized shell or continuum elements, i.e., elements where the constitutive tangent tensor is not positive definite.

This report presents the basic equations required for the definition of the material properties and it explains how to define the model in ABAQUS® standard. An example of the simulation of fracture of an open-hole carbon-epoxy quasi-isotropic laminate loaded in tension is also described.

The full details of the development and validation of the model are presented in the papers shown in Appendix B and Appendix C:

- P.P. Camanho, P. Maimí, C.G. Dávila, *Prediction of size effects in notched laminates using continuum damage mechanics*, **Composites Science and Technology**, 67, 2715-2727, 2007. This paper describes the application of the model in the prediction of size effects in notched composites using shell elements.
- H. Koerber, P.P. Camanho, *Simulation of progressive damage in bolted composite joints*, **Proceedings of the 13th European Conference on Composite Materials (ECCM-13)**, Stockholm, Sweden, 2008. This paper presents the application of the model in the prediction of the mechanical response of CFRP bolted joints using solid elements. In addition, the paper compares the model proposed here with the ABAQUS® built-in damage model [1].

## 3.2 Input into Abaqus standard

### 3.2.1 Shell elements

#### Material properties

The material properties must be defined by the user in the `jobname.inp` file according to the following example.

```

**
** MATERIAL #1: thin embedded ply
**
** E1, E2, G12, v12, alpha1,alpha2, XT, XP0
** XC, YT, YC, ALPHA0, SL , SLud , GIC_F1, GIC_FE
** GIC_M, GIIC_M, GIC_FC, GIIC_M-, beta1, beta2 , DM, Eta_viscous
**
*MATERIAL,NAME=IM7-8552-thin
*USER MATERIAL, CONSTANTS=24, UNSYMM
**
171420., 9080. , 5290., 0.32 , -5.5E-6, 25.8E-6, 2323.5, 232.3,
1200.1, 160.2 , 199.8 , 0.925, 130.2, 92.3, 31.5, 50.0,
0.2774, 0.7879, 106.3 , 1.3092, 0.000, 0.005, 0.0, 0.000
**
*DENSITY
1590E-6
**
*DEPVAR
15

```

The material properties defined after the `*USER MATERIAL` command are shown in Table 3.1.

Table 3.1 Material properties in the `jobname.inp` file.

Line				Column				
	1	2	3	4	5	6	7	8
1	$E_1$	$E_2$	$G_{12}$	$v_{12}$	$\alpha_{11}$	$\alpha_{22}$	$X_T$	$X_{PO}$
2	$X_C$	$Y_T$	$Y_C$	$\alpha_0$	$S_L$	$S_L^{\text{ud}}$	$G_{1+}^L$	$G_{1+}^E$
3	$G_{2+}$	$G_6$	$G_{1-}$	$G_{2-}$	$\beta_{11}$	$\beta_{22}$	$\Delta M$	$\eta^{\text{visc}}$

Most of the properties required are standard ply properties. However, non-standard material properties are also required.  $X_{PO}$  is the transition strength used for the definition of the damage evolution law for longitudinal tensile failure.  $G_{1+}^L$  and  $G_{1+}^E$  are respectively the fracture energies per unit area related with the linear and exponential softening laws shown on Figure 3-1.

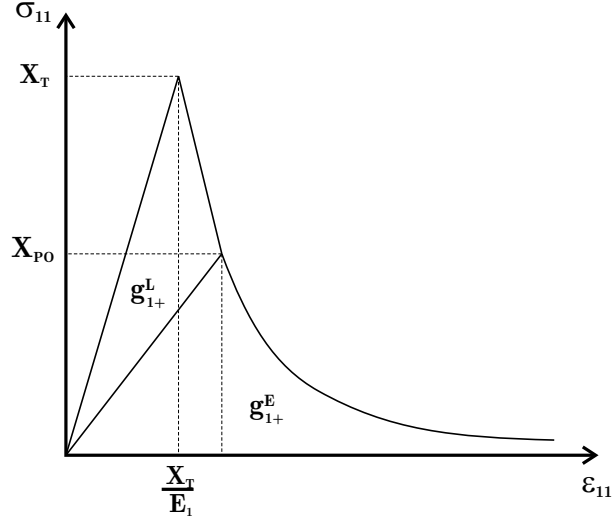


Figure 3-1 Damage evolution in longitudinal tension.

The parameter  $\alpha_0$  is the fracture angle of a ply under pure transverse compression. For graphite/epoxy and glass/epoxy materials the fracture angle  $\alpha_0$  is typically equal to  $53^\circ$ .  $\eta^{\text{visc}}$  is the parameter used in the viscous regularization procedure used to mitigate convergence difficulties.

### Initial conditions

The model requires the definition of the initial values of the state variables. Therefore, the `jobname.inp` file must include the following command:

```
**
** Initialization of the state variables:
**
** ELSET, rfT, rmT, rfC, rmC , AfC, AmT, AmC, d1, d2, d6,
** dr/dr, gf, gm, FlfX, ALEA
**
*INITIAL CONDITIONS, TYPE=SOLUTION
  OUT_PLT, 1.0, 1.0, 1.0, 1.0, -1.0, -1.0, -1.0,
  0.0, 0.0, 0.0, 0.0, 0.0, 0.0, 0.0, 1.0
```

where `OUT_PLT` represents the group of all elements whose constitutive model is defined by the `UMAT` subroutine. The state variables are shown in Table 3.2.

Table 3.2 State variables.

STATEV(1)	$r_{1+}$	Damage threshold function
STATEV(2)	$r_{2+}$	Damage threshold function
STATEV(3)	$r_{1-}$	Damage threshold function
STATEV(4)	$r_{2-}$	Damage threshold function
STATEV(5)	$A_{1-}$	Adjustment constant
STATEV(6)	$A_{2+}$	Adjustment constant
STATEV(7)	$A_{2-}$	Adjustment constant
STATEV(8)	$d_1$	Damage variable
STATEV(9)	$d_2$	Damage variable
STATEV(10)	$d_6$	Damage variable
STATEV(11)	$\partial r_{1+}^{t+1} / \partial r_{1+}^t$	Derivative required for the viscous regularization
STATEV(12)	$g_1$	Energy dissipated
STATEV(13)	$g_2 + g_6$	Energy dissipated
STATEV(14)	$\phi_{1\pm}^{t-1}$	Damage activation functions
STATEV(15)	Ran	Definition of random properties

The state variables STATEV(1) to STATEV(14) are defined in detail in references [8]-[11]. STATEV(15) should be equal to one if a random field of material properties is not required. Setting STATEV(15)=0 creates a random field for the ply longitudinal strengths. All the variables can be post-processed using ABAQUS® viewer:

```
*ELEMENT OUTPUT, ELSET=DAMAGE_ELEMS
1, 2, 3, 4
SDV
```

### 3.2.2 Continuum elements

#### Material properties

The material properties must be defined by the user in the `jobname.inp` file according to the following example.

```

** MATERIAL #1: thin embedded ply
**
** E1    , E2    , G12    , v12    , alpha1, alpha2, XT    , XP0,
** XC    , YT    , YC    , ALPHA0 , SL    , SLud  , GIC_F1, GIC_FE
** GIC_M, GIIC_M, GIC_FC, GIIC_M-, beta1 , beta2 , DM    , Eta_viscous
** v23   , thickness
**
**MATERIAL,NAME=IM7-8552-thin
**USER MATERIAL, CONSTANTS=26, UNSYMM
**
171420., 9080. , 5290., 0.32 , -5.5E-6, 25.8E-6, 2323.5, 232.3,
1200.1, 160.2 , 199.8 , 0.925, 130.2, 92.3, 31.5, 50.0,
0.2774, 0.7879, 106.3 , 1.3092, 0.000, 0.005, 0.0, 0.000,
0.52 , 0.125
**
*DENSITY
1590E-6
**
*DEPVAR
15

```

The material properties defined after the \*USER MATERIAL command are shown in Table 3.3.

Table 3.3 Material properties in the jobname.inp file.

Line				Column				
	1	2	3	4	5	6	7	8
1	$E_1$	$E_2$	$G_{12}$	$v_{12}$	$\alpha_{11}$	$\alpha_{22}$	$X_T$	$X_{PO}$
2	$X_C$	$Y_T$	$Y_C$	$\alpha_0$	$S_L$	$S_L^{\text{ud}}$	$G_{1+}^L$	$G_{1+}^E$
3	$G_{2+}$	$G_6$	$G_{1-}$	$G_{2-}$	$\beta_{11}$	$\beta_{22}$	$\Delta M$	$\eta^{\text{visc}}$
$v_{23}$	$t$							

The parameter  $t$  is the ply thickness.

### Initial conditions

The model requires the definition of the initial values of the state variables. Therefore, the jobname.inp file must include the following command:

```

**
** Initialization of the state variables:
**
** ELSET, rfT, rmT, rfC, rmC , AfC, AmT, AmC, d1, d2, d6,
** dr/dr, gf, gm, FlfX, ALEA
**

```



```
*INITIAL CONDITIONS, TYPE=SOLUTION
OUT_PLT, 1.0, 1.0, 1.0, 1.0, -1.0, -1.0, -1.0,
0.0, 0.0, 0.0, 0.0, 0.0, 0.0, 0.0, 1.0
```

The state variables are shown in Table 3.2.

### 3.2.3 Effect of Element Size and Toughness on Degradation Rates

To predict damage propagation, it is necessary to establish rates of material degradation that are energetically consistent. The present damage model relies on damage evolution laws that take into account the toughness of the material in each damage mode as well as the volume of material represented by each element integration point in the model [8]-[11]. However, correct degradation rates can only be achieved when the finite element mesh is sufficiently refined.

When an element is too large for a given material, it is not possible to achieve the proper degradation without a snap-back of the constitutive model [8]-[11]. Under these circumstances, the model is designed to reduce the material strengths as necessary to achieve the correct energy release rates. This approach allows the use of coarser meshes for damage propagation. However, the mesh in the regions of damage initiation should be sufficiently refined. In addition, care should be applied to ensure that the strengths of elements in coarse regions away from the damage areas are not reduced so much as to cause unrealistic failures. References [8]-[11] provide techniques to estimate the maximum size of elements in the regions of damage initiation: the maximum size for the finite element for each damage law  $M$  is:

$$l^* \leq \frac{2E_M G_M}{X_M^2}, M = 1\pm, 2\pm, 6 \quad (3.1)$$

where  $E_M$ ,  $G_M$  and  $X_M$  are the Young modulus, fracture energies and strengths, respectively.  $l^*$  is the characteristic size of the finite element (ABAQUS® CELENT parameter).

When the strength of an element is reduced the subroutine writes a warning message to the `modelname.dat` file according to the following format:

```
STRENGTH REDUCTION    YT = 101.229471616873    N. ELEMENT = 203
```

where YT is the adjusted value of the transverse tensile strength.

In addition, the coarse elements whose longitudinal tensile strength and transverse tensile and compressive strengths were reduced can be visualized using ABAQUS® viewer. The elements whose longitudinal compressive strength ( $X_C$ ) was reduced have the state variable STATEV(5) equal to 100. The elements whose transverse tensile and compressive strengths,  $Y_T$  and  $Y_C$  respectively, were reduced have the state variable STATEV(6) ( $Y_T$ ) and STATEV(7) ( $Y_C$ ) equal to 100.

### 3.2.4 Thermal stresses

The constitutive model calculates the residual thermal stresses that result from the different coefficients of thermal expansion in the longitudinal and transverse directions. To enable the calculation of the thermal stresses, the user should define in the `jobname.inp` file the amplitude of the thermal step as follows:

```
*AMPLITUDE, NAME=AMPL, DEFINITION=TABULAR
0.,0.,1.,1.
```

The residual thermal stresses should be calculated in the initial step, as shown in the following example:

```
**
** Step 1: thermal step
**
*STEP, INC=10000, UNSYMM=YES
*STATIC
0.5, 1., 1D-7, 1.
*TEMPERATURE, AMPLITUDE=AMPL
GLOBAL, -155.
```

where `GLOBAL` represent the group of nodes that belong to the elements whose constitutive model is defined by the UMAT subroutine, and -155 is the difference between the working and reference temperatures.

The following (mechanical) steps must include the following command:

```
*TEMPERATURE
GLOBAL, -155.
```

## 3.3 Example

An ABAQUS® model with an example of the use of the UMAT subroutine in the strength prediction of a quasi-isotropic Hexcel IM7-8552  $[90/0/\pm 45]_{3s}$  CFRP laminate with a central hole and loaded in tension can be downloaded from the following URL:

```
www.fe.up.pt/~pcamanho/oht3v2.inp
www.fe.up.pt/~pcamanho/model_open_hole_3_dy.inp
www.fe.up.pt/~pcamanho/IM7-8552.inp
```

The model is composed of ABAQUS® S4 shell elements and it represents a specimen that is 3mm thick, 150mm long, 36mm wide having a central hole with a diameter of 6mm. The difference between the working and stress-free temperatures used to

calculate the residual thermal stresses is  $-155^{\circ}\text{C}$ . An implicit dynamic analysis was performed considering a loading rate of 2mm/min. The use of an implicit dynamic finite element model enables the prediction of the load drop that occurs when the specimens fail catastrophically. An implicit static analysis normally fails to converge at the maximum load.

The material properties used are shown in Tables 3.4-3.6.

Table 3.4 Ply elastic properties for IM7-8552.

Property	Value
$E_1$ (GPa)	171.42
$E_2$ (GPa)	9.08
$G_{12}$ (GPa)	5.29
$\nu_{12}$	0.32

Table 3.5 Ply strengths for IM7-8552.

Property	Value (MPa)
$X_T$	2326.2
$X_C$	1200.1
$Y_T^{\text{ud}}$	62.3
$Y_C$	199.8
$S_L^{\text{ud}}$	92.3

Table 3.6 Calculated in-situ strengths for IM7-8552 (MPa).

Ply configuration	$Y_T$	$S_L$
Thin embedded ply	160.2	130.2
Thin outer ply	101.4	107.0

Table 3.7 Fracture energies for transverse fracture for IM7-8552 ( $\text{kJ/m}^2$ ).

Property	Value
$G_{2+}$	0.2774
$G_6$	0.7879

The fracture energy  $G_{2-}$  is calculated as  $G_{2-} = G_6 / \cos \alpha_0$  with  $\alpha_0 = 53^{\circ}$ .

As explained in section 3.2.3, the UMAT subroutine verifies the size of the elements in the beginning of the analysis: if the size of one element is large enough to cause a snap-back of the constitutive model, the strength of that element is reduced. Therefore, the mesh should be refined in the locations where damage initiation is likely to take place. It should be noted that a strength reduction may cause difficulties in

Table 3.8 Fracture energies for longitudinal fracture for IM7-8552 (kJ/m<sup>2</sup>).

Property	Value
G <sub>1+</sub>	81.5
G <sub>1-</sub>	106.3

coarse regions of the model away from the damage zones where the strength could be reduced enough to cause premature damage.

To overcome this difficulty, it is suggested to assign different material properties to the coarse elements located in regions where no damage takes place. The strategy proposed consists in increasing the fracture toughness of these elements to avoid the strength reduction. For example:

```

****
**** MATERIAL #4: linear elastic material
****
** E1, E2, G12, v12, alpha1, alpha2, XT , XP0,
** XC, YT, YC, ALPHA0 , SL, SLud , GIC_F1, GIC_FE
** GIC_M, GIIC_M, GIC_FC, GIIC_M-, beta1 , beta2 , DM , Eta_viscous
**
*MATERIAL,NAME=LE
*USER MATERIAL, CONSTANTS=24, UNSYMM
  171420., 9080. , 5290., 0.32 , -5.5E-6, 25.8E-6, 2323.5, 232.3,
  1200.1, 113.3 , 199.8 , 0.925, 106.9, 92.3 , 31.5e5, 50.0e5,
  0.2774e5, 0.7879e5, 106.3e5 , 1.3092e5, 0.000, 0.005, 0.0, 0.000
**
*DENSITY
  1590E-6
**
*DEPVAR
  15

```

Figure 3-2 highlights in red the region modeled with coarse elements with increased toughness, which implies a linear-elastic response for these elements. Figure 3-3 shows the region modeled with the actual material properties.

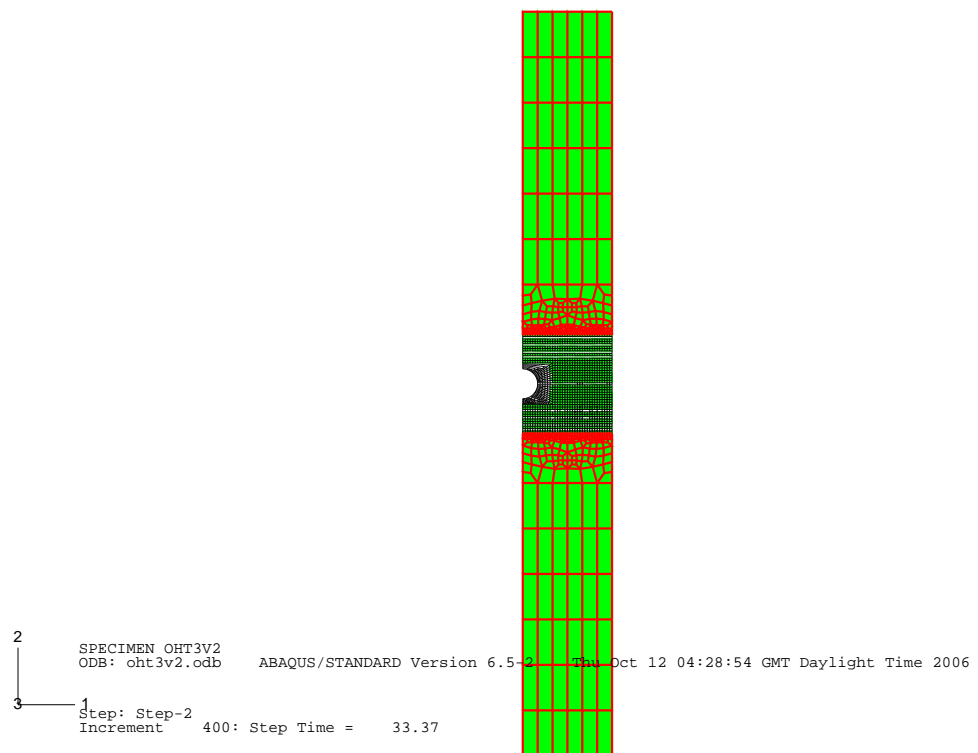


Figure 3-2 Coarse mesh - elements with toughness increased.

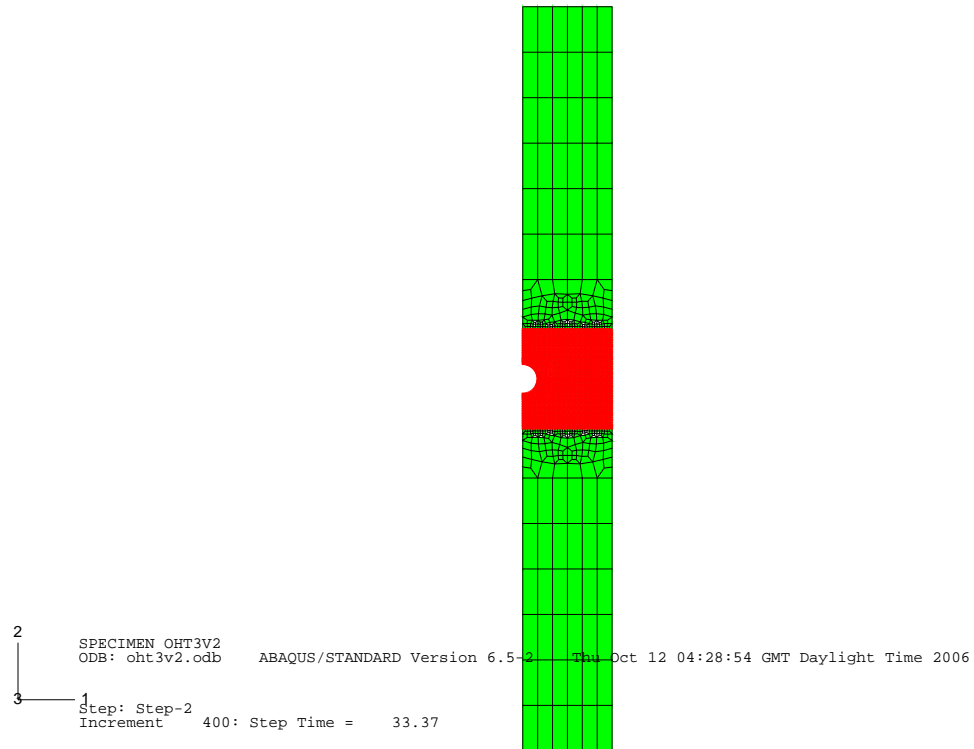


Figure 3-3 Refined mesh - real material properties.

The damage variable  $d_6$  in the  $0^\circ$  ply at the onset of damage localization is shown in Figure 3-4.

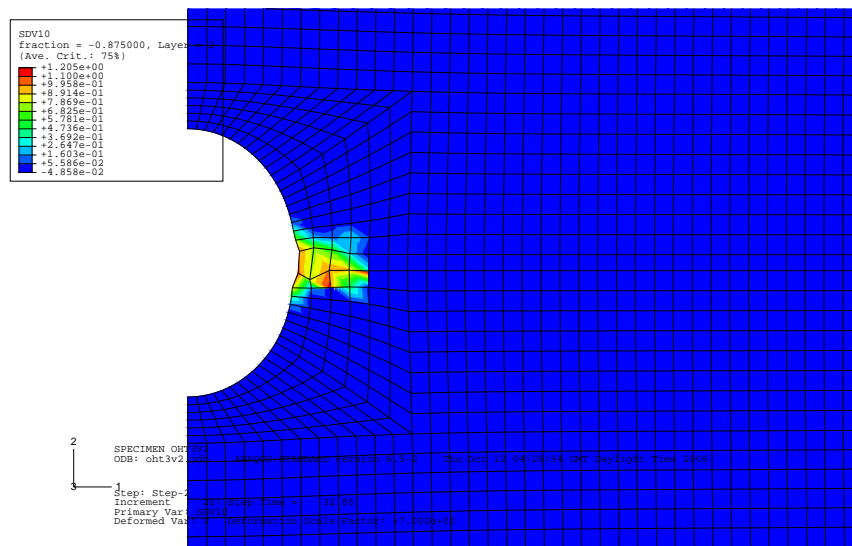


Figure 3-4 Onset of damage localization.

The predicted load-displacement relation is shown in Figure 3-5, where it can be observed that an implicit dynamic analysis predicts the load drop that occurs when the specimen fails catastrophically.

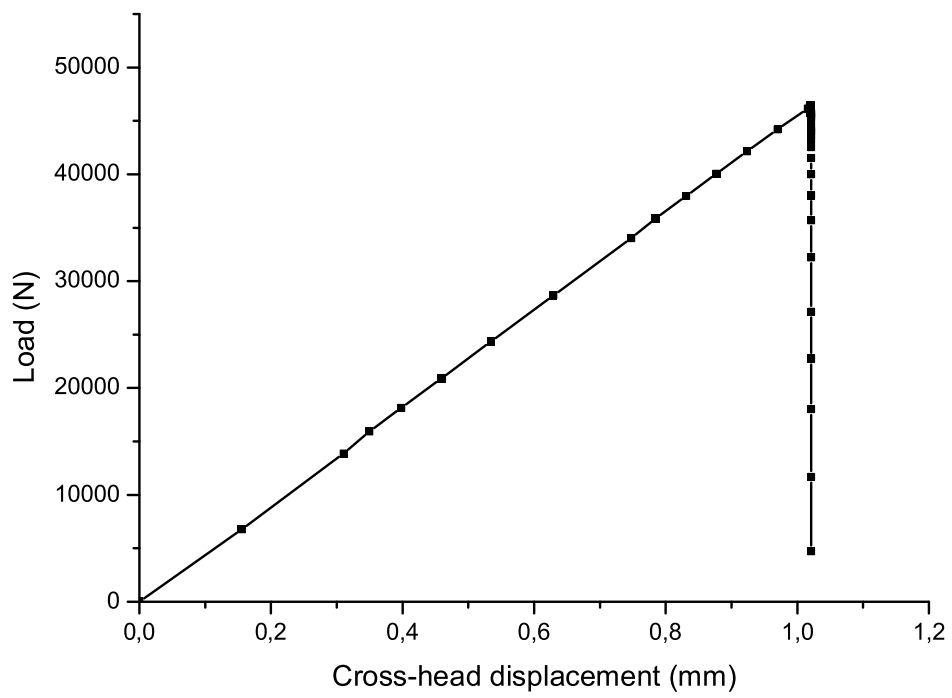


Figure 3-5 Predicted load-displacement relation.

## 4. VUMAT SUBROUTINE

---

### 4.1 Overview

The third part of this report is a reference manual for the use of an ABAQUS® user subroutine **VUMAT** [1] with the implementation of the continuum damage model for laminated composites described in section 3 and in the Appendix B. There are several relevant loading scenarios for which an explicit finite element code is more appropriate. For example, in dynamically loaded composite structures or in problems with multiple contact surfaces. In addition, explicit formulations can provide solutions for problems that suffer from severe convergence difficulties when implicit finite element codes are used.

Following the strategy used in the development of the **UMAT** subroutine, the code described in this section is able to simulate the mechanical response of composite structures using both shell and continuum elements.

This section includes an example of the simulation of a low-velocity impact in a composite laminate, using the **VUMAT** subroutine developed in this project, an additional **VUMAT** subroutine that simulates delamination onset and propagation (the development of this second **VUMAT** subroutine was planned for the second year of this project).

### 4.2 Input into Abaqus explicit

#### 4.2.1 Shell elements

##### Material properties

The material properties must be defined by the user in the `jobname.inp` file according to the following example.

```
**
** USER PLY MATERIAL
**
** E1      , E2      , G12      , v12      , alpha1, alpha2, XT      , XP0,
** XC      , YT      , YC      , ALPHA0 , SL      , SLud   , GIC_F1, GIC_FE
** GIC_M,  GIIC_M, GIC_FC, GIIC_M-, beta1 , beta2 , DM      , Eta_viscous
**
**MATERIAL,NAME=IM7-8552-Damage
```



```

*USER MATERIAL, CONSTANTS=25
  171420., 9080., 5290., 0.32 , -5.5E-6, 25.8E-6, 2323.5, 232.3,
    1200.1, 132.7, 199.8, 0.925,   117.1,    92.3,    81.5,   10.0,
      1.0,    2.0, 106.3,   1.31,    0.000,    0.005,    0.0,    0.0,
*Density
  1.59e-9
*DEPVAR,DELETE=17
  17
  1, rfT, "Fiber tension internal variable"
  2, rmT, "Matrix tension internal variable"
  3, rfC, "Fiber compr internal variable"
  4, rmC, "Matrix compr internal variable"
  5, AfC, "Fiber tension adjustment parameter"
  6, AmT, "Matrix tension adjustment parameter"
  7, AmC, "Matrix compr adjustment parameter"
  8, d1, "Damage variable, direction 11"
  9, d2, "Damage variable, direction 22"
 10, d6, "Damage variable, direction 12"
 11, gf, "Fiber dissipated energy"
 12, gm, "Matrix dissipated energy"
 13, E11, "Direct strain, direction 11"
 14, E22, "Direct strain, direction 22"
 15, E33, "Direct strain, direction 33"
 16, E12, "Shear strain, direction 12"
 17, STATUS, "Status of the element"

```

The **STATUS** variable defines the status of an element: if **STATUS=1** the element is active, and if **STATUS=0** the element has been deleted. The criterion implemented to delete an element from the mesh is based on the value of the damage variable associated with failure mechanisms in the longitudinal direction: if  $d_1 \geq 0.999$  the element is deleted from the mesh. This procedure prevents the severe reduction on the stable time increment that results from highly distorted, damaged, finite elements.

The material properties defined after the **\*USER MATERIAL** command are shown in Table 3.1.

### Initial conditions

The model requires the definition of the initial values of the state variables. Therefore, the **jobname.inp** file must include the following command:

```

** shell elements
** ELSET, rfT, rmT, rfC, rmC, AfC, AmT, AmC,
** d1, d2, d6, gf, gm, e11, e22, e33,
** e12, STATUS
**
*Initial Conditions, Type=Solution
<elset>, 1.0, 1.0, 1.0, 1.0, -1.0, -1.0, -1.0,
0.0, 0.0, 0.0, 0.0, 0.0, 0.0, 0.0, 0.0,
0.0, 1.0

```

where <elset> represents the group of all elements whose constitutive model is defined by the VUMAT subroutine.

The state variables used are shown in Table 4.1.

Table 4.1 State variables.

STATEV(1)	$r_{1+}$	Damage threshold function
STATEV(2)	$r_{2+}$	Damage threshold function
STATEV(3)	$r_{1-}$	Damage threshold function
STATEV(4)	$r_{2-}$	Damage threshold function
STATEV(5)	$A_{1-}$	Adjustment constant
STATEV(6)	$A_{2+}$	Adjustment constant
STATEV(7)	$A_{2-}$	Adjustment constant
STATEV(8)	$d_1$	Damage variable
STATEV(9)	$d_2$	Damage variable
STATEV(10)	$d_6$	Damage variable
STATEV(11)	$g_1$	Energy dissipated
STATEV(12)	$g_2 + g_6$	Energy dissipated
STATEV(13)	$\varepsilon_{11}$	11-component of the strain tensor
STATEV(14)	$\varepsilon_{22}$	22-component of the strain tensor
STATEV(15)	$\varepsilon_{33}$	33-component of the strain tensor
STATEV(16)	$\varepsilon_{12}$	12-component of the strain tensor
STATEV(17)	STATUS	Status of the element

#### 4.2.2 Continuum elements

##### Material properties

The material properties must be defined by the user in the `jobname.inp` file according to the following example.

```

** MATERIAL #1: thin embedded ply
**
** E1      , E2      , G12      , v12      , alpha1, alpha2, XT      , XP0,
** XC      , YT      , YC      , ALPHA0 , SL      , SLud   , GIC_F1, GIC_FE
** GIC_M,  GIIC_M, GIC_FC, GIIC_M-, beta1 , beta2 , DM      , Eta_viscous
** v23     , thickness
**
*MATERIAL,NAME=IM7-8552-thin
*USER MATERIAL, CONSTANTS=26, UNSYMM
**
171420., 9080. , 5290., 0.32 , -5.5E-6, 25.8E-6, 2323.5, 232.3,
1200.1, 160.2 , 199.8 , 0.925, 130.2, 92.3, 31.5, 50.0,
0.2774, 0.7879, 106.3 , 1.3092, 0.000, 0.005, 0.0, 0.000,
0.52 , 0.125
**
*DENSITY
1590E-6
**
*DEPVAR,DELETE=20
20
1, rfT, "Fiber tension internal variable"
2, rmT, "Matrix tension internal variable"
3, rfC, "Fiber compr internal variable"
4, rmC, "Matrix compr internal variable"
5, AfC, "Fiber tension adjustment parameter"
6, AmT, "Matrix tension adjustment parameter"
7, AmC, "Matrix compr adjustment parameter"
8, d1, "Damage variable, direction 11"
9, d2, "Damage variable, direction 22"
10, d6, "Damage variable, direction 12"
11, gf, "Fiber dissipated energy"
12, gm, "Matrix dissipated energy"
13, E11, "Direct strain, direction 11"
14, E22, "Direct strain, direction 22"
15, E33, "Direct strain, direction 33"
16, E12, "Shear strain, direction 12"
17, E13, "Shear strain, direction 13"
18, E23, "Shear strain, direction 23"
19, d3, "Damage variable direction 33"
20, STATUS, "Status of the element"

```

The material properties defined after the \*USER MATERIAL command are shown in Table 3.3.

The state variables used are shown in Table 4.2.

Table 4.2 State variables.

STATEV(1)	$r_{1+}$	Damage threshold function
STATEV(2)	$r_{2+}$	Damage threshold function
STATEV(3)	$r_{1-}$	Damage threshold function
STATEV(4)	$r_{2-}$	Damage threshold function
STATEV(5)	$A_{1-}$	Adjustment constant
STATEV(6)	$A_{2+}$	Adjustment constant
STATEV(7)	$A_{2-}$	Adjustment constant
STATEV(8)	$d_1$	Damage variable
STATEV(9)	$d_2$	Damage variable
STATEV(10)	$d_6$	Damage variable
STATEV(11)	$g_1$	Energy dissipated
STATEV(12)	$g_2 + g_6$	Energy dissipated
STATEV(13)	$\varepsilon_{11}$	11-component of the strain tensor
STATEV(14)	$\varepsilon_{22}$	22-component of the strain tensor
STATEV(15)	$\varepsilon_{33}$	33-component of the strain tensor
STATEV(16)	$\varepsilon_{12}$	12-component of the strain tensor
STATEV(17)	$\varepsilon_{13}$	13-component of the strain tensor
STATEV(18)	$\varepsilon_{23}$	23-component of the strain tensor
STATEV(19)	$d_3$	Damage variable
STATEV(20)	STATUS	Status of the element

### Initial conditions

The model requires the definition of the initial values of the state variables. Therefore, the `jobname.inp` file must include the following command:

```

** 3D elements
** ELSET, rfT, rmT, rfC, rmC, AfC, AmT, AmC,
** d1, d2, d6, gf, gm, e11, e22, e33,
** e12, e13, e23, STATUS
**
*Initial Conditions, Type=Solution
<elset>, 1.0, 1.0, 1.0, 1.0, -1.0, -1.0, -1.0,
0.0, 0.0, 0.0, 0.0, 0.0, 0.0, 0.0, 0.0,
0.0, 0.0, 0.0, 0.0, 1.0

```

## 4.3 Example

An ABAQUS® model with an example of the use of the **VUMAT** subroutine in the strength prediction of a Hexcel IM7-8552 [ $\pm 45_8$ ] CFRP laminate under a low-velocity impact can be downloaded from the following URL:

[www.fe.up.pt/~pcamanho/Impact\\_Test.inp](http://www.fe.up.pt/~pcamanho/Impact_Test.inp)  
[www.fe.up.pt/~pcamanho/Laminate\\_Solid\\_Test.icl](http://www.fe.up.pt/~pcamanho/Laminate_Solid_Test.icl)

The model of the composite plies is created using ABAQUS® C3D8 solid elements and it represents a 2mm thick, 100mm×100mm square specimen, as shown in Figure 4-1.

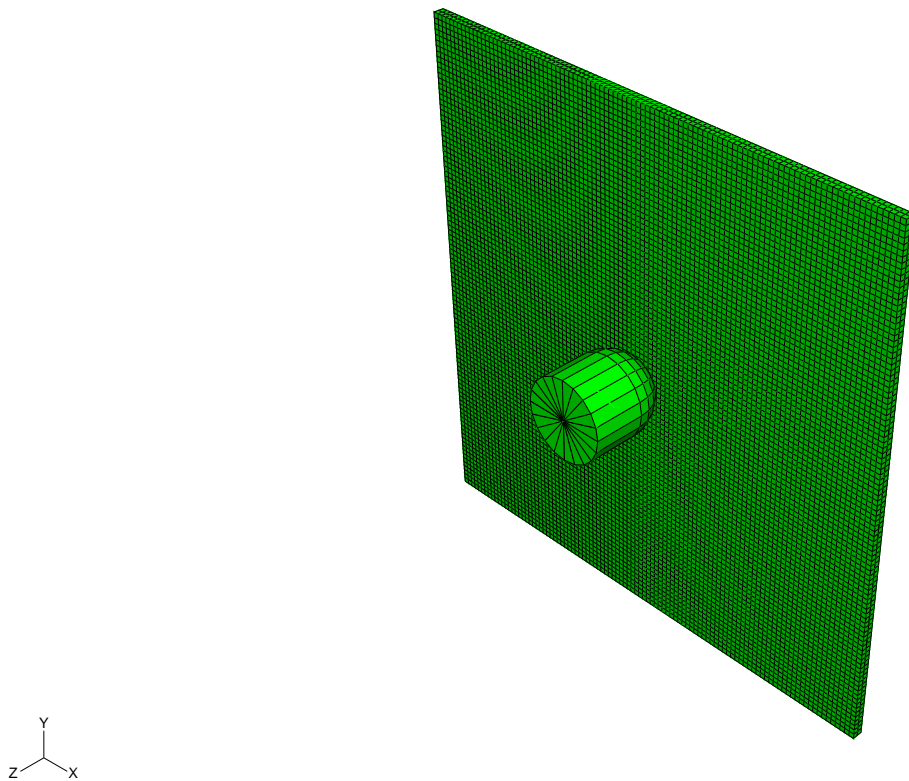


Figure 4-1 Specimen and impactor.

The impact results from the contact of the specimen with a semi-spherical rigid body with a diameter of 16mm, mass of 1kg, initial velocity of 4m/s, corresponding to an impact energy of 8J. The composite specimen is clamped along all edges. The material properties used are shown in Tables 3.4-3.6. In addition to the simulation of ply failure mechanisms by means of the subroutine **VUMAT**, the separation between the +45 and -45 plies (delamination) is simulated using another **VUMAT** subroutine where a cohesive formulation previously proposed is implemented in ABAQUS® solid cohesive elements [12].

Figure 4-2 shows the predicted delaminated region at the interface between the +45 and -45 plies. The damage variable  $d_6$  in the  $-45^\circ$ , corresponding to the back-face of the laminate, is shown in Figure 4-3.

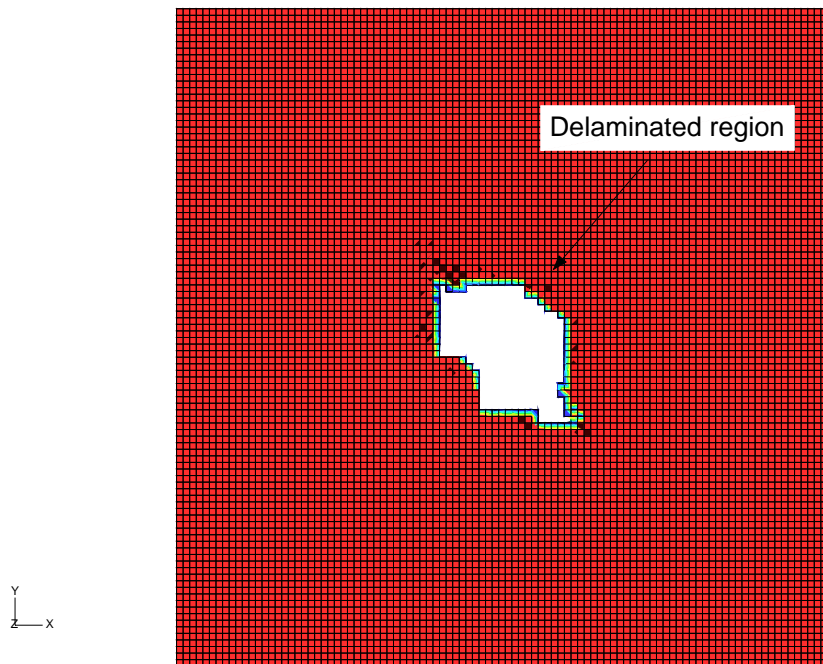


Figure 4-2 Predicted delamination.

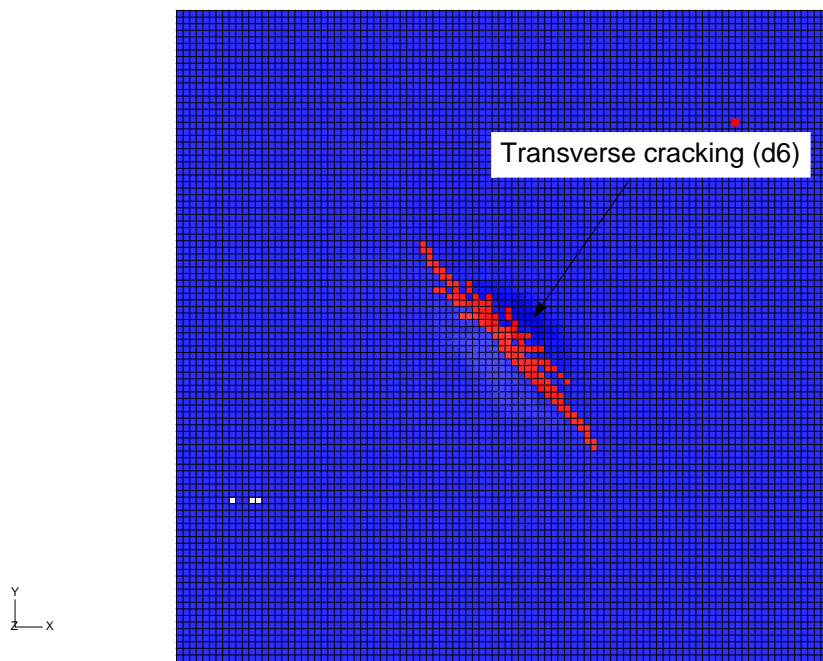


Figure 4-3 Predicted transverse matrix cracking in the laminate back-face.

Figure 4-4 shows the damage on the top (+45) ply, at the contact region between the impactor and the laminate.

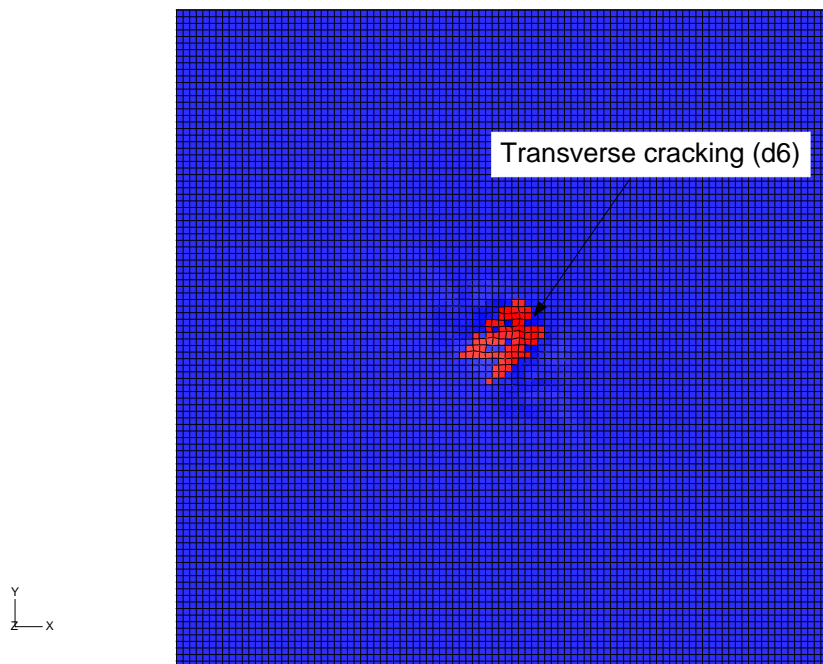


Figure 4-4 Predicted transverse matrix cracking in the contact region between the impactor and laminate.

The preliminary results obtained in this example indicate that the model developed is able to simulate the interaction between the failure mechanisms. In addition, the implementation of the material model in ABAQUS® explicit renders the solution of complex dynamic problems involving contact and failure possible.

## 5. CONCLUSIONS

---

A new ABAQUS® **UVARM** subroutine with the computational implementation of the LaRC failure criteria was developed in the first phase of this project. This subroutine predicts first ply failure, and it may be used for the preliminary analysis of composite structures, for the identification of critical regions of such structures, and in the design of structures where no type of damage is acceptable (e.g. cryogenic fuel tanks).

A continuum damage model able to predict the onset and propagation of intralaminar failure mechanisms was developed and implemented in both **UMAT** and **VUMAT** ABAQUS® subroutines. The model may be used in both shell and three-dimensional continuum elements using ABAQUS® implicit (**UMAT**) and ABAQUS® explicit (**VUMAT**). The computational models were implemented according to the requirements established in the beginning of the project:

- *Accurate prediction of damage onset.* The failure criteria implemented is able to represent the following characteristics of the mechanical behavior of laminated composite materials: i) in-situ effects, i.e. the effective increase of the transverse tensile and in-plane shear strengths of a ply when it is embedded in a multidirectional laminate; ii) the beneficial effect of transverse compression on the apparent shear strength of a ply; and iii) the effect of the shear stresses on fiber kinking.
- *Crack closure under load reversal.* The continuum damage model implements an unilateral representation of cracks, allowing the load path continuity to be recovered when cracks close under compressive loads.
- *Residual thermal stresses.* The constitutive model represents the effects of the residual thermal stresses in the plies of a multidirectional laminate.
- *Standard material properties.* The majority of the material properties required by the model can be obtained from standard test methods.
- *Ply-level properties.* The model uses ply properties, thus avoiding the need to test laminates every time the lay-up or stacking sequence is modified.
- *Regularization of energy dissipated.* The model avoids mesh dependency problems and assures the objectivity of the numerical solution by accounting for the toughnesses of the material in each damage mode as well as the energy dissipated by damage at a material integration point. In addition, procedures to rapidly assess adequacy of the mesh resolution and to provide corrective means when maximum mesh size requirements cannot be met were proposed.
- *Explicitly integrated constitutive model.* The model does not require iterations to solve the constitutive equations, being therefore suitable to be used in large scale computations.



- *Fast convergence rate of numerical solution.* The model includes stabilization methods that mitigate the problem of slow convergence rate of models involving strain-softening.

It was also shown that the continuum damage model used in shell elements is able to predict the effect of size on the strength of quasi-isotropic CFRP laminates. In addition, the preliminary validation example of a low-velocity impact load on a CFRP laminate indicates that the combination of a ply-based damage model and a cohesive formulation for the simulation of delamination is a strategy that may capture the interaction between these different failure mechanisms.

Future work should address the issues related to the mesh-dependent directionality of crack propagation that is often observed in continuum damage models. This problem may be mitigated by using an improved kinematic representation of the failure mechanisms, such as the transversely isotropic damage model presented in [13] and presented in Appendix D (the full development of this model was planned for the second year of the project).

# Bibliography

- [1] Dassault Systemes. 2006. ABAQUS 6.7 User's Manuals.
- [2] Camanho, P. P.; Dávila, C. G.; Pinho, S. T.; Iannucci, L., and Robinson, P. Prediction of in situ strengths and matrix cracking in composites under transverse tension and in-plane shear. *Composites-Part A*. 2005; 37:165-176.
- [3] Dávila, C. G.; Camanho, P. P., and Rose, C. A. Failure criteria for FRP laminates. *Journal of Composite Materials*. 2005; 39:323-345.
- [4] Dávila, C. G and Camanho, P. P. Failure Criteria for FRP Laminates in Plane Stress. NASA/TM-2003-212663. National Aeronautics and Space Administration; 2003.
- [5] Pinho, S. T.; Dávila, C. G.; Camanho, P. P.; Iannucci, L., and Robinson, P. Failure models and criteria for FRP under in-plane shear or three-dimensional stress states including shear non-linearity. NASA/TM-2005-213530. 2005.
- [6] Parvizi, A.; Garrett, K., and Bailey, J. Constrained cracking in glass fibre-reinforced epoxy cross-ply laminates, *Journal of Material Science*. 1978; 13:195-201.
- [7] Dvorak, G. J. and Laws, N. Analysis of progressive matrix cracking in composite laminates II. first ply failure. *Journal of Composite Materials*. 1987; 21:309-329.
- [8] Maimí, P.; Camanho, P.P., Mayugo, J.A. and Dávila C.G. A thermodynamically consistent damage model for advanced composites. NASA Technical Memorandum 214282. National Aeronautics and Space Administration, 2006.
- [9] Maimí, P.; Camanho, P.P., Mayugo, J.A. and Dávila, C.G. A continuum damage model for composite laminates: part I - constitutive model. *Mechanics of Materials*. 2007; 39:897-908.
- [10] Maimí, P.; Camanho, P.P., Mayugo, J.A. and Dávila, C.G. A continuum damage model for composite laminates: part II - computational implementation and validation. *Mechanics of Materials*. 2007; 39:909-919.
- [11] Camanho, P.P.; Maimí, P. and Dávila, C.G. Prediction of size effects in notched laminates using continuum damage mechanics. *Composites Science and Technology*. 2007; 67:2715-2727.

- [12] Gonzalez, E.V., Maimí, P., Turon, A., Camanho, P.P., Renart, J. Simulation of delamination by means of cohesive elements using an explicit finite element code, *Computers, Materials and Continua*. 2008; submitted for publication.
- [13] Maimí, P., Camanho, P.P., Mayugo, J.A. A three-dimensional damage model for transversely isotropic composite laminates. *Journal of Composite Materials*. 2008; in press.

# Appendix A: LaRC03-UVARM-v1 Fortran subroutine

```

      SUBROUTINE UVARM(UVAR,DIRECT,T,TIME,DTIME,CMNAME,ORNAME,
1  NUARM,NOEL,NPT,LAYER,KSPT,KSTEP,KINC,NDI,NSHR,COORD,
2  JMAC,JMATYP,MATLAYO,LACCFLA)
C
      INCLUDE 'ABA_PARAM.INC'
C
      common/crdflg/lrdflg
C
      CHARACTER*80 CMNAME,ORNAME,CMNAME1
      CHARACTER*3 FLGRAY(15)
      CHARACTER xoutdir*255, xfname*80
      CHARACTER dmurname*255, FNAMEX*80
      DIMENSION UVAR(*),DIRECT(3,3),T(3,3),TIME(2)
      DIMENSION ARRAY(15),JARRAY(15),JMAC(*),JMATYP(*),COORD(*)
C
      DIMENSION stress(6)
C      The dimensions of the variables FLGRAY, ARRAY and JARRAY
C must be set equal to or greater than 15.
      double precision alphao,alphamem(1),psimem(1),thetamem(1),
1      omega(1),lambda(1),
2      fmat(1),fkink(1),fft(1),epsmato(1),
3      sigmato(1),epskinko(1),sigkinko(1),epsfto(1),
4      sig1(1),sig2(1),sig3(1),tau12(1),tau23(1),tau31(1),
5      eps1(1),eps2(1),eps3(1),eps12(1),eps23(1),eps31(1),
6      s12,s23,fio,beta
C
      integer lft,llt
C
      pi=dacos(-1.d0)
      degtorad=pi/180.d0
C
      do i=1,nuvarm
         uvar(i) = 0.d0
      enddo
C
      -----
C      Open and read input file with material properties:
C directory/jobname.mt
      -----
      lxfname = 0
      lxoutdir = 0
      xfname = ' '
      xoutdir = ' '
C
```

```

call getjobname(xfname,lxfname)      ! input file name
call getoutdir(xoutdir,lxoutdir)    ! output directory
C
if(lrdflg.ne.1) then
  fname=dmkname(xfname(1:lxfname),xoutdir(1:lxoutdir),'.mt')
  open(unit=17,file=fname,status='old')
  lrdflg = 1
endif
C
read (17,*)
read (17,*) klarc
C
CMNAME1='**dummy_name**'
do while(CMNAME1.NE.CMNAME)      ! search for material type
  read (17,*)
  read (17,*) CMNAME1
  if(CMNAME1.EQ.CMNAME) then
    read (17,*)
    read (17,*) ym1, ym2, ym3, nu21, nu31, nu32
    read (17,*)
    read (17,*) g12, g23, g31, xt, xc, yt, yc, s12
    read (17,*)
    read (17,*) alphao, beta, g, slis
  else
    do i=1,6
      read(17,*)
    enddo
  endif
enddo
C
rewind 17
C
-----
C    Compute derived material properties
-----
  alphao=alphao*degtorad
  st=yc*dcos(alphao)*(dsin(alphao)+dcos(alphao)/dtan(2.d0*alphao))
  s23=st
  s1=s12
  etat=-1.d0/dtan(2.d0*alphao)
  etal=-s12*dcos(2*alphao)/(yc*dcos(alphao)*dcos(alphao))
C
-----
C    Read stress tensor from current increment
-----
  CALL GETVRM('S',ARRAY,JARRAY,FLGRAY,JRCD,JMAC,JMATYP,MATLAYO,
1          LACCFLA)
C

```



```

-----
      IF(S22.GT.0.D0) THEN                                ! matrix tension
      IF(S11.LT.0.D0.AND.DABS(S11).LT.XC/2) THEN
      CALL ROTATE_PHI(SL,XC,ETA_L,S11,S22,S12,0.D0,0.D0,
1      S11_M,S22_M,S12_M,S13_M,S23_M,G12,NDIM)
      FIP(1) = (1-G)*S22_M/YT+G*S22_M/YT*S22_M/YT+S12_M/SL_IS*
1      S12_M/SL_IS
      ELSE
      FIP(2) = (1-G)*S22/YT+G*S22/YT*S22/YT+S12/SL_IS*S12/SL_IS
      ENDIF
C
      ELSE                                                ! matrix compression
      IF(S11.GE.-YC) THEN
      FIP(3) = FLARC03(ALPHA,S22,S12,ETA_L,ETA_T,SL_IS,ST,PI)
      ELSE
      CALL ROTATE_PHI(SL,XC,ETA_L,S11,S22,S12,0.D0,0.D0,
1      S11_M,S22_M,S12_M,S13_M,S23_M,G12,NDIM)
      FIP(4) = FLARC03(ALPHA,S22_M,S12_M,ETA_L,ETA_T,SL_IS,ST,PI)
      ENDIF
      ENDIF
C-----
*
*      Longitudinal (fibre)
* C
-----

      IF(S11.GE.0.D0) THEN                                ! fibre tension
      FIP(5) = S11/XT
C
      ELSE                                                ! fibre compression
      CALL ROTATE_PHI(SL,XC,ETA_L,S11,S22,S12,0.D0,0.D0,
1      S11_M,S22_M,S12_M,S13_M,S23_M,G12,NDIM)
      IF(S22_M.LT.0.D0) THEN
      FIP(6) = FMCCAULEY((DABS(S12_M)+ETA_L*S22_M)/SL_IS) ! LaRC#4
      ELSEIF (DABS(S11).GE.XC/2.D0) THEN
      FIP(7) = (1-G)*S22_M/YT+G*S22_M/YT*S22_M/YT+S12_M/SL_IS
1      *S12_M/SL_IS
      ENDIF
      ENDIF
C
      FI(1) = MAX(FIP(1),FIP(2))    ! Transverse with S22>0
C
      FI(2) = MAX(FIP(3),FIP(4))    ! Transverse with S22<0
C
      FI(3) = FIP(5)                ! Longitudinal with S11>0
C
      FI(4) = MAX(FIP(6),FIP(7))    ! Longitudinal with S11<0
C
-----

```









## Appendix B: Paper published in Composites Science and Technology

# Prediction of size effects in notched laminates using continuum damage mechanics

P.P. Camanho<sup>a,\*</sup>, P. Maimí<sup>b</sup>, C.G. Dávila<sup>c</sup>

<sup>a</sup> *DEMEGI, Faculdade de Engenharia, Universidade do Porto, Rua Dr. Roberto Frias, 4200-465 Porto, Portugal*

<sup>b</sup> *AMADE, University of Girona, Campus Montilivi s/n, Girona, Spain*

<sup>c</sup> *NASA Langley Research Center, Hampton, VA, USA*

Received 2 November 2006; received in revised form 12 February 2007; accepted 12 February 2007

Available online 25 February 2007

## Abstract

This paper examines the use of a continuum damage model to predict strength and size effects in notched carbon–epoxy laminates. The effects of size and the development of a fracture process zone before final failure are identified in an experimental program. The continuum damage model is described and the resulting predictions of size effects are compared with alternative approaches: the point stress and the inherent flaw models, the Linear Elastic Fracture Mechanics approach, and the strength of materials approach. The results indicate that the continuum damage model is the most accurate technique to predict size effects in composites. Furthermore, the continuum damage model does not require any calibration and it is applicable to general geometries and boundary conditions.  
© 2007 Elsevier Ltd. All rights reserved.

**Keywords:** Size effect; C. Continuum damage mechanics; Fracture mechanics

## 1. Introduction

The introduction of advanced composite materials in new applications relies on the development of accurate analytical and computational tools that are able to predict the thermo-mechanical response of composites under general loading conditions and geometries. In the absence of accurate analytical models, the design process has to rely on costly matrices of mechanical tests based on large numbers of test specimens [1] and empirical knockdown factors [2].

The prediction of ultimate strength remains the main challenge in the simulation of the mechanical response of composite materials [3]. The simulation of size effects on the strength of composites is of particular interest and relevance [4–8]; reliable analytical and numerical models must represent the decrease of the ultimate strength when the structural dimensions increase [9].

Size effects in laminated composites occur at different material and structural levels. At the meso-mechanical level, it is observed that the transverse tensile and in-plane shear strengths of a ply constrained by sublaminae depend on the ply thickness [10]. This size effect is normally called the “in situ” effect and can be accounted for in the prediction of matrix cracking onset using the “in situ” strengths in appropriate failure criteria. The “in situ” strengths can be calculated from analytical closed-form solutions using ply elastic properties and fracture energies [11,12].

Size effects also occur at the macro-mechanical level. For example, it is shown in [13] that the strength of notched quasi-isotropic composite laminates decreases for increasing notch sizes when thin plies are used. This effect, usually known as the “hole size effect”, is caused by the development and propagation of non-critical ply-level damage mechanisms that occur in the vicinity of the hole before the final collapse of the laminate. The exact nature of the non-critical damage mechanisms has been reported by several authors. Using Moiré interferometry in notched

\* Corresponding author. Tel.: +351 225081753; fax: +351 225081315.  
E-mail address: [pcamanho@fe.up.pt](mailto:pcamanho@fe.up.pt) (P.P. Camanho).

$[0/+45/90/-45]_s$  laminates, Mollenhauer et al. [14] observed a strain redistribution as a result of matrix–fiber splitting in the  $0^\circ$  surface ply and sub-surface ply cracking. Green et al. [4] reported fiber splitting in the  $0^\circ$  plies, matrix cracking in the off-axis plies, and delamination in  $[+45_m/90_m/-45_m/0_m]_{ns}$  carbon–epoxy laminates with a central circular hole.

The observed ply-level damage mechanisms can be regarded as a fracture process zone that develops before final failure of the laminate. For very small specimens, the fracture process zone affects the entire width of the laminate. On the other hand, the size of the fracture process zone in large specimens is negligible when compared with the characteristic dimensions of the specimen. The relative dimension of the fracture process zone with respect to the specimen size justifies the different strengths observed in small and large specimens. Therefore, to predict the hole size effect in quasi-brittle materials with general dimensions, methods that account for the energy dissipated by the propagation of non-critical damage mechanisms are required [15].

While the strength of notched multidirectional laminates manufactured using thin plies generally decreases with hole diameter, Green et al. [4] reported an opposite trend for laminates with plies with the same fiber orientation blocked together (ply-level scaling): for a 4 mm thick  $[45_4/90_4/-45_4/0_4]_s$  carbon fiber reinforced plastic (CFRP) laminate, increasing the hole size from 3.2 mm to 25.4 mm increased the strength by 51%. This new finding was attributed to the formation of delaminations at the edge of the hole [4]. Ply-blocked specimens exhibit a delamination type of failure, and for small hole diameters the size of the delamination is relatively large and grows unstably.

Green et al. also performed tests on thickness-scaled CFRP laminates [4]. A decrease of the ultimate strength with test specimen thickness was reported for both ply-level and sublaminates-level scaled laminates, where the laminate thickness is increased by increasing the number of sublaminate while keeping the ply thickness constant. When increasing the thickness from 1 mm to 8 mm, strength reductions of 16.5% and 64.4% were measured for the sublaminates level and ply-level scaled specimens, respectively. The strength reduction was attributed to the higher energy release rate at the interfaces of the ply-level scaled specimens, which promotes delamination, and to the higher stress concentration relief that occurs as a result of damage in the surface plies of sublaminates-level scaled specimens.

The calculation of macro-mechanical size effects is often based on semi-empirical methods that require calibration such as the point stress and average stress models proposed by Whitney and Nuismer [16]. The point stress model assumes that final failure occurs when the stress at a characteristic distance from the notch reaches the unnotched strength of the laminate. In the average stress model, it is assumed that final failure occurs when the laminate stress averaged over a characteristic distance is equal to the unnotched strength of the laminate. Modifications of the

point stress and average stress models using ply strengths have been proposed to predict the strength of laminates with open and loaded holes [17,18]. The advantage of using ply properties rather than laminate properties is that the need to measure laminate strengths for every layup is avoided. However, the measurement of the characteristic distances is still required for each lay-up and geometry [18].

On the other hand, models based on continuum damage mechanics do not require calibration, so they potentially provide the means for a truly predictive methodology for the strength prediction of composite laminates. Continuum damage models are defined in the framework of the thermodynamics of irreversible processes. Generally speaking, the formulation of continuum damage models starts by the definition of a potential (e.g. the complementary free energy) as a function of one or more damage variables that is the basis for establishing the relation between the stress and the strain tensors. It is also required to define the damage activation functions, i.e. the conditions that lead to the onset of inelastic response, and the damage evolution functions. Some of the models proposed in the literature are exclusively based on thermodynamic restrictions of the constitutive model and on some adjusting functions for damage onset and evolution. Other models, besides satisfying the thermodynamic restrictions, are based on the failure mechanisms [19], i.e. the damage activation functions are related to the physics of the different failure mechanisms, and the damage variables are related to the orientation of the ply failure planes experimentally observed. Mechanism-based continuum damage models can predict damage onset and the extent and type of non-critical damage mechanisms. Furthermore, continuum damage models that relate the damage variables to the normal components of the stress tensor are able to simulate the effect of crack closure under load reversal cycles. Therefore, such models can be used to predict the strength under non-monotonic loading including load reversals.

The objective of this paper is to investigate the use of a continuum damage model for the prediction of size effects in notched carbon–epoxy laminates loaded in tension. An experimental program is conducted to measure the relevant material properties and to identify size effects occurring in laminates with different hole sizes. The recently proposed continuum damage model is described and analysis of open hole specimens subjected to tension loads are presented. The analyses results are compared with the experimental data and with predictions obtained using a strength of materials approach, Linear Elastic Fracture Mechanics, and the point stress model.

## 2. Experimental program

### 2.1. Material selection and characterization

The material selected for the present study is Hexcel's IM7-8552 carbon epoxy unidirectional tape with a nominal ply thickness of 0.131 mm. The material was cured accord-

ing to the manufacturer's specifications, with temperature stages of 110 °C for 1 h, followed by 180 °C for 2 h. A pressure of 7 bar was applied for the duration of the cure cycle.

The fiber volume fraction was measured using image processing techniques resulting in an average value of 59.1%. The coefficients of thermal expansion were measured using a dilatometer and the resulting values are  $\alpha_{11} = -5.5 \times 10^{-6}/^{\circ}\text{C}$  for the longitudinal direction, and  $\alpha_{22} = 25.8 \times 10^{-6}/^{\circ}\text{C}$  for the transverse direction. The elastic properties and strengths were measured using ASTM test standards [20–22]. Five specimens were used for each test performed.

The mean measured values of the ply elastic properties are shown in Table 1.  $E_1$  and  $E_2$  are the longitudinal and transverse Young's modulus respectively,  $G_{12}$  is the shear modulus, and  $\nu_{12}$  is the major Poisson's ratio. Table 1 also presents the standard used in each test, the standard deviation (STDV), and the coefficient of variation (CV).

The measured ply strengths are shown in Table 2.  $X_T$  and  $Y_T^{\text{ud}}$  are the longitudinal and transverse tensile strengths, respectively.  $X_C$  and  $Y_C$  are the longitudinal and transverse compressive strengths, respectively.  $S_L^{\text{ud}}$  is the in-plane shear strength.

The values of the transverse tensile strength ( $Y_T^{\text{ud}}$ ) and of the in-plane shear strength ( $S_L^{\text{ud}}$ ) measured in the test specimens correspond to the strengths of unconstrained unidirectional plies. The transverse tensile and shear strengths of constrained plies (in situ strengths) are higher than the ones of an unidirectional ply [10] and decrease when increasing the ply thickness. The in situ strengths are calculated using models previously proposed by the authors, which are based on the mode I fracture toughness,  $G_{2+}$ , and on the mode II fracture toughness,  $G_6$  [12]. These models use the simplifying assumption that the in situ strengths are not a function of the elastic properties and geometry of the neighboring layers.

To measure the components of the fracture toughness, double cantilever beam (DCB) [23] and four-point bending end notched flexure (4-ENF) [24] tests were performed. The measured components of the fracture toughness are shown in Table 3.

The in situ strengths are calculated as functions of the fracture toughness and ply elastic properties using the models described in [12] with a shear response factor  $\beta = 2.98 \times 10^{-8} \text{ MPa}^{-3}$ . The calculated in situ strengths are shown in Table 4.

The shear strength in the transverse direction is calculated as [25,26]

Table 2  
Measured ply strengths for IM7-8552

Property	Standard	Mean value (MPa)	STDV (MPa)	CV (%)
$X_T$	Ref. [20]	2326.2	134.1	5.8
$X_C$	Ref. [21]	1200.1	145.7	12.1
$Y_T^{\text{ud}}$	Ref. [20]	62.3	5.3	8.5
$Y_C$	Ref. [21]	199.8	20.5	10.2
$S_L^{\text{ud}}$	Ref. [22]	92.3	0.6	0.7

Table 3  
Measured fracture energies for transverse fracture for IM7-8552 (kJ/m<sup>2</sup>)

Property	Mean value	STDV	CV (%)
$G_{2+}$	0.2774	0.0246	0.88
$G_6$	0.7879	0.0803	10.19

Table 4  
Calculated in situ strengths for IM7-8552 (MPa)

Ply configuration	$Y_T$	$S_L$
Thin embedded ply	160.2	130.2
Thin outer ply	101.4	107.0

$$S_T = Y_C \cos \alpha_0 \left( \sin \alpha_0 + \frac{\cos \alpha_0}{\tan 2\alpha_0} \right) \quad (1)$$

where  $\alpha_0$  is the fracture angle of a ply under pure transverse compression [27]. For a fracture angle  $\alpha_0 = 53^{\circ}$ , the shear strength in the transverse direction is calculated as  $S_T = 75.3 \text{ MPa}$ .

The continuum damage model also requires the fracture energies per unit surface for longitudinal failure,  $G_{1+}$  (tension) and  $G_{1-}$  (compression). These energies were measured using the Compact Tension (CT) and Compact Compression (CC) tests in cross-ply laminates proposed by Pinho et al. [28,29]. The measured fracture energies per unit surface are shown in Table 5.

## 2.2. Notched laminates

Tests of notched composite laminates were performed to quantify the size effect and to obtain empirical data to validate the numerical model. Quasi-isotropic laminates were manufactured in Hexcel IM7-8552 CFRP with a stacking sequence of  $[90/0/\pm 45]_{3s}$ .

The unnotched tensile strength of the laminate,  $X_T^L$ , was measured using five test specimens and the average value obtained was 845.1 MPa. The average value of the failure strain,  $12,900\mu\epsilon$ , was measured in the five test specimens using strain gauges.

Table 1  
Measured ply elastic properties for IM7-8552

Property	Standard	Mean value	STDV	CV (%)
$E_1$ (GPa)	Ref. [20]	171.42	2.38	1.39
$E_2$ (GPa)	Ref. [20]	9.08	0.09	1.03
$G_{12}$ (GPa)	Ref. [22]	5.29	0.13	2.53
$\nu_{12}$	Ref. [20]	0.32	0.02	6.18

Table 5  
Measured fracture energies for longitudinal fracture for IM7-8552 (kJ/m<sup>2</sup>)

Property	Mean value	STDV	CV (%)
$G_{1+}$	81.5	6.1	7.6
$G_{1-}$	106.3	2.2	2.1

The notched test specimens were machined using a procedure that prevents delaminations in the regions close to the insertion point and the exit of the drill bit. Sacrificial frontal and backing plates were used to clamp the specimens during the drilling process. All test specimens were machined to class 1 hole quality used in aerospace [30]. No damage was observed in a sample of test specimens inspected using X-rays.

Specimens with five different hole diameters,  $d = 2$  mm, 4 mm, 6 mm, 8 mm, 10 mm and with a width-to-diameter ratio  $w/d$  equal to 6 were tested in a MTS servo-hydraulic machine following the ASTM D-5766 standard [31] according to the test matrix shown in Table 6. Five specimens were tested for each geometry.

The specimens labeled OHT3, OHT6 and OHT9 were instrumented with two strain gages in the positions schematically shown in Fig. 1.

The distances  $d_s$  shown in Fig. 1 are respectively 10.5 mm, 13.5 mm, and 12.5 mm for the test specimens OHT3, OHT6 and OHT9. The specimens OHT10 and OHT11 were not instrumented. Acoustic emission (AE) sensors were used in one test specimen for each size.

Table 6  
Open hole tension test matrix

Specimen ref.	$d$ (mm)	$w$ (mm)	$w/d$
OHT11	2	12	6
OHT10	4	24	6
OHT3	6	36	6
OHT6	8	48	6
OHT9	10	60	6

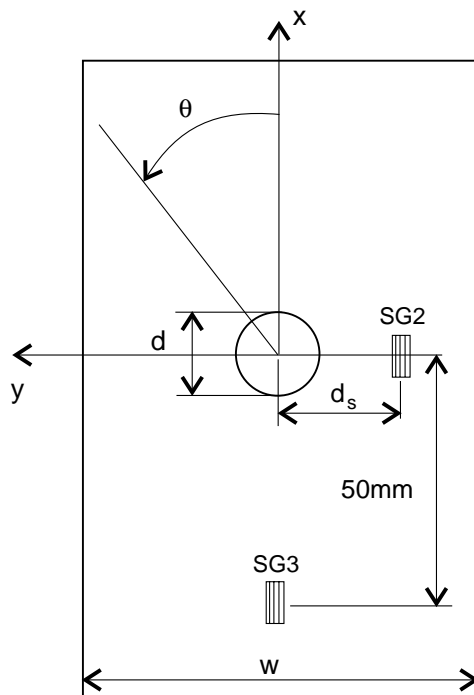


Fig. 1. Position of strain gages.

Fig. 2 shows the applied load and the cumulative number of AE signals as a function of time for one OHT3 test specimen.

From the AE signals shown in Fig. 2, it can be concluded that non-critical damage mechanisms accumulate well before final failure of the specimen, creating a fracture process zone (FPZ). Similar results are observed in the OHT6 and OHT9 specimens, as well as in other experimental investigations [4,14].

The remote failure stress is defined using the failure load measured in the tests ( $\bar{P}$ ) and the measured values of the specimen thickness ( $t_L$ ) and width ( $w$ ) as:  $\bar{\sigma}^\infty = \frac{\bar{P}}{wt_L}$ . The remote failure stresses obtained for the different geometries are summarized in Table 7.

The failure mode observed in all specimens is net-section tension, as shown in Fig. 3. Fig. 4 shows the relation between the remote stress and the strain measured by strain gages SG3 for one test specimen of each of the three different geometries.

The experimental results presented in Table 7 clearly identify a size effect: an increase in the hole diameter from 2 mm to 10 mm results in a 32.8% reduction in the strength. The observed size effect is caused by the development of the fracture process zone identified in the AE results, which redistributes the stresses and dissipates energy. In small specimens, the fracture process zone extends towards the edges of the specimen and the average stress at the fracture plane tends to the unnotched strength of the laminate.

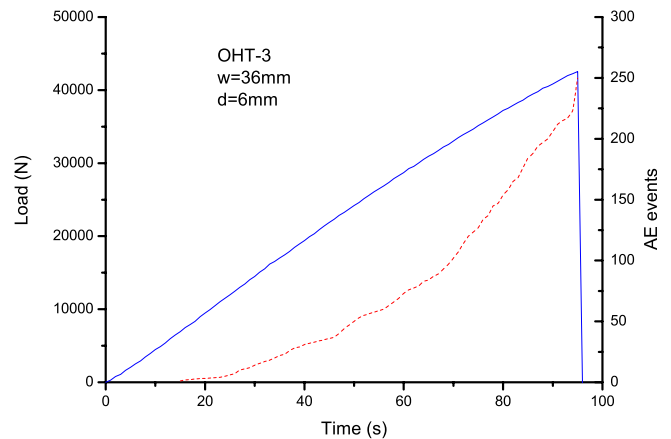


Fig. 2. Applied load and AE signals as a function of time for the specimen with a 6 mm diameter hole.

Table 7  
Results of open-hole tensile tests

Hole diameter (mm)	$\bar{\sigma}^\infty$ (MPa)	STDV (MPa)	CV (%)
2	555.7	15.3	2.8
4	480.6	21.4	4.5
6	438.7	25.3	5.8
8	375.7	15.1	4.0
10	373.7	14.1	3.8



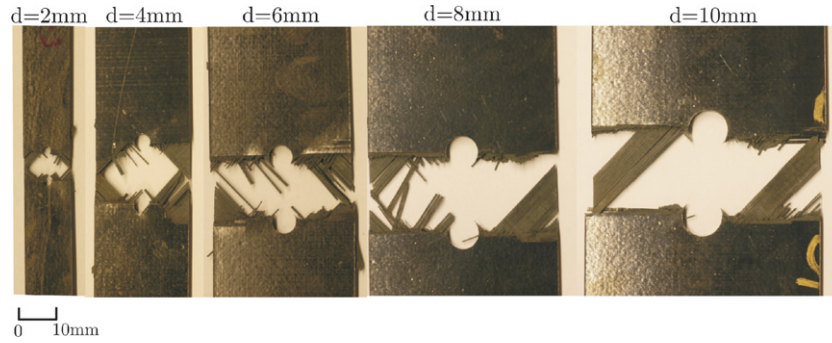
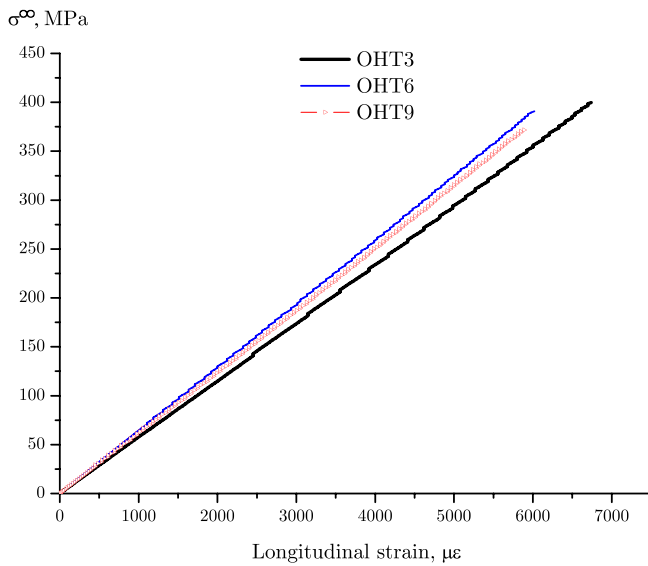
Fig. 3. Net-section tension failures in specimens with  $w/d = 6$ .

Fig. 4. Relation between remote stress and longitudinal strain in SG3.

The effect of size on the strength can be explained using a simple example based on the cohesive crack model, which is well-suited to simulate fracture of quasi-brittle materials [32]. Consider that the fracture process zone is represented by a cohesive crack with the simple constitutive relation shown in Fig. 5a.

The cohesive constitutive model relates the laminate cohesive stress,  $\sigma$ , to the crack opening,  $w$ , and must satisfy the following condition:  $\int_0^\infty \sigma(w) dw = G_C$ . Structural collapse occurs when a point along the fracture plane reaches the critical opening,  $w_c$ , and the corresponding length of

the fracture process zone can be estimated using the Irwin model as  $l_{FPZ} \approx \frac{EG_C}{\pi(X_T^L)^2}$  [33,34].

Based on the constitutive law shown in Fig. 5a, it is possible to schematically represent the stress distribution at failure along the fracture planes of specimens with different sizes, as shown in Fig. 5b. It is observed that in small specimens the fracture process zone extends towards the edges, whereas in large specimens the fracture process zone is confined to the vicinity of the hole. As a consequence, the average stress acting on the fracture plane, and hence the strength, are larger for small specimens.

### 3. Simulation of the effect of size on strength

Strength prediction methods uniquely based on stress or strain failure criteria are unable to predict the size effects observed in notched specimens. Consider for example a calculation of the final failure of a specimen with a central hole using the value of the longitudinal stress in the fiber direction (maximum stress criterion). The distribution of the longitudinal stress in the critical plies, the  $0^\circ$  plies along the fracture plane, defined by  $\theta = 90^\circ$  in Fig. 1, can be calculated using an approximate closed-form solution as [35]

$$\sigma_{11} = \sigma_{xx}(0, y) (\bar{Q}_{11} a_{11}^* + \bar{Q}_{12} a_{12}^*) \quad (2)$$

where  $a_{ij}^*$  are the components of the laminate compliance matrix defined as [36]

$$[a^*] = t_L [A]^{-1} \quad (3)$$

where the matrix  $[A]$  relates the in-plane forces per unit length to the mid-plane strains.  $\bar{Q}_{ij}$  are the components of the plane stress transformed reduced stiffness matrix of the  $0^\circ$  plies [18], and  $t_L$  is the thickness of the laminate.

The through-the-thickness averaged normal stress in the fracture plane for a quasi-isotropic laminate is calculated by Tan [35] as

$$\sigma_{xx}(0, y) = \frac{2 + (1 - d/w)^3}{6(1 - d/w)} \left[ 2 + \left( \frac{d}{2y} \right)^2 + 3 \left( \frac{d}{2y} \right)^4 \right] \sigma_{xx}^\infty, \quad y \geq d/2 \quad (4)$$

where  $\sigma_{xx}^\infty$  is the remote tensile stress.

From Eqs. (2) and (4) it is clear that for the same material and stacking sequence the stress concentration factor,

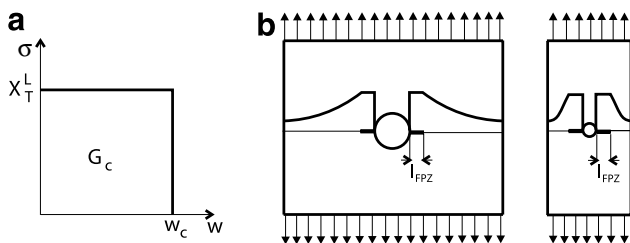


Fig. 5. Cohesive crack constitutive law and fracture process zone. (a) Constitutive model and (b) stress distributions along the fracture plane.



and hence the maximum longitudinal stress in the  $0^\circ$  ply, depends on the ratio between the specimen hole diameter and width. Applying the maximum stress criterion and using Eqs. (2) and (4)

$$\frac{\sigma_{11}}{X_T} = 1 \Rightarrow \bar{\sigma}^\infty = \frac{(1 - d/w)X_T}{[2 + (1 - d/w)^3](\bar{Q}_{11}a_{11}^* + \bar{Q}_{12}a_{12}^*)} \quad (5)$$

Eq. (5) demonstrates that the application of the maximum stress criterion results in the same strength prediction for different hole diameters when the  $d/w$  ratio is held constant. The lack of size effect on the predicted strength clearly contradicts the experimental observations.

### 3.1. Linear Elastic Fracture Mechanics

There are two approaches that can be used with Linear Elastic Fracture Mechanics (LEFM) to calculate the effect of size on the strength of notched composite laminates. In the first approach, it is assumed that the length  $a$  of a pre-existing crack in the laminate is scaled in the same proportion of the hole diameter and specimen width and that the critical value of the laminate's stress intensity factor,  $K_{Ic}$ , is independent of the crack length. Consider two specimens with hole diameters  $d_1$  and  $d_2$ . The stress intensity factor at failure is

$$K_{Ic} = \bar{\sigma}_1^\infty F\left(\frac{w_1}{d_1}, \frac{a_1}{d_1}\right) \sqrt{\pi a_1} = \bar{\sigma}_2^\infty F\left(\frac{w_2}{d_2}, \frac{a_2}{d_2}\right) \sqrt{\pi a_2} \quad (6)$$

Taking into account the fact that the crack length is proportional to the hole diameter and that the finite width correction factors,  $F(w/d, a/d)$ , are equal for scaled geometries, the failure stress of a specimen with a hole diameter  $d_2$  can be calculated from the failure stress of the specimen with a hole diameter  $d_1$

$$\bar{\sigma}_2^\infty = \bar{\sigma}_1^\infty \sqrt{\frac{d_1}{d_2}} \quad (7)$$

The second approach to predict size effects using LEFM is the inherent flaw model (IFM) proposed by Waddoups et al. [13]. It is considered that the non-critical damage mechanisms occurring before ultimate failure of a composite laminate can be lumped into a constant “region of intense energy”, or “inherent flaw”, of length  $a$ . The critical value of the stress intensity factor of a plate with a hole of radius  $R$  is given by

$$K_{Ic} = f(a, R) \bar{\sigma}^\infty \sqrt{\pi a} \quad (8)$$

where  $f(a, R)$  is Bowie's solution for the calculation of the stress intensity factor of two cracks emanating from a circular hole, given as [37,38]

$$f(a, R) = 0.5 \left( 3 - \frac{a}{d/2 + a} \right) \left[ 1 + 1.243 \left( 1 - \frac{a}{d/2 + a} \right)^3 \right] \quad (9)$$

Waddoups et al. [13] considered that the strength of an unnotched specimen can be predicted by taking into

account that the hole radius tends to zero, in which case the function  $f(a, R)$  tends to one, leaving

$$K_{Ic} = X_T^L \sqrt{\pi a} \quad (10)$$

where  $X_T^L$  is the tensile strength of the unnotched laminate.

From (8) and (10), the equation proposed by Waddoups et al. [13] is obtained

$$\bar{\sigma}^\infty = X_T^L / f(a, R) \quad (11)$$

The strength of the laminate containing an open-hole is predicted using two parameters: the length of the inherent flaw,  $a$ , that needs to be calculated from a baseline specimen, and the unnotched tensile strength of the laminate,  $X_T^L$ .

### 3.2. Point-stress model

The point-stress model (PSM) proposed by Whitney and Nuismer [16], considers that ultimate failure occurs when the stress at a given distance from the hole boundary,  $r_{ot}$ , reaches the unnotched strength of the laminate,  $X_T^L$ . An alternative version of the point stress model uses the ply stresses and strengths, so that it is not necessary to measure the strength for every different laminate.

Using Eqs. (2) and (4), the strength predicted using the PSM is

$$\bar{\sigma}^\infty = X_T \left\{ \frac{2 + (1 - \frac{d}{w})^3}{6(1 - \frac{d}{w})} \left[ 2 + \left( \frac{d}{d + 2r_{ot}} \right)^2 + 3 \left( \frac{d}{d + 2r_{ot}} \right)^4 \right] \times (\bar{Q}_{11}a_{11}^* + \bar{Q}_{12}a_{12}^*) \right\}^{-1} \quad (12)$$

Failure is predicted using two parameters: the characteristic distance in tension  $r_{ot}$ , and the longitudinal tensile strength of the ply,  $X_T$ .

### 3.3. Continuum damage model

Continuum damage mechanics is a methodology well suited for the simulation of damage evolution and ultimate failure of composites under general loads and boundary conditions for which no analytical solution is available. The continuum damage model used here is based on previous work by the authors [19,39,40]. The main aspects of the continuum damage model are presented in the following sections. The full details of the model can be found in Refs. [19,39,40].

#### 3.3.1. Constitutive model

The proposed definition for the complementary free energy density of a ply is

$$G = \frac{\sigma_{11}^2}{2(1 - d_1)E_1} + \frac{\sigma_{22}^2}{2(1 - d_2)E_2} - \frac{\nu_{12}}{E_1} \sigma_{11} \sigma_{22} + \frac{\sigma_{12}^2}{2(1 - d_6)G_{12}} + (\alpha_{11}\sigma_{11} + \alpha_{22}\sigma_{22})\Delta T + (\beta_{11}\sigma_{11} + \beta_{22}\sigma_{22})\Delta M \quad (13)$$

where the damage variable  $d_1$  is associated with longitudinal (fiber) failure,  $d_2$  is the damage variable associated with transverse matrix cracking, and  $d_6$  is the damage variable

associated with longitudinal and transverse cracks.  $\beta_{11}$  and  $\beta_{22}$  are the coefficients of hygroscopic expansion in the longitudinal and transverse directions, respectively.  $\Delta T$  and  $\Delta M$  are the differences of temperature and moisture content with respect to the corresponding reference values. The coefficients of thermal expansion of a ply are also affected by the failure mechanisms. The exact dependence of the coefficients of thermal expansion with damage can be obtained for simple laminates in the absence of stress gradients [41]. These conditions are not met by the laminate under investigation here and the effects of damage on the coefficients of thermal expansion are neglected.

The strain tensor is equal to the derivative of the complementary free energy density with respect to the stress tensor

$$\varepsilon = \frac{\partial G}{\partial \sigma} = \mathbf{H} : \sigma + \alpha \Delta T + \beta \Delta M \quad (14)$$

The lamina compliance tensor can be represented as

$$\mathbf{H} = \frac{\partial^2 G}{\partial \sigma^2} = \begin{bmatrix} \frac{1}{(1-d_1)E_1} & -\frac{\nu_{12}}{E_1} & 0 \\ -\frac{\nu_{12}}{E_1} & \frac{1}{(1-d_2)E_2} & 0 \\ 0 & 0 & \frac{1}{(1-d_6)G_{12}} \end{bmatrix} \quad (15)$$

The closure of transverse cracks under load reversal is taken into account by defining four damage variables associated with longitudinal and transverse damage. To distinguish between the active and the passive damage variables, it is necessary to define the longitudinal and transverse damage modes as follows:

$$d_1 = d_{1+} \frac{\langle \sigma_{11} \rangle}{|\sigma_{11}|} + d_{1-} \frac{\langle -\sigma_{11} \rangle}{|\sigma_{11}|} \quad (16)$$

$$d_2 = d_{2+} \frac{\langle \sigma_{22} \rangle}{|\sigma_{22}|} + d_{2-} \frac{\langle -\sigma_{22} \rangle}{|\sigma_{22}|}$$

where  $\langle x \rangle$  is the McCauley operator defined as  $\langle x \rangle := (x + |x|)/2$ .

### 3.3.2. Damage activation functions

The determination of the domain of elastic response under complex stress states is an essential component of an accurate damage model. It is assumed that the elastic domain is enclosed by four surfaces, each of them accounting for one damage mechanism: longitudinal and transverse fracture under tension and compression. Those surfaces are formulated by the damage activation functions based on the LaRC04 failure criteria [26].

The four damage activation functions,  $F_N$ , associated with damage in the longitudinal ( $N=1+, 1-$ ) and transverse ( $N=2+, 2-$ ) directions represented in Fig. 6, are defined as

$$F_{1+} = \phi_{1+} - r_{1+} \leq 0; \quad F_{1-} = \phi_{1-} - r_{1-} \leq 0 \quad (17)$$

$$F_{2+} = \phi_{2+} - r_{2+} \leq 0; \quad F_{2-} = \phi_{2-} - r_{2-} \leq 0$$

where the loading functions  $\phi_N$  ( $N=1+, 1-, 2+, 2-$ ) depend on the strain tensor and material constants (elastic and strength properties). The elastic domain thresholds  $r_N$  ( $N=1+, 1-, 2+, 2-$ ) take an initial value of 1 when the material is undamaged, and they increase with damage. The elastic domain thresholds are related to the damage variables  $d_M$  ( $M=1+, 1-, 2+, 2-, 6$ ) by the damage evolution laws.

The current values of the elastic domain thresholds  $r_N$  are obtained using the loading functions  $\phi_N$  according to the following equations [19,39,40]:

$$r_{1+} = \max \left\{ 1, \max_{s=0,t} \{ \phi_{1+}^s \}, \max_{s=0,t} \{ \phi_{1-}^s \} \right\}$$

$$r_{1-} = \max \left\{ 1, \max_{s=0,t} \{ \phi_{1-}^s \} \right\} \quad (18)$$

$$r_{2+} = \max \left\{ 1, \max_{s=0,t} \{ \phi_{2+}^s \}, \max_{s=0,t} \{ \phi_{2-}^s \} \right\}$$

$$r_{2-} = \max \left\{ 1, \max_{s=0,t} \{ \phi_{2-}^s \} \right\}$$

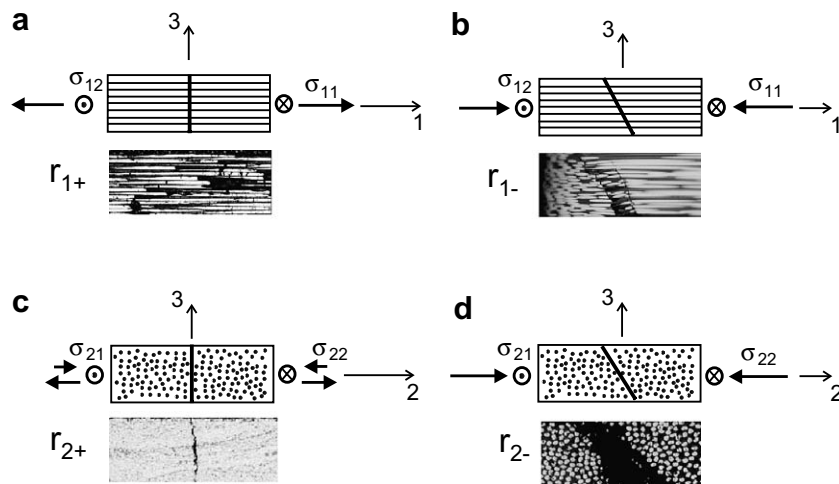


Fig. 6. Fracture surfaces and corresponding internal variables. (a) Longitudinal tensile fracture, (b) longitudinal compressive fracture, (c) transverse fracture with  $\alpha = 0^\circ$  and (d) transverse fracture with  $\alpha = 53^\circ$ .

**3.3.2.1. Longitudinal tensile fracture.** The LaRC04 criterion for fiber tension is defined as

$$\phi_{1+} = \frac{E_1}{X_T} \varepsilon_{11} = \frac{\tilde{\sigma}_{11} - \nu_{12} \tilde{\sigma}_{22}}{X_T} \quad (19)$$

where the effective stress tensor  $\tilde{\sigma}$  is computed as  $\tilde{\sigma} = \mathbf{H}_0^{-1} : \varepsilon$ .  $\mathbf{H}_0$  is the undamaged compliance tensor.

**3.3.2.2. Longitudinal compressive fracture.** The damage activation function used to predict damage under longitudinal compression ( $\tilde{\sigma}_{11} < 0$ ) and in-plane shear (fiber kinking) is established as a function of the components of the stress tensor  $\tilde{\sigma}^{(m)}$  in a coordinate system ( $m$ ) representing the fiber misalignment

$$\phi_{1-} = \frac{\langle |\tilde{\sigma}_{12}^m| + \eta^L \tilde{\sigma}_{22}^m \rangle}{S_L} \quad (20)$$

where the coefficient of longitudinal influence can be approximated as [26]

$$\eta^L \approx -\frac{S_L \cos(2\alpha_0)}{Y_C \cos^2 \alpha_0} \quad (21)$$

with  $\alpha_0 = 53^\circ$  [27]. The components of the effective stress tensor in the coordinate system associated with the rotation of the fibers are calculated as

$$\begin{aligned} \tilde{\sigma}_{22}^m &= \tilde{\sigma}_{11} \sin^2 \varphi^C + \tilde{\sigma}_{22} \cos^2 \varphi^C - 2|\tilde{\sigma}_{12}| \sin \varphi^C \cos \varphi^C \\ \tilde{\sigma}_{12}^m &= (\tilde{\sigma}_{22} - \tilde{\sigma}_{11}) \sin \varphi^C \cos \varphi^C + |\tilde{\sigma}_{12}|(\cos^2 \varphi^C - \sin^2 \varphi^C) \end{aligned} \quad (22)$$

The misalignment angle ( $\varphi^C$ ) is determined using standard shear and longitudinal compression strengths,  $S_L$  and  $X_C$ , respectively [26]

$$\varphi^C = \arctan \left( \frac{1 - \sqrt{1 - 4 \left( \frac{S_L}{X_C} + \eta^L \right) \frac{S_L}{X_C}}}{2 \left( \frac{S_L}{X_C} + \eta^L \right)} \right) \quad (23)$$

**3.3.2.3. Transverse fracture perpendicular to the mid-plane of the ply.** Transverse matrix cracks perpendicular to the mid-plane of the ply, i.e. with  $\alpha_0 = 0^\circ$ , are created by a combination of in-plane shear stresses and transverse tensile stresses, or in-plane shear stresses and small transverse compressive stresses. These conditions are represented by the following failure criteria:

$$\phi_{2+} = \begin{cases} \sqrt{(1-g) \frac{\tilde{\sigma}_{22}}{Y_T} + g \left( \frac{\tilde{\sigma}_{22}}{Y_T} \right)^2 + \left( \frac{\tilde{\sigma}_{12}}{S_L} \right)^2} & \text{if } \tilde{\sigma}_{22} \geq 0 \\ \frac{1}{S_L} \langle |\tilde{\sigma}_{12}| + \eta^L \tilde{\sigma}_{22} \rangle & \text{if } \tilde{\sigma}_{22} < 0 \end{cases} \quad (24)$$

where  $g$  is the fracture toughness ratio defined as  $g = \frac{G_{2+}}{G_6}$ .

**3.3.2.4. Transverse compressive fracture.** The matrix failure criterion for transverse compressive stresses consists of a quadratic interaction between the effective shear stresses acting on the fracture plane

$$\phi_{2-} = \sqrt{\left( \frac{\tilde{\tau}_{\text{eff}}^T}{S_T} \right)^2 + \left( \frac{\tilde{\tau}_{\text{eff}}^L}{S_L} \right)^2} \quad \text{if } \tilde{\sigma}_{22} < 0 \quad (25)$$

where the effective stresses  $\tilde{\tau}_{\text{eff}}^T$  and  $\tilde{\tau}_{\text{eff}}^L$  are computed as [26]

$$\begin{aligned} \tilde{\tau}_{\text{eff}}^T &= \langle -\tilde{\sigma}_{22} \cos(\alpha_0) (\sin(\alpha_0) - \eta^T \cos(\alpha_0) \cos(\theta_s)) \rangle \\ \tilde{\tau}_{\text{eff}}^L &= \langle \cos(\alpha_0) (|\tilde{\sigma}_{12}| + \eta^L \tilde{\sigma}_{22} \cos(\alpha_0) \sin(\theta_s)) \rangle \end{aligned} \quad (26)$$

with  $\eta^T = \frac{-1}{\tan(2\alpha_0)}$  and  $\theta_s = \arctan \left( \frac{-|\tilde{\sigma}_{12}|}{\tilde{\sigma}_{22} \sin(\alpha_0)} \right)$ .

### 3.3.3. Damage evolution laws and numerical implementation

Strain-softening constitutive models that do not take into account the finite element discretization produce results that are mesh-dependent, i.e. the solution is non-objective with respect to the mesh refinement and the computed energy dissipated decreases with a reduction of the element size [42,43]. An effective solution to assure objective solutions consists of using a characteristic length of the finite elements ( $l^*$ ) in the definition of the constitutive model [42]. As schematically shown in Fig. 7, the post-peak response of the material is scaled as a function of the element size to keep the computed energy dissipation independent of the size of the element, and equal to the material fracture energy.

The energetic regularization of the model proposed requires the fracture energies associated with the four fracture planes shown in Fig. 6. These fracture energies were measured in the experimental program and are used in the damage evolution laws.

The exponential damage evolution laws proposed by the authors [19,39,44] are expressed in the following general form:

$$d_M = 1 - \frac{1}{f_N(r_N)} \exp \{A_M [1 - f_N(r_N)]\} f(r_K) \quad (27)$$

where the function  $f_N(r_N)$  is selected to force the softening of the constitutive relation and it is taken as being independent of the material. The term  $f(r_K)$  represents the coupling factor between damage laws and elastic threshold domains. The specific damage evolution laws for each damage variable are presented in [19,39–44].

The regularization of the energy dissipated is performed by integrating the rate of energy dissipation for each failure

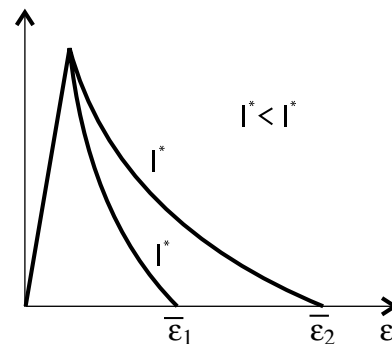


Fig. 7. Scaling of constitutive model for different element sizes.

mode. The energy dissipated in each failure mode must be independent of the element size, and must be equal to the fracture energy measured in the experiments

$$\int_1^\infty \frac{\partial G}{\partial d_M} \frac{\partial d_M}{\partial r_M} dr_M = \frac{G_M}{l^*}, \quad M = 1+, 1-, 2+, 2-, 6 \quad (28)$$

Using (27) in (28), it is possible to numerically integrate the resulting equation and calculate the parameters  $A_M$  that assure a mesh-independent solution [19].

The constitutive model was implemented in the ABAQUS Finite Element (FE) code [45] as a user-written UMAT subroutine.

### 3.3.4. Mesh objectivity and unidirectional notched specimen

The mesh objectivity of the model proposed is illustrated by simulating the response of a notched  $[90]_{24}$  CFRP laminate loaded in tension. The specimen simulated is 150 mm long, 12 mm wide, 3 mm thick, and contains a central circular notch with a diameter of 6 mm. The properties used are reported in Tables 1–3.

Two FE models with different mesh refinements and using the damage model outlined in the previous sections were created. Models 1 and 2 use, respectively, 6 and 20 elements along the fracture plane. Only one-half of the specimen width is modeled. The details of the two meshes are shown in Fig. 8.

Fig. 9 shows the load–displacement relation predicted using the constitutive model proposed. It is observed that the solution is independent of the mesh refinement.

In order to demonstrate the error introduced by not accounting for element size, two analyses with different levels of mesh refinement were also conducted with a constitutive model that is not adjusted using Eq. (28). Instead, a constant softening parameter  $A_{2+} = 1.5$  is used, independently of the mesh refinement. The load–displacement relation predicted by this model is shown in Fig. 10. It is clear from this figure that the maximum load and energy dissipation predicted are a function of the refinement of the mesh.

### 3.3.5. Quasi-isotropic open hole tension specimens

Finite element models of all OHT specimens shown in the test matrix presented in Section 2 were created using

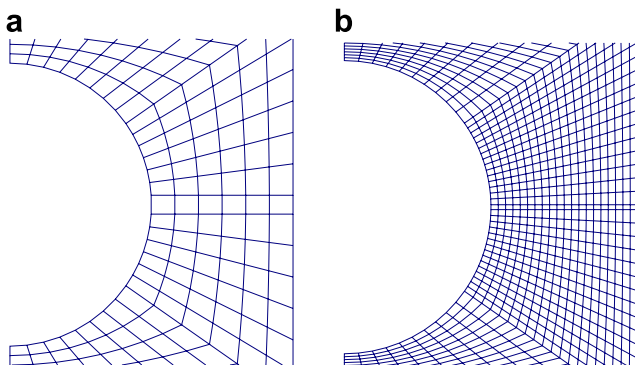


Fig. 8. Different mesh refinements: (a) mesh 1; (b) mesh 2.

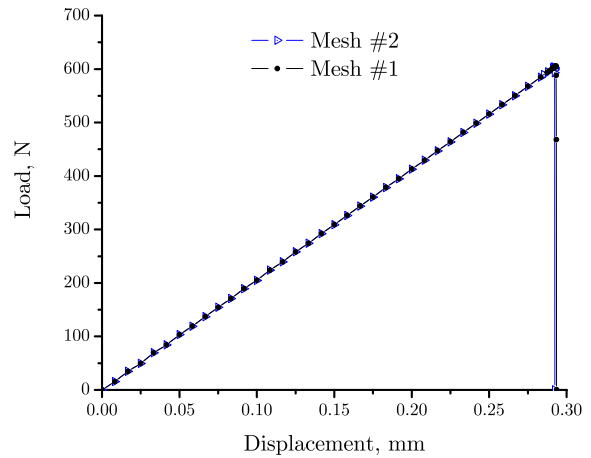


Fig. 9. Load–displacement relation predicted using the model proposed.

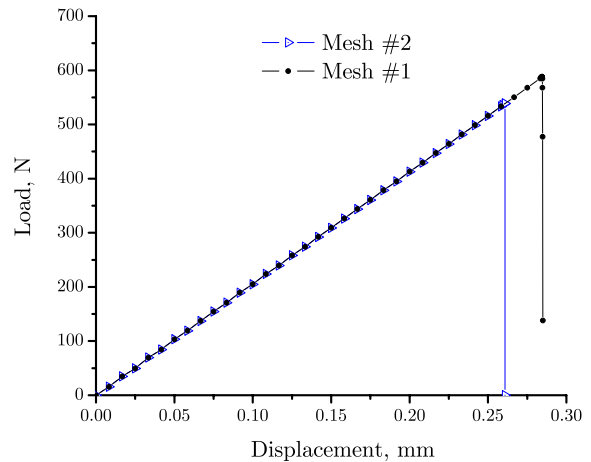


Fig. 10. Load–displacement relation predicted using the non-adjusted model.

ABAQUS [45] four-node S4 shell elements. The difference between the working and reference temperatures used to calculate the residual thermal stresses was  $-155^\circ\text{C}$ . An implicit dynamic analysis was subsequently performed, and the loading rate used in the experiments, 2 mm/min, was also applied to the numerical models. The use of an implicit dynamic finite element model enables the prediction of the load drop that occurs when the specimens fail catastrophically. The material properties used are presented in Tables 1–5.

Delamination is not simulated by the model. As explained by Green et al. [4], delamination is the driving failure mechanism for ply-blocked laminates, but not for sublaminates-level scaled laminates, such as those used in this work. The simulation of delamination is required for ply-blocked laminates, and can be performed using cohesive elements connecting several shell elements that represent the layers [46].

The models simulate the fracture process from the onset of damage up to structural collapse. Fig. 11 shows the evolution of fiber fracture predicted in the top  $0^\circ$  ply, as well



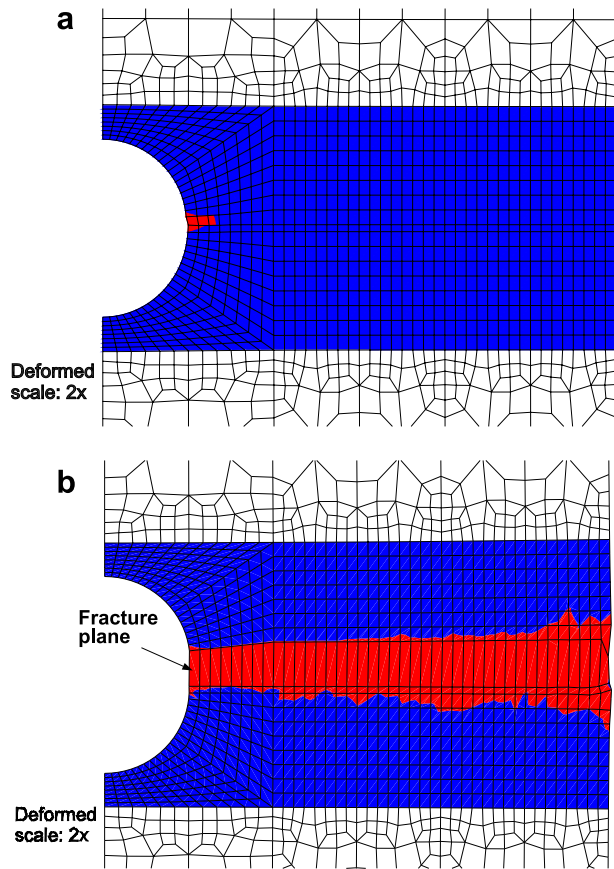


Fig. 11. Evolution of fiber fracture in the top 0° ply for the specimen OHT9.

the plane of localized deformation (fracture plane) for specimen configuration OHT9.

Fig. 12 shows the relation between the applied remote stress and the longitudinal deformation measured using the strain gages and the corresponding numerical predictions in the specimen OHT6. The numerical results corre-

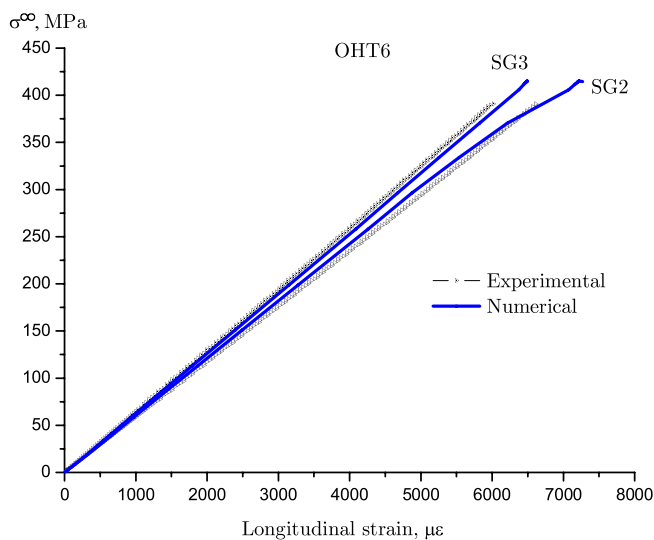


Fig. 12. Experimental and numerical results- specimen OHT6, strain gages SG2 and SG3.

Table 8

Comparison between experimental and numerical failure stresses (MPa)

Hole diameter (mm)	$\bar{\sigma}^\infty$ , experimental	$\bar{\sigma}^\infty$ , numerical	Error (%)
2	555.7	553.6	−0.4
4	480.6	463.0	−3.7
6	438.7	430.0	−2.0
8	375.7	415.0	+10.5
10	373.7	405.6	+8.5

spond to the averaged strain calculated in the group of elements whose position and total area correspond approximately to the area where the strain gages were bonded to the specimen. The location of the different strain gages is shown in Fig. 1.

The remote failure stresses measured in the experimental program and predicted by the numerical model are shown in Table 8.

From the comparison between the experimental and numerical results, both in terms of stress–strain relations and failure stresses, it can be concluded that the model is capable of predicting with good accuracy the response of all OHT specimens that were tested.

### 3.4. Comparison of approaches

The four methods previously described, i.e. strength of materials, LEFM-scaled, LEFM-inherent flaw model, point stress model, and continuum damage model were applied to predict the size effect for the specimens described in Section 2.2.

Eq. (7) provides the LEFM-scaled prediction for the notched strength of the laminate when all the in-plane dimensions are scaled. The average failure stress measured in the specimens with a hole diameter of 6 mm was used in the LEFM model to predict the strength of the specimens with different geometries.

Eq. (11) provides the LEFM-inherent flaw model prediction of the notched strength. The specimen with a 6 mm hole diameter is used to calculate the length of the inherent flaw. Using the measured mean failure stress in Eq. (11), the length of the inherent flaw is calculated as  $a = 1.28$  mm.

The point-stress prediction of the size effect is performed using Eq. (12). The characteristic distance of 0.75 mm was obtained by using the measured mean failure stress in the specimen with a 6 mm hole diameter. This value of the characteristic distance is used to predict the strength of the other specimens.

The predictions of the normalized strength as a function of the hole diameter obtained using the different models are shown in Fig. 13.

It can be observed that both the point stress and LEFM-IFM models can predict with reasonable accuracy the size effect law of notched composite laminates. The point stress and inherent flaw models are particularly accurate for specimens with hole diameters close to the diameter used to calculate the characteristic distance (PSM) and the length of

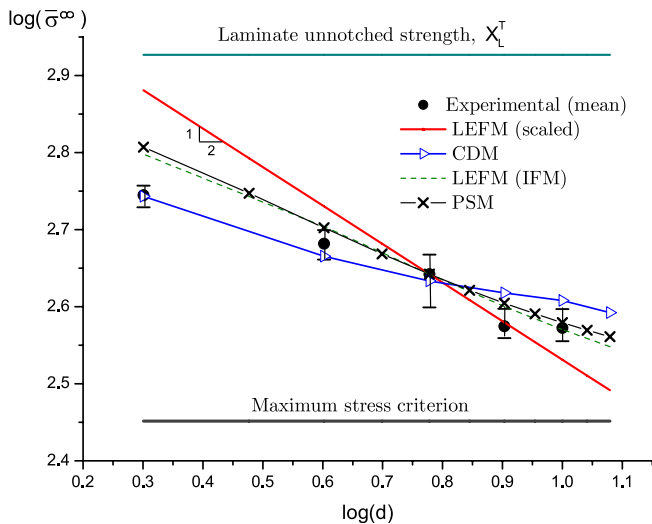


Fig. 13. Predictions of size effects in CFRP plates with  $w/d = 6$ .

the inherent flaw. For specimens with small hole diameters, the predictions lose accuracy. Therefore, to accurately predict the notched strength of laminates these models require the calculation of the characteristic distance and length of inherent flaw for different geometries, and the definition of an extrapolation procedure to define the values of these parameters for other geometries [18]. It should also be noted that the basic equation used in the inherent flaw model, Eq. (11), is only valid when finite width effects are negligible, which is the case of the specimens tested. For smaller ratios between the specimen width and hole diameter, the inherent flaw model should be modified.

The continuum damage model can predict the size effect law observed in the experiments, especially for specimens with hole diameters smaller than 6 mm. Unlike the point stress and inherent flaw models, the continuum damage model does not require any adjustment parameter and only uses material properties that are measured at the ply level as well as the fracture energies.

Fig. 13 indicates that the use of the LEFM-scaled model results in accurate predictions for hole sizes between 6 mm and 10 mm. However, the strength is overpredicted for small hole diameters. For small specimens, the damaged region in the vicinity of the hole cannot be considered to be negligible when compared with the characteristic dimensions of the specimen, and LEFM is not applicable.

LEFM-scaled predictions are also inaccurate for large specimens because the notched strengths of those specimens tend to a constant value [4]. Bazant [15] relates this asymptotic structural response to the invariance of the size of the fracture process zone when the characteristic dimensions of large specimens are increased. It should also be noted that the LEFM predictions based on scaled specimens always result in a line with a  $-1/2$  slope that passes through the baseline point (Fig. 13). This means that the use of a small hole diameter as the baseline point would result in severe underpredictions of the notched strength of larger specimens.

The maximum stress criterion for longitudinal failure is unable to predict size effects and always underpredicts the strength of notched laminates. For a hole diameter of 2 mm, the application of the maximum stress criterion results in an error of  $-49.1\%$ . The error associated with the strength of materials approach is even larger when using a failure criterion for transverse (matrix) cracking, which occurs before fiber fracture, or failure criteria that are unable to distinguish fiber and matrix failure modes.

#### 4. Conclusions

The size effect in notched IM7-8552 CFRP was identified and quantified in an experimental program. The acoustic emission results show that final fracture is preceded by a process of accumulation of non-critical damage mechanisms.

By comparing the experimental data with the different models that are commonly used for the strength prediction of composites, it can be concluded that fiber-based failure criteria (strength of materials approach) cannot predict size effects. In addition, the strength of materials approach always underpredicts the strength of notched composites, with errors as high as  $-49.1\%$  for a specimen with a 2 mm hole diameter.

The Linear Elastic Fracture Mechanics approach using a hole diameter of 6 mm for calibration predicts the size effect accurately for specimens with hole diameters between 6 mm and 10 mm. However, Linear Elastic Fracture Mechanics should not be used for the strength prediction of specimens with hole diameters equal to or less than 2 mm, or for larger specimens whose failure stresses tend to a constant value.

The point stress and inherent flaw models are simple approaches that do not require complex FE implementations yet provide reasonable predictions for the range of hole diameters tested. However, the accuracy of these models relies upon the measurement of the characteristic distance and length of the inherent flaw for each lay-up and stacking sequence.

For the problems selected, the continuum damage model proposed predicts with good accuracy hole size effects in composite laminates subjected to tension. The model requires material properties that are measured at the ply level and fracture energies that are measured using both standard test methods and novel compact tension and compact compression test methods. The continuum damage models provides not only the final failure load, but also information concerning the integrity of the material during the load history. Furthermore, the finite element-based damage model can be applied to structures and components of arbitrary configurations where analytical solutions could not be developed.

#### Acknowledgements

The financial support of the Portuguese Foundation for Science and Technology (FCT) under the project PDCTE/

50354/EME/2003 is acknowledged by the first author. Effort sponsored by the Air Force Office of Scientific Research, Air Force Material Command, USAF, under grant number FA8655-06-1-3072. The US Government is authorized to reproduce and distribute reprints for Governmental purposes notwithstanding any copyright notation thereon.

## References

- [1] MIL-HDBK-17. Military handbook, Polymer matrix composites. US Department of Defense; 1994.
- [2] Going to extremes: meeting the emerging demand for durable polymer matrix composites. Washington (DC): National Research Council, The National Academies Press; 2006.
- [3] Hinton MJ, Soden PD. Predicting failure in composite laminates: the background to the exercise. *Compos Sci Technol* 1998;58:1001–10.
- [4] Green BG, Wisnom MR, Hallet SR. An experimental investigation into the tensile strength scaling of notched composites. *Composites – Part A* 2007;38:867–78.
- [5] Bazant ZP, Daniel IM, Li Z. Size effect and fracture characteristics of composite laminates. *J Eng Mater Technol* 1996;118:317–23.
- [6] Wisnom MR. Size effects in the testing of fibre-reinforced composites. *Compos Sci Technol* 1999;59:1937–57.
- [7] Dvorak GJ, Suvorov AP. Size effect in fracture of unidirectional composite plates. *Int J Fract* 1999;95:89–101.
- [8] Bazant ZP, Zhou Y, Novák D, Daniel IM. Size effect on flexural strength of fiber-composite laminates. *J Eng Mater Technol* 2004;126:29–37.
- [9] Bazant ZP. Size effect. *Int J Solids Struct* 2000;37:69–80.
- [10] Parvizi A, Garrett K, Bailey J. Constrained cracking in glass fibre-reinforced epoxy cross-ply laminates. *J Mater Sci* 1978;13:195–201.
- [11] Dvorak GJ, Laws N. Analysis of first ply failure in composite laminates. *Eng Fract Mech* 1986;25:763–70.
- [12] Camanho PP, Dávila CG, Pinho ST, Iannucci L, Robinson P. Prediction of in situ strengths and matrix cracking in composites under transverse tension and in-plane shear. *Composites – Part A* 2006;37:165–76.
- [13] Waddoups ME, Eisenmann JR, Kaminski BE. Macroscopic fracture mechanics of advanced composite materials. *J Compos Mater* 1971;5:446–54.
- [14] Mollenhauer D, Iarve EV, Kim R, Langley B. Examination of ply cracking in composite laminates with open holes: a Moiré interferometric and numerical study. *Composites – Part A* 2006;37:282–94.
- [15] Bazant ZP, Chen EP. Scaling of structural failure. Report SAND96-2948. Albuquerque. New Mexico: Sandia National Laboratories; 1996.
- [16] Whitney JM, Nuismer RJ. Stress fracture criteria for laminated composites containing stress concentrations. *J Compos Mater* 1974;8:253–65.
- [17] Chang FK, Scott RA, Springer GS. Strength of mechanically fastened composite joints. *J Compos Mater* 1982;16:470–94.
- [18] Camanho PP, Lambert M. A design methodology for mechanically fastened joints in laminated composite materials. *Compos Sci Technol* 2006;66:3004–20.
- [19] Maimí P, Camanho PP, Mayugo JA, Dávila CG. A thermodynamically consistent damage model for advanced composites. NASA Technical Memorandum 214282, National Aeronautics and Space Administration; 2006.
- [20] Standard test method for tensile properties of polymer matrix composite materials, ASTM D 3039/D 3039M-00. West Conshohocken (PA), USA: American Society for Testing and Materials (ASTM).
- [21] Standard test method for compressive properties of unidirectional or cross-ply fiber-resin composites, ASTM D 3410-87. West Conshohocken (PA), USA: American Society for Testing and Materials (ASTM).
- [22] Standard test method for in-plane shear response of polymer matrix composite materials by test of a  $\pm 45^\circ$  laminate, ASTM D 3518/3518M-94. West Conshohocken (PA), USA: American Society for Testing and Materials (ASTM).
- [23] Standard test methods for mode I interlaminar fracture toughness of unidirectional fiber-reinforced polymer matrix composites, ASTM D 5528-01. West Conshohocken (PA), USA: American Society for Testing and Materials (ASTM).
- [24] Martin R, Elms T, Bowron S. Characterization of mode II delamination using the 4ENF. In: Proceedings of the 4th European conference on composites: testing and standardisation, Lisbon, 1998.
- [25] Dávila CG, Camanho PP, Rose CA. Failure criteria for FRP laminates. *J Compos Mater* 2005;39:323–45.
- [26] Pinho ST, Dávila CG, Camanho PP, Iannucci L, Robinson P. Failure models and criteria for FRP under in-plane or three-dimensional stress states including shear non-linearity, NASA Technical Memorandum 213530. USA: National Aeronautics and Space Administration; 2005.
- [27] Puck A, Schürmann H. Failure analysis of FRP laminates by means of physically based phenomenological models. *Compos Sci Technol* 1998;58:1045–67.
- [28] Pinho ST. Modelling failure of laminated composites using physically-based failure models, PhD thesis. Department of Aeronautics, Imperial College London, UK, 2005.
- [29] Pinho ST, Robinson P, Iannucci L. Fracture toughness of the tensile and compressive fibre failure modes in laminated composites. *Compos Sci Technol* 2006;66:2069–79.
- [30] Sawicki AJ, Minguet PJ. The influence of fastener clearance upon the failure of compression-loaded composite bolted joints. Composite structures: theory and practice, ASTM STP 1383. American Society for Testing and Materials; 2000. p. 293–308.
- [31] Open hole tensile strength of polymer composite laminates, ASTM D 5766/D 5766M-02a. West Conshohocken (PA), USA: American Society for Testing and Materials (ASTM).
- [32] Turon A, Camanho PP, Costa J, Dávila CG. A damage model for the simulation of delamination in advanced composites under variable-mode loading. *Mech Mater* 2006;38:1072–89.
- [33] Irwin GR. Plastic zone near a crack and fracture toughness. In: Proceedings of the seventh segamore ordnance materials conference, New York, 1960. p. 63–78.
- [34] Turon A, Dávila CG, Camanho PP, Costa J. An engineering solution for using coarse meshes in the simulation of delamination with cohesive zone models, NASA Technical Memorandum 213547. USA: National Aeronautics and Space Administration; 2005.
- [35] Tan SC. Stress concentrations in laminated composites. Technomic Publishing Company, Inc.; 2004.
- [36] Herakovich CT. Mechanics of fibrous composites. John Wiley and Sons, Inc.; 1998.
- [37] Bowie OL. Analysis of an infinite plate containing radial cracks, originating at the boundaries of an internal circular hole. *J Math Phys* 1956;35:60–71.
- [38] Tada H, Paris P, Irwin GR. The stress analysis of cracks handbook. New York: The American Society of Mechanical Engineers; 2000.
- [39] Maimí P, Camanho PP, Mayugo JA, Dávila CG. A continuum damage model for composite laminates: part I – constitutive model. *Mech Mater*, in press.
- [40] Maimí P, Camanho PP, Mayugo JA, Dávila CG. A continuum damage model for composite laminates: part II – computational implementation and validation. *Mech Mater*, in press.
- [41] Joffe R, Krasnikovs A, Varna J. COD-based simulation of transverse cracking and stiffness reduction in (S/90n)s laminates. *Compos Sci Technol* 2001;61:637–56.
- [42] Bazant ZP, Oh BH. Crack band theory for fracture of concrete. *Matér Construc* 1983;16(93):155–77.
- [43] Bazant ZP, Jirásek M. Nonlocal integral formulations of plasticity and damage: survey of progress. *J Eng Mech* 2002;128:1119–49.

- [44] Maimí P. Modelización constitutiva y computacional del daño y la fractura de materiales compuestos, PhD thesis, Universitat de Girona, Spain, 2006.
- [45] ABAQUS 6.5 User's manual. ABAQUS Inc., Pawtucket, RI, USA, 2005.
- [46] Dávila CG, Turon A, Camanho PP. Decohesion elements for shell analysis. In: Camanho PP, Wisnom MR, Pierron F, editors. Proceedings of the composites testing and model identification conference, Porto, Portugal, 10–12 April 2006.



## Appendix C: Paper published in ECCM-13

# Simulation of Progressive Damage in Bolted Composite Joints

Hannes Koerber, Pedro P. Camanho

DEMEGI, Faculdade de Engenharia, Universidade do Porto  
Rua Dr. Roberto Frias, 4200-465 Porto, Portugal  
hkoerber@fe.up.pt

## Abstract

In this article, finite element analyses of mechanically fastened double-lap joints in carbon/epoxy laminates are performed using a progressive damage model available in the commercial software ABAQUS. An alternative damage model, implemented into a VUMAT user subroutine, is also presented. Two failure modes are considered: catastrophic net-section tension-failure and non-catastrophic accumulation of bearing damage. A three-dimensional mesh is used for the analysis and in addition to results for static implicit analysis; a method for explicit simulation of quasi-static tests is presented. The simulation results are compared with experimental data. By comparison of the two damage models for the tension-failure simulation, it can be shown that the shape of the damage evolution law for fiber-tension damage is perhaps more critical than the fracture energy value. Results for simulation of bearing damage using the commercial damage model are presented and some limitations of the model are discussed.

## 1 Introduction

With the increasing use of fiber-reinforced plastics (FRPs) in aerospace structures, the analysis of mechanically fastened joints in composite materials has become a key aspect in the design process. It is well known that mechanically fastened joints perform better in metals than they do in composite structures. The joint efficiency in a metal structure is 70% - 80% compared to 40% - 50% in a composite [1]. Some reasons for the relatively low performance of bolted composite joints are: the brittleness of the composite material, which allows little stress relief around the loaded hole; material anisotropy, leading to high stress concentrations; and low through-thickness strength of classic unidirectional laminates, causing interlaminar delamination. Despite these disadvantages, mechanically fastened composite joints are widely used, since they provide a fast and efficient way of substructure assembly. Due to the complex failure mechanisms, their design however relies heavily on experiments combined with semi-analytical methods [2]. If it is possible to obtain part of the mechanical properties needed during the design phase via numerical analysis, significant cost savings can be achieved. Analysis using progressive damage models, able to capture the physics of the failure mechanisms occurring at damage initiation and damage evolution leading to ultimate failure has therefore received significant attention in recent years.

In general, two-dimensional finite element modelling is sufficient for the majority of linear composite laminate analysis. While this is computationally efficient and preferable for most applications, a three-dimensional model may be suited better for the analysis of a bolted composite joint in a quasi-isotropic laminate. In a 3D-model, cohesive zone elements can be included to capture delamination failure; unsymmetrical loading of the bolt hole (single-lap joints) can be considered and through-thickness stresses (clamping forces) which are known to have a significant effect on the initiation of bearing damage may be considered [3].

## 2 Progressive Damage Models for Unidirectional FRP Laminates

Two progressive damage models for FRP unidirectional laminates are applied in the present work. The first model recently became available in the commercial finite element code ABAQUS/Standard 6.6.1 and ABAQUS/Explicit 6.7.1, and will therefore be referred to as the Abaqus-Model. The Hashin-criteria is used for damage initiation in this model [4],[5]. The influence of damage on the constitutive material model is based on the work of Matzenmiller et al. [6] and damage evolution for all failure modes is governed by a simple linear formulation, used by Camanho and Davila for cohesive elements [7]. A detailed description of the Abaqus-Model, including its numerical implementation, is presented in [8]. An alternative damage model, based on the work of Maimi et al. [9] is also used in this study. The model can be used for finite element analysis in Abaqus/Explicit via a VUMAT user subroutine and will therefore be referred to as the VUMAT-Model. Maimi applies a combination of the LaRC03 and LaRC04 criteria for damage initiation [10],[11]. Rather than using linear softening, exponential damage evolution laws are applied to describe the softening response for all failure modes except fiber tension. For unidirectional carbon/epoxy laminates, such as the material used in this study, the propagation of a crack perpendicular to the fiber-direction under tensile loading can be divided into two phases. An initial and rather brittle fiber-matrix failure mechanism, followed by a tougher fiber-bridging and fiber pull-out phase acting at a lower stress level [12]. To account for the different damage mechanisms, a linear-exponential law is therefore used for the fiber-tension mode (Figure 1, b). For both models, the area under the stress-strain curve is equal to the dissipated fracture energy divided by a characteristic length of the finite element. References [8] and [9] provide further information on the determination of the characteristic element length. In case of the VUMAT-Model, the fracture toughness determined for fiber-tensile fracture (Table 2) is divided in two parts, associated with the linear and exponential softening law. In addition to the tensile strength  $X^T$ , a value representing the fiber pull-out strength  $X^{PO}$  must be specified for the VUMAT-model.

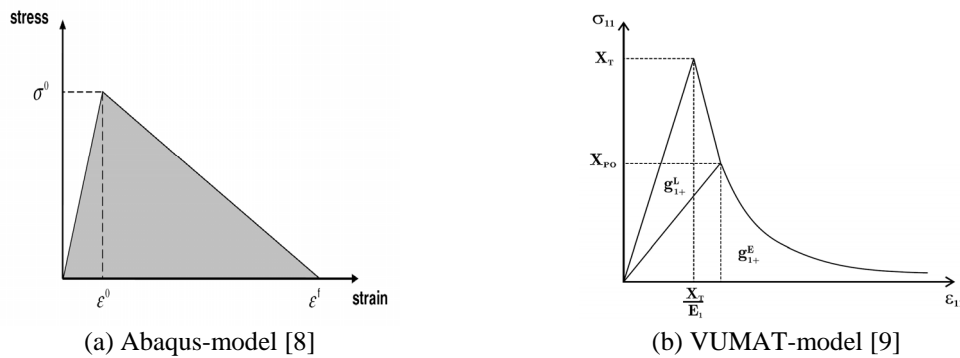


Figure 1. Damage evolution laws for fiber-tension

## 3 Experiments

Two double-shear bolted joint specimens tested in the context of developing a design methodology for mechanically fastened composite joints [2] were selected in this study. The specimen geometry and dimensions are shown in Figure 2 and were designed to either promote pure tensile- or bearing-failure. Both specimens were made of UD carbon/epoxy prepreg Hexcel IM7-8552 with a quasi-isotropic lay-up of

[90/0/+45/-45]<sub>4s</sub>. A 6 mm steel bolt was used and a washer with an outer-diameter of 12 mm was placed on either side of the laminate. The torque applied to the bolt corresponds to a finger-tight assembly. Surface strain was measured according to the strain gauge positions specified in Figure 2. Both specimens were tested in a conventional load frame at a quasi-static displacement-rate of 2 mm/min.

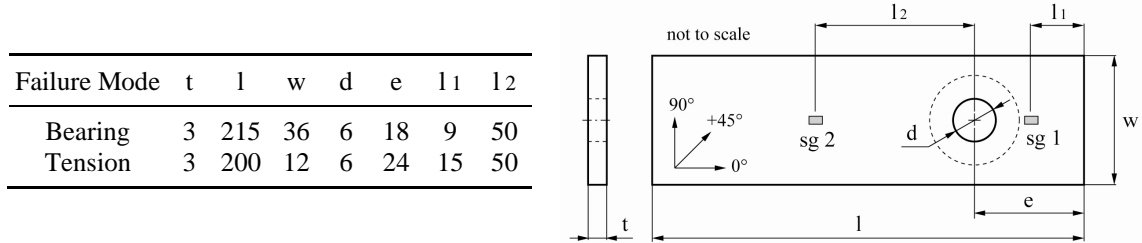


Figure 2. Specimen geometry (dimensions in mm)

#### 4 FE Model

The finite element model used for both specimen types will be explained on the basis of the tension failure specimen shown in Figure 3. For the bearing failure specimen a similar mesh was used. Due to the lay-up symmetry, only half of the laminate was modelled and symmetry boundary conditions were applied at the laminate symmetry plane. One element per ply was used for the laminate mesh, which was divided into a coarse mesh area away from the hole and a refined mesh area around the hole and in the direction of loading. Both mesh regions are connected via a TIE constraint which is a convenient way for mesh transition as opposed to a paved mesh or multi-point constraint (MPC). In case of the bolt, only the length of the shaft in contact with the hole was modelled. Similar symmetry boundary conditions were applied to the nodes lying in the laminate symmetry plane. The washer is accounted for by a distributed load corresponding to the bolt torque and applied to a surface approximately equal to the surface area of the washer. Strain in the loading direction is obtained from two element sets in the first layer of elements, representing the 90° outer-ply, at the strain gauge position of the test specimen (Figure 2). Although not applied in the present simulations, the 3D finite element mesh was developed for the use of cohesive zone delamination elements and a full 3D-formulation of the VUMAT damage model, which is yet to be implemented into an Abaqus subroutine. For the Abaqus-Model, where two formulations of the Hashin-criteria are available, the formulation proposed by Hashin and Rotem was selected [4]. The in-situ effect was considered for both damage models. It is characterised by higher transverse tensile and shear strengths for a ply constrained by plies with different fiber orientations, compared to the strengths of the same ply in a unidirectional laminate [13]. For the tension-failure specimen, simulations were conducted using the implicit and explicit Abaqus-model as well as the VUMAT-model. The bearing failure specimen was simulated using the implicit and explicit Abaqus-model. Depending on the damage model and solver, different elements were used for the different regions of the finite element model. The selected elements are summarised in Table 1 where SC8R stands for a reduced integration continuum shell element, similar to a standard solid but with a kinematic and a constitutive behaviour similar to a conventional shell. The Abaqus-Model is limited to elements with plane-stress formulation, therefore only the SC8R element can be used in a 3D-mesh. C3D8 and C3D8R represent standard solid elements in a fully integrated or reduced integration

formulation, respectively. For reduced integration elements, default hourglass control parameters were selected. In case of the implicit Abaqus-model, viscous regularisation (VR) had to be used to obtain a converging solution. The VR-parameters were selected according to a similar example given in [8].

Table 1. Finite element selection

Type	Solver	Version	Damage Model	Laminate Fine	Mesh Area Laminate Coarse	Bolt
Abaqus/Standard		6.6.1	Abaqus	SC8R	C3D8	C3D8
Abaqus/Explicit		6.7.1	Abaqus	SC8R	C3D8R	C3D8R
Abaqus/Explicit		6.6.1	VUMAT	C3D8R	C3D8R	C3D8R

The joint is loaded via a velocity boundary condition applied to a selected node-set of the bolt mesh. In case of the implicit Abaqus-model, this velocity corresponds to the actual test speed. To obtain a simulation time suited for an explicit simulation, two modifications were applied to the explicit model. The test speed was increased by a factor of 1000 and the mass density was scaled by a factor of 100, resulting in a 10-fold increase of the stable time increment.

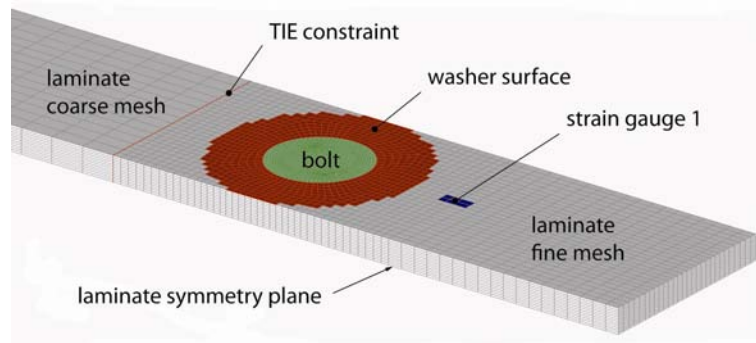


Figure 3. Finite element model of tension failure specimen

To evaluate if the modified FE-model produces an appropriate quasi-static response, the energy balance was studied [14]:

$$E_I + E_V + E_{FD} + E_{KE} - E_W = E_{TOTAL} = const. \quad (4.1)$$

$E_I$  is the internal energy,  $E_V$  is the energy absorbed by viscous dissipation,  $E_{FD}$  is the energy absorbed by frictional dissipation,  $E_{KE}$  is the kinetic energy,  $E_W$  is the work of external forces and  $E_{TOTAL}$  is the total energy in the system. For a quasi-static analysis,  $E_W$  should be approximately equal to  $E_I$ , while as  $E_V$ ,  $E_{FD}$ ,  $E_{KE}$  and  $E_{TOTAL}$  should be near zero. According to [14] however, a 5% to 10% value of the kinetic energy compared to the internal energy is acceptable. A graphical representation of the energy-balance is illustrated in Figure 4. With the exception of a slight increase in the total energy  $E_{TOTAL}$ , the above conditions for a quasi-static analysis hold for the entire duration of the simulation. The total energy increase prior to ultimate failure is caused by an increase of  $E_V$  and  $E_A$ . These two energies are introduced to stabilise the

element during damage evolution. As they remain small compared to  $E_I$  and  $E_W$ , it was concluded that the modifications to the explicit model are valid and the simulation is in fact representing a quasi-static test.

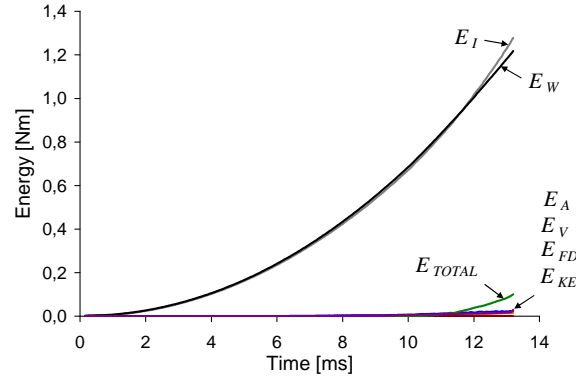


Figure 4. Energy balance, tension-failure simulation (VUMAT-model)

The material properties used for both progressive damage models are summarised in Table 2. Elastic and unidirectional ply strengths can be obtained from standard test methods and the in-situ ply strengths can be calculated according to [13]. For the fracture energies, a test standard exists only for matrix tension [15]. The values for tensile and compressive fiber fracture, can be obtained from compact tension (CT) and compact compression (CC) tests as proposed by Pinho et al. [16]. Matrix compression fracture energy can be obtained from mode II end-notched flexure tests (ENF) and a formulation for  $G_{2-}$  specified in [9]. According to this formulation, the value depends on the laminate stacking configuration. In the present study the value for a strongly confined laminate is used. The additional parameters used for the VUMAT-model are associated with the different damage evolution law (compare Figure 1, b) and since the LaRC damage initiation criteria considers the fracture angle for compressive transverse load cases, a representative fracture angle  $\alpha$  must also be given.

Table 2. IM7-8552 material properties

(a) Elastic ply properties			(b) UD ply strength			(c) In-situ ply strength [MPa]		
$E_1$	171.42	GPa	$X^T$	2226.2	MPa	Ply configuration	$Y_{is}^T$	$S_{is}^L$
$E_2 = E_3$	9.08	GPa	$X^C$	1200.1	MPa	thin outer	101.4	107.0
$G_{12} = G_{13}$	5.29	GPa	$Y_{ud}^T$	62.3	MPa	thin embedded	160.2	130.2
$G_{23}$	3.98	GPa	$Y^C$	199.8	MPa	thin embedded (2t)	113.3	107.0
$\nu_{12} = \nu_{13}$	0.32	-	$S_{ud}^L$	92.3	MPa			
$\nu_{23}$	0.5	-						
(d) Fracture energies [kJ/m <sup>2</sup> ]			(e) Additional VUMAT-model properties					
fiber tension	$G_{1+}$	81.5	fiber pull-out strength	$X_{PO}$	232.3	MPa		
fiber compression	$G_{1-}$	106.5	fracture angle	$\alpha$	53	°		
matrix tension	$G_{2+}$	0.2774	$G_{1+}$ , linear softening	$G_{1+}^L$	31.5	kJ/m <sup>2</sup>		
matrix compression	$G_{2-}$	5.62	$G_{1+}$ , exponential softening	$G_{1+}^E$	50.0	kJ/m <sup>2</sup>		

## 5 Simulation Results

### 5.1 Tension-failure simulation

The maximum load,  $P_{\max}$ , obtained from the simulations and experiment, is summarised in Table 3 and Figure 5 shows the load-strain response at strain gauge position 1 and 2. It can be seen that both simulations using the Abaqus-model significantly overestimate the ultimate load while as the results of the VUMAT-model correlate well with the mean average load maximum obtained from the experiment. Another difference between the simulation results can be noticed when plotting the fiber damage parameter for a  $0^\circ$ -ply (Figure 6). For both Abaqus-model simulations, the crack propagates at an angle of about  $45^\circ$  to the fiber-direction and hence follows the matrix damage developing in the neighbouring  $45^\circ$ -ply. The crack in the VUMAT-model localises in a plane perpendicular to the fibers, as observed in the experiment.

It should be noted that various damping mechanisms, such as mass- or stiffness-proportional Rayleigh-damping and bulk viscosity, exist for the Abaqus-model while as these mechanisms did not have a major effect on the user material specified in the VUMAT subroutine. Therefore oscillations measured at strain gauge 1 could not be avoided in this case.

Table 3. Maximum load, tension failure specimen

		$P_{\max}$ [kN]	
Experiment	(mean average)	9.477	
	(minimum)	9.232	(-2.6%)
	(maximum)	10.135	(+6.9%)
Abaqus Model, implicit		12.833	(+35.4%)
Abaqus Model, explicit		13.122	(+38.5%)
VUMAT Model		9.454	(-0.2%)

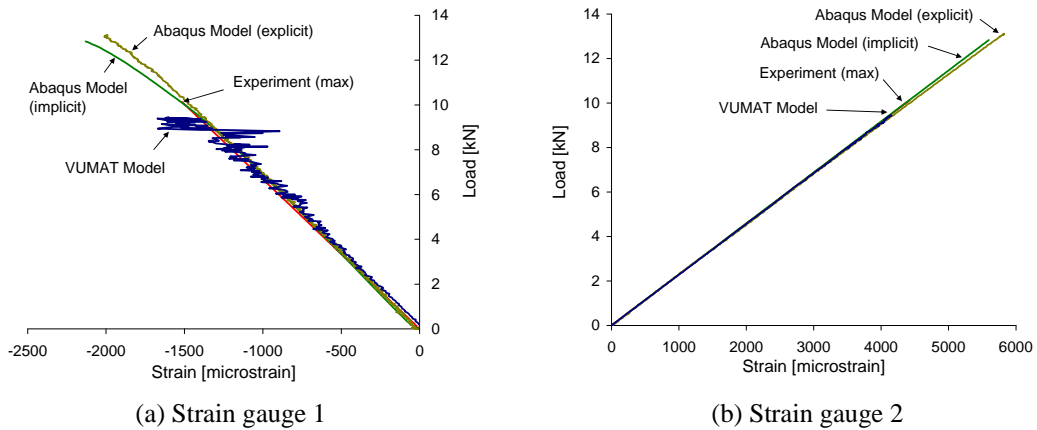


Figure 5. Load-strain response, tension-failure specimen

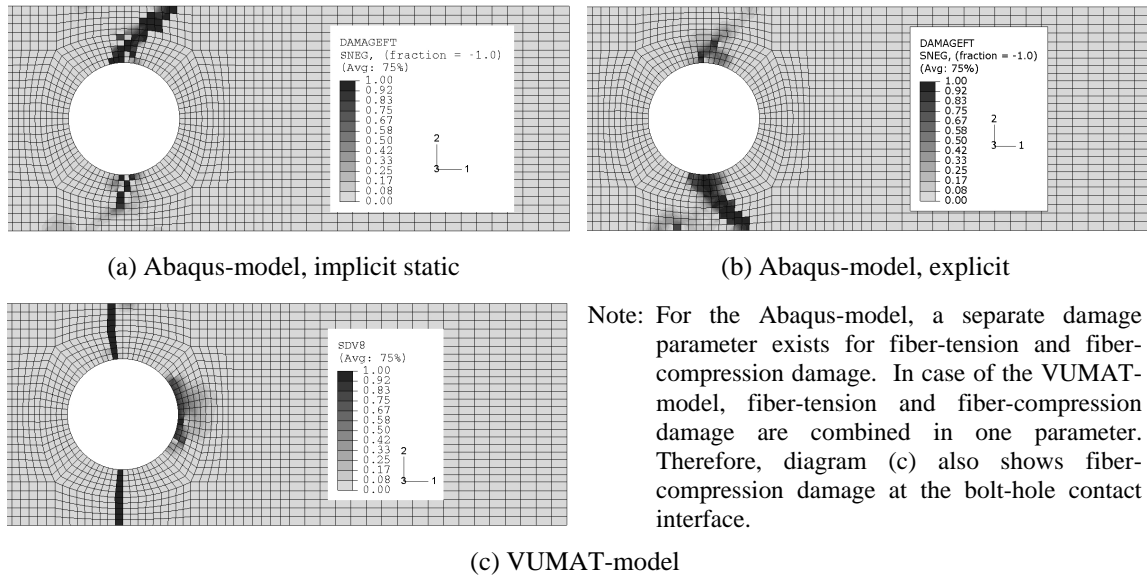


Figure 6. Fiber damage in layer 2 ( $0^\circ$ ) at maximum load, tension failure specimen

## 5.2 Bearing-failure simulation

Other than in the case of the tension-failure specimen, where ultimate failure is clearly defined by the maximum load, bearing-failure is a non-catastrophic damage mode, characterised by a progressive accumulation of damage and permanent hole deformation [2]. As a result, different definitions may be used for defining bearing strength such as the onset of nonlinearity or the bearing strength at 2% bearing strain offset. Figure 7 (a) shows the load-strain response obtained from simulation and a representative experiment at strain gauge position 1. Diagram (b) illustrates the bearing stress-bearing strain curve as defined by the ASTM test method [17]. The difference between the initial bearing stress slope of simulation and experiment can be explained by the different method of obtaining the hole elongation. In case of the simulation, the elongation was measured directly on the hole, while as for the test a LVDT was attached to the test rig and laminate, similar to the illustration in Fig. 10 (a) of [17].

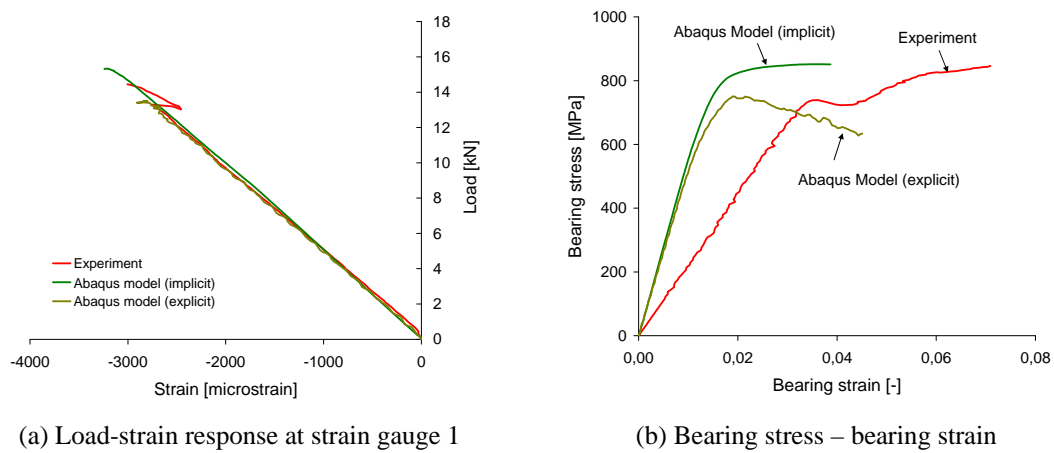


Figure 7. Load-strain and bearing stress-bearing strain response



Table 4 summarises the bearing strengths defined at the onset of nonlinearity  $\sigma_{onl}^{br}$  and at 2% bearing strain offset  $\sigma_{2\%off}^{br}$  for the implicit and explicit Abaqus-model simulation and the experiment. It is clear from the experimental results that the 2% offset definition is associated with significant data scatter which complicates a comparison between simulation and experiment. It was shown by Camanho and Lambert that damage at 2% strain offset has progressed to a state of through-the-thickness cracks spanning several plies [2]. This damage state can not be captured by the present finite element model and therefore the onset of nonlinearity (at 5% decrease of the initial chord modulus), is used for a comparison of simulation and experiment rather than the 2% offset definition. For both simulations, the predicted bearing strength is below the experimental value. Figure 8 shows the extent of predicted fiber-compression damage at 2% offset bearing strength.

Table 4. Bearing strength

		$\sigma_{onl}^{br}$ [MPa]		$\sigma_{2\%off}^{br}$ [MPa]	
Experiment	(mean average)	747		870	
	(minimum)	738	(-1.2%)	747	(-14.1%)
	(maximum)	753	(+0.8%)	958	(+10.1%)
Abaqus-model, implicit		645	(-13.6%)	851	(-2.2%)
Abaqus-model, explicit		610	(-18.3%)	689	(-20.8%)

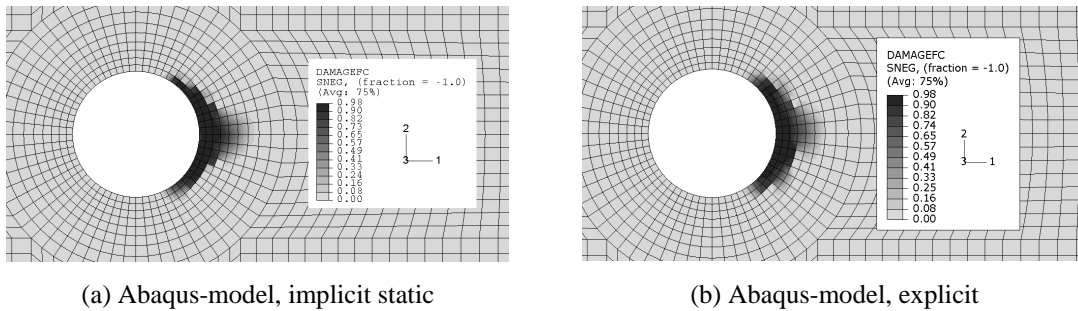


Figure 8. Fiber damage in layer 2 (0°) at 2% offset bearing strength, bearing specimen

## 6 Discussion and Conclusion

### 6.1 Tension-failure simulation

In Section 5.1 it was shown that the ultimate load for the tension-failure specimen was significantly over-predicted by the Abaqus-model (Table 3). Since the same material properties were used for all simulations and viscous regularisation was not specified for the explicit analysis, it is assumed that the difference between the Abaqus- and VUMAT-model is associated with the damage evolution law. It was further noticed that the crack for the Abaqus-model develops in a plane inclined at an angle of 45° to the fibers. In an attempt to create a damage evolution shape similar to that used in the VUMAT-model, the fracture energy for fiber-tension (compare Table 2, d) was reduced by 50%. With this modification, the over-prediction was reduced to 7.8% for the implicit and to 18.5% for the explicit formulation of the Abaqus-model. Comparing Figure 6 and Figure 8, it can be seen that the crack has shifted towards a plane

perpendicular to the fiber-direction with the improvement most pronounced for the implicit model. It is therefore concluded that the shape of the fiber-tension damage evolution law is more critical than the actual fracture toughness value and that the formulation chosen in the VUMAT-model is able to represent the damage mechanisms occurring in the fiber-tension damage mode.

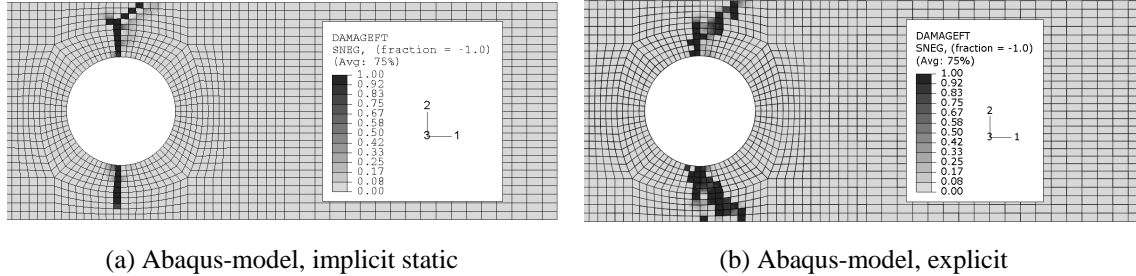


Figure 9. Fiber-damage in layer 2 ( $0^\circ$ ) at maximum load for Abaqus-model with modified fracture toughness

## 6.2 Bearing-failure simulation

In Section 5.2 it was shown that conservative results can be obtained for the bearing strength at onset of nonlinearity (ONL), using either the implicit or explicit formulation of the Abaqus-model (Table 4). With damage initiation occurring at a similar stress level of about 450-460 MPa, the bearing strength results for the ONL-formulation of bearing strength were relatively close. The difference in the nonlinear region of the bearing stress curve, comparing the implicit and explicit solution in Figure 7 is not entirely understood yet and may partly be attributed to the influence of viscous regularisation on the evolution of damage. As for the tension-failure specimen, viscous regularisation had to be used for the implicit static simulation in order to obtain a converging solution but was not used in case of the explicit simulations. Further, it is possible that the masses considered in the explicit simulation, and hence the modifications as described in Section 4, may have an influence on the fiber-compression damage mode; although this did not seem to be critical for the tension-failure simulation.

It is concluded that the Abaqus-model, using a simple maximum strength criteria and linear damage evolution law for fiber-compression, is able to predict a lower bound for ONL bearing strength. In reality however, the damage mechanism for fiber-compression is more complicated with fiber-kinking occurring in the  $0^\circ$  plies. Further, the model can not account for the stabilising-effect of through-thickness stresses [3], which is not critical if a relatively low level of clamping pressure is used, but may lead to a significant under-prediction at higher torque-levels.

## Acknowledgements

The financial support by the Air Force Office of Scientific Research, Air Force Material Command, USAF, under grant number FA8655-06-1-3072 is acknowledged. The U.S. Government is authorised to reproduce and distribute reprints for Governmental purpose notwithstanding any copyright notation thereon.

## References

- [1] McCarthy M.A., "BOJCAS: Bolted Joints in Composite Aircraft Structures", *Air and Space Europe*, 2001; 3
- [2] Camanho P.P., Lambert M., "A design methodology for mechanically fastened joints in laminated composite materials", *Composites Science and Technology*, 2006; 66: 3004-3020
- [3] Park H.J., "Effects of stacking sequence and clamping force on the bearing strength of mechanically fastened joints in composite laminates", *Composite Structures*, 2001; 53: 213-221
- [4] Hashin Z., Rotem A., "A fatigue failure criterion for fiber reinforced materials", *Journal of Composite Materials*, 1973; 7: 448-464
- [5] Hashin Z., "Failure criteria for unidirectional fiber composites", *Journal of Applied Mechanics*, 1980; 47: 329-334
- [6] Matzenmiller A., Lubliner J., Taylor R.L., "A constitutive model for anisotropic damage in fiber-composites", *Mechanics of Materials*, 1995; 20: 125-152
- [7] Camanho P.P., Davila C.G., "Mixed-mode decohesion finite elements for the simulation of delamination in composite materials", *NASA-TM-2002-211737*, 2002
- [8] Lapczyk I., Hurtado J.A., "Progressive damage modelling in fiber-reinforced materials", *Composites Part A*, 2007; 38: 2333-2341
- [9] Maimi P., Camanho P.P., Mayugo J.A., Davila C.G., "A continuum damage model for composite laminates: Part II – Computational implementation and validation", *Mechanics of Materials*, 2007; 39: 909-919
- [10] Davila C.G., Camanho P.P., Rose C.A., "Failure criteria for FRP laminates", *Journal of Composites Materials*, 2005; 29: 323-345
- [11] Pinho S.T., Davila C.G., Iannucci L., Robinson P., "Failure models and criteria for FRP under in-plane or three-dimensional stress states including shear non-linearity", *NASA-TM-2005-213530*, 2005
- [12] Davila C.G., Rose C.A., "Superposition of cohesive elements to account for R-curve toughening in the fracture of composites", *Abaqus Users' Conference*, 2008
- [13] Camanho P.P., Davila C.G., Pinho S.T., Iannucci L., Robinson P., "Prediction of in situ strengths and matrix cracking in composites under transverse tension and in-plane shear", *Composites Part A*, 2006; 37: 165-176
- [14] ABAQUS 6.6 "Getting started with ABAQUS", Abaqus Inc., 2006
- [15] "Standard test method for mode I interlaminar fracture toughness of unidirectional fiber-reinforced polymer matrix composites" ASTM D 5528-01, American Society for Testing and Materials (ASTM), West Conshohocken, PA, USA
- [16] Pinho S.T., Robinson P., Iannucci L., "Fracture toughness of the tensile and compressive fibre failure modes in laminated composites", *Composites Science and Technology*, 2006; 66: 2069-2079
- [17] "Standard test method for bearing response of polymer matrix composite laminates" ASTM D 5961/D 5961 M-05, American Society for Testing and Materials (ASTM), West Conshohocken, PA, USA

## Appendix D: Paper published in the Journal of Composite Materials

# A three-dimensional damage model for transversely isotropic composite laminates

P. Maimí<sup>a</sup>, P.P. Camanho<sup>b,\*</sup>, J.A. Mayugo<sup>a</sup>

<sup>a</sup>AMADE, Universitat de Girona, Campus Montilivi s/n, Girona, Spain

<sup>b</sup>DEMEGI, Faculdade de Engenharia, Universidade do Porto, Rua Dr. Roberto Frias, 4200-465, Porto, Portugal

---

## Abstract

This paper proposes a fully three-dimensional continuum damage model, developed at the sub-ply level, to predict in an integrated way both the intralaminar and the interlaminar failure mechanisms that occur in laminated fiber-reinforced polymer composites. The constitutive model is based on the assumption that the composite material is transversely isotropic, and accounts for the effects of crack closure under load reversal cycles. The damage model is implemented in an implicit finite element code taking into account the requirement to ensure a mesh-independent computation of the dissipated energy. The comparison between the model predictions and published experimental data indicates that the model can accurately predict the effects of transverse matrix cracks on the residual stiffness of quasi-isotropic laminates, the interaction between transverse matrix cracks and delamination, and final failure of the laminate.

*Key words:* Fracture, Damage Mechanics, FEA.

---

[Table 1 about here.]

## 1 Introduction

It has been widely recognized that one of the most significant barriers to the increased use of composite materials is the inability to predict accurately structural failure [1]. The prediction of structural failure in laminate composites is particularly challenging when both delamination and intraply failure mechanisms, such as matrix cracking or fiber failure, contribute to the fracture process.

Delamination is normally simulated using methods based on Linear-Elastic Fracture Mechanics, such as the Virtual Crack Closure Technique [2], or using cohesive formulations [3]-[9]. The onset of intralaminar failure mechanisms is normally predicted using ply-based failure criteria

---

\* Corresponding author

Email address: [pcamanho@fe.up.pt](mailto:pcamanho@fe.up.pt) (P.P. Camanho).

[10]-[15]. Generally, failure criteria alone are unable to predict the collapse of composite structures. To predict failure initiation, propagation and final collapse it is necessary to combine the ply-based failure criteria with appropriate damage models. When the laminate is uniformly stressed, and when transverse matrix cracks are the main failure mechanism, it is possible to use analytical or semi-analytical solutions to relate the applied load to the residual stiffness and strength of the laminate [16]-[21]. However, the simulation of the propagation of intralaminar failure mechanisms in composite structures with complex geometries requires models based on the formalism of continuum damage mechanics [22]-[30].

There are several relevant structural applications of laminated composites where both delamination and ply failure mechanisms are relevant, interacting, energy dissipation mechanisms. For example, in composites subjected to low velocity impact, in skin-stiffener terminations or in ply-scaled notched laminates. The approach normally used to simulate both delamination and ply failure is to combine cohesive elements that simulate delamination with continuum damage models that simulate ply damage [31]-[33]. Although this mesomechanical approach has proved to be successful for some structural configurations [31], there are some fundamental problems that prevent the general application of this methodology that uses two different kinematic representations for interlaminar and intralaminar failure mechanisms. For example, in the numerical simulation of the interaction between transverse matrix cracks and delamination it is necessary to capture the high stresses at the tip of the transverse crack. Using a mesomechanical model, it is not possible to capture this interaction because the elements where the transverse crack is predicted soften without being able to accurately capture the stress field at the interface. Furthermore, even if strain-softening constitutive models are used in mesomechanical models to predict transverse matrix cracking in multidirectional laminates, the finite element where transverse cracking is predicted does not unload the adjoining elements that represent the same ply, and therefore is unable to represent a transverse crack.

To accurately predict the interaction between intralaminar and interlaminar failure mechanisms it is essential to have a good kinematic representation of the different failure mechanisms. This has been realized by Wisnom and co-workers [34],[35] in their simulations of fracture of notched and unnotched specimens, using cohesive zone models to represent both intralaminar and interlaminar failure mechanisms. The cohesive zone models provide an accurate kinematic representation that enabled the successful simulation of complex phenomena such as size effects in both ply-scaled and sublaminate scaled composite notched specimens [34], and the fracture of unnotched scaled quasi-isotropic specimens [35]. Although the use of cohesive zone models has proved to be an accurate technology to simulate the interaction between failure mechanisms there are two main limitations to its use. The first limitation is the need to know in advance the planes of crack propagation. There are several situations where the orientation of the crack plane is not known *a priori*. For example, when a ply is subjected to both transverse compression and in-plane shear the fracture plane depends on the relation between these two components of the stress tensor [12]. The second limitation to the use of cohesive zone models is the need to introduce cohesive finite elements at every single interface where a crack may develop.

To overcome some of the difficulties in the simulation of the interaction between failure mechanisms, the objective of this work is to formulate a fully three-dimensional damage model at the sub-ply level that is able to represent both interlaminar and intralaminar failure mechanisms without previous knowledge of the orientation of the failure planes. The sub-ply level constitutive model and the corresponding computational implementation are described in the following sections. The model is then validated by comparing the numerical predictions with published

57 experimental results.

## 58 2 Damage model for a transversely isotropic laminate

### 59 2.1 Constitutive tensor

60 Consider a transversely isotropic material and a vector  $\mathbf{e}_1 = \{1, 0, 0\}^T$ , parallel to the fiber  
 61 direction. In the transversely isotropic plane, orthogonal to  $\mathbf{e}_1$ , there is a set of orthonormal  
 62 vectors  $\{\mathbf{e}_2, \mathbf{e}_3\}$  that define a plane where the shear strain  $\gamma_{23}$  is zero. In order to correctly detect  
 63 crack closure under load reversal cycles a set of orthonormal vectors  $\{\mathbf{e}_1, \mathbf{e}_2, \mathbf{e}_3\}$  are defined.

64 Taking  $\epsilon = \{\epsilon_{11}, \epsilon_{22}, \epsilon_{33}, 2\epsilon_{12}, 2\epsilon_{13}, 2\epsilon_{23}\}^T$  as the components of the strain tensor in the global  
 65 coordinate system, the relation between the strain tensor in the local and global coordinate  
 66 system is:

$$\begin{Bmatrix} \varepsilon \\ 0 \end{Bmatrix} = \mathbf{T}\epsilon \quad (1)$$

67 The transformation matrix  $\mathbf{T}$  relates the strains in the material coordinate system to the strains  
 68 in the coordinates defined by the vectors  $\{\mathbf{e}_1, \mathbf{e}_2, \mathbf{e}_3\}$ ,  $\varepsilon = \{\varepsilon_{11}, \varepsilon_{22}, \varepsilon_{33}, \gamma_{12}, \gamma_{13}\}^T$ . Without loss  
 69 of generality, it is possible to assume that the one direction of the global coordinate system  
 70 coincides with  $\mathbf{e}_1$ . Therefore the transformation matrix can be written as:

$$\mathbf{T} = \begin{bmatrix} 1 & 0 & 0 & 0 & 0 & 0 \\ 0 & \cos^2 \theta & \sin^2 \theta & 0 & 0 & \cos \theta \sin \theta \\ 0 & \sin^2 \theta & \cos^2 \theta & 0 & 0 & -\sin \theta \cos \theta \\ 0 & 0 & 0 & \cos \theta - \sin \theta & 0 & 0 \\ 0 & 0 & 0 & \sin \theta & \cos \theta & 0 \\ 0 & -2 \sin \theta \cos \theta & 2 \sin \theta \cos \theta & 0 & 0 & \cos^2 \theta - \sin^2 \theta \end{bmatrix} \quad (2)$$

71 The angle  $\theta$  is determined by enforcing that the shear strain  $\gamma_{23}$  is zero, i.e.,  $\tan(-2\theta) = \frac{-2\epsilon_{23}}{\epsilon_{22} - \epsilon_{33}}$ .

72 Having defined the coordinate system that is the basis for the derivation of the the constitutive  
 73 model, it is now necessary to propose a suitable form for the specific free energy. Assuming  
 74 a constant density, the total complementary free energy is given as  $\int_V \psi dV$ , where  $\psi$  is the  
 75 complementary free energy per unit volume. The proposed definition for the complementary  
 76 free energy per unit volume is:

$$\begin{aligned}
\psi = & \frac{\sigma_{11}^2}{2(1-d_1)E_1} + \frac{1}{2E_2} \left( \frac{\sigma_{22}^2}{1-d_2} + \frac{\sigma_{33}^2}{1-d_3} \right) - \frac{\nu_{12}}{E_1} (\sigma_{22} + \sigma_{33}) \sigma_{11} - \\
& - \frac{\nu_{23}}{E_2} \sigma_{22} \sigma_{33} + \frac{\sigma_{12}^2 + \sigma_{13}^2}{2(1-d_6)G_{12}} + [\alpha_{11}\sigma_{11} + \alpha_{22}(\sigma_{22} + \sigma_{33})] \Delta T + \\
& + [\beta_{11}\sigma_{11} + \beta_{22}(\sigma_{22} + \sigma_{33})] \Delta M
\end{aligned} \tag{3}$$

77 where  $\alpha_{11}$  and  $\alpha_{22}$  are the coefficients of thermal expansion in the longitudinal and transverse  
 78 direction, respectively.  $\beta_{11}$  and  $\beta_{22}$  the coefficients of hygroscopic expansion in the longitudinal  
 79 and transverse direction, respectively.  $\Delta T$  and  $\Delta M$  are the differences in temperature and  
 80 moisture content with respect to the corresponding reference values.  $d_1$ ,  $d_2$  and  $d_3$  are the  
 81 damage variables. The strain tensor is calculated as:

$$\varepsilon = \frac{\partial \psi}{\partial \sigma} = \mathbf{H} : \sigma + \alpha \Delta T + \beta \Delta M, \text{ with } \mathbf{H} = \frac{\partial^2 \psi}{\partial \sigma \otimes \partial \sigma} \tag{4}$$

82 The compliance tensor,  $\mathbf{H}$ , relates the elastic strains with the elastic stresses. This tensor  
 83 depends on the value of damage variables. It is assumed that damage is represented by a set  
 84 of variables that affect the longitudinal, the transverse and the shear modulus. The damage  
 85 variables related to longitudinal and transverse directions change when the normal stresses  
 86 switch from positive to negative or vice-versa. The damage variable  $d_1$  represents cracks in  
 87 planes normal to the fiber direction, whereas the damage variables  $d_2$  represents cracks in  
 88 planes parallel to the fiber direction. The damage variable  $d_6$  affect the shear moduli  $G_{12}$  and  
 89  $G_{13}$ . The transverse damage variable is not able to detect, at constitutive level, the directionality  
 90 of cracks. However, the directionality of cracks is detected at macroscopic level as the locus of  
 91 the damaged points. From (4), the compliance tensor is defined as:

$$\mathbf{H} = \begin{bmatrix} \frac{1}{(1-d_1)E_1} & -\frac{\nu_{12}}{E_1} & -\frac{\nu_{12}}{E_1} & 0 & 0 \\ -\frac{\nu_{12}}{E_1} & \frac{1}{(1-d_2)E_2} & -\frac{\nu_{23}}{E_2} & 0 & 0 \\ -\frac{\nu_{12}}{E_1} & -\frac{\nu_{23}}{E_2} & \frac{1}{(1-d_3)E_2} & 0 & 0 \\ 0 & 0 & 0 & \frac{1}{(1-d_6)G_{12}} & 0 \\ 0 & 0 & 0 & 0 & \frac{1}{(1-d_6)G_{12}} \end{bmatrix} \tag{5}$$

92 where  $E_1$  and  $E_2$  are the longitudinal and transverse Young modulus, respectively.  $\nu_{12}$  is the  
 93 major Poisson ratio and  $\nu_{23}$  is the Poisson ratio in the transverse isotropic plane.  $G_{12}$  is the  
 94 shear modulus.  $d_1$ ,  $d_2$  and  $d_3$  are the damage variables in the directions defined by the vectors  
 95  $(\mathbf{e}_1, \mathbf{e}_2, \mathbf{e}_3)$ . These damage variables depend on the longitudinal ( $d_{L\pm}$ ) and transverse ( $d_{T\pm}$ )  
 96 damage variables as:



$$\begin{aligned}
d_1 &= d_{L+} \frac{\langle \sigma_{11} \rangle}{|\sigma_{11}|} + d_{L-} \frac{\langle -\sigma_{11} \rangle}{|\sigma_{11}|} \\
d_2 &= d_{T+} \frac{\langle \sigma_{22} \rangle}{|\sigma_{22}|} + d_{T-} \frac{\langle -\sigma_{22} \rangle}{|\sigma_{22}|} \\
d_3 &= d_{T+} \frac{\langle \sigma_{33} \rangle}{|\sigma_{33}|} + d_{T-} \frac{\langle -\sigma_{33} \rangle}{|\sigma_{33}|}
\end{aligned} \tag{6}$$

where  $\langle x \rangle$  is the McCauley operator defined as  $\langle x \rangle := (x + |x|)/2$ . The shear damage variable is not influenced by the sign of the shear stress components, i.e.,  $d_6 = d_S$ . The shear damage variable is influenced by the normal stresses that produce friction between the crack faces allowing stress transfer and dissipation under shear loads [36]. This effect is neglected in the present model.

It should be noted that the closure effect in the transversely isotropic plane is activated independently in the the directions  $\mathbf{e}_2$  and  $\mathbf{e}_3$ . Therefore the material becomes orthotropic when  $\sigma_{22}$  has a different sign than that of  $\sigma_{33}$ .

The coaxially of stresses and strains in the transverse isotropic plane is enforced and the correspondent shear modulus is evaluated as:  $G_{23} = \frac{\sigma_{33} - \sigma_{22}}{2(\varepsilon_{33} - \varepsilon_{22})}$ . If the stresses in the transversely isotropic plane have the same sign, and if the damage variables have the same value ( $d_2 = d_3$ ), the shear modulus is given as:  $G_{23} = \frac{E_2(1-d_2)}{2[1+\nu_{23}(1-d_2)]}$ . It is important to note that, unlike the majority of the rotating crack models, this model does not exhibit a negative shear modulus, which is a physically inadmissible result [37]. This is due to the fact that the damage is isotropic if the transverse stresses have the same sign.

The stress tensor in the global coordinate system ( $\varsigma$ ) is calculated as:

$$\varsigma = \mathbf{T}^T \begin{Bmatrix} \sigma \\ 0 \end{Bmatrix} \tag{7}$$

## 2.2 Dissipation

The thermodynamic forces  $Y_M$  ( $M = 1, 2, 3, 6$ ) are calculated as:

$$\begin{aligned}
Y_1 &= \frac{\partial \psi}{\partial d_1} = \frac{\sigma_{11}^2}{2(1-d_1)^2 E_1} ; & Y_3 &= \frac{\partial \psi}{\partial d_3} = \frac{\sigma_{33}^2}{2(1-d_3)^2 E_2} \\
Y_2 &= \frac{\partial \psi}{\partial d_2} = \frac{\sigma_{22}^2}{2(1-d_2)^2 E_2} ; & Y_6 &= \frac{\partial \psi}{\partial d_6} = \frac{\sigma_{12}^2 + \sigma_{13}^2}{2(1-d_6)^2 G_{12}}
\end{aligned} \tag{8}$$

The rate of dissipation is expressed in terms of the thermodynamic forces and damage variables as:

$$\Xi = Y_1 \dot{d}_1 + Y_2 \dot{d}_2 + Y_3 \dot{d}_3 + Y_6 \dot{d}_6 \geq 0 \quad (9)$$

Due the particular form of the complementary free energy selected, it is observed that the thermodynamic forces ( $Y_M$ ) are always positive. Therefore the condition of positive evolution of damage variables ( $\dot{d}_M \geq 0$ ) ensures a positive energy dissipation. The crack closure effect under load reversal cycles does not result in spurious energy dissipation because the conjugated thermodynamic forces are zero when such a loading scenario takes place [38].

### 2.3 Damage activation functions

The damage activation functions define the elastic domain under general stress states. The elastic domain is defined here by three damage activation functions, that are represented by three surfaces in the strain space.

The selection of the damage activation function depends upon the different failure mechanisms of the material system. The main assumption of the present selection of damage activation functions is that the shear stresses in the transversely isotropic plane,  $\sigma_{12}$  and  $\sigma_{13}$ , create cracks orientated in a plane with a normal vector in the  $(\mathbf{e}_2, \mathbf{e}_3)$  plane. This response is typical of unidirectional composites in which the fibers enforce the matrix cracks to growth along their direction.

The damage activation functions  $F_N$  ( $N = L+, L-, T$ ) are defined as:

$$\begin{aligned} F_{L+} &= \phi_{L+} - r_{L+} \leq 0 \\ F_{L-} &= \phi_{L-} - r_{L-} \leq 0 \\ F_T &= \phi_T - r_T \leq 0 \end{aligned} \quad (10)$$

where  $F_{L+}$  defines the elastic domain for longitudinal tensile failure,  $F_{L-}$  defines the elastic domain for longitudinal compressive failure, and  $F_T$  defines the elastic domain for transverse failure.

The loading functions  $\phi_N$  ( $N = L+, L-, T$ ) depend on the strain tensor, and on the elastic and strength properties. The internal variables  $r_N$  ( $N = L+, L-, T$ ) take an initial value of 1 when the material is undamaged, and they increase with damage. The internal variables of the constitutive model are related to the damage variables  $d_M$  ( $M = L+, L-, T+, T-, S$ ) by the damage evolution laws.

### 2.4 Loading functions

A simple non interacting maximum strain or stress criteria results in accurate predictions of the onset of longitudinal damage of polymer-based composite materials under tensile stresses [14],[15]. The maximum strain criterion is used for longitudinal tensile loading:

$$\phi_{L+} = \frac{E_1}{X_T} \langle \varepsilon_{11} \rangle \quad (11)$$

Longitudinal failure of unidirectional composite materials under compressive stresses is a far more complex phenomenon. The compressive failure is the result of a complex sequence of damage mechanisms that culminate in the formation of a kink band.

The LaRC03-04 [14],[15] failure criteria postulates that fiber kinking is triggered by onset of damage in the matrix. Under this circumstance, the fibers loose their lateral support and collapse under the compressive load. The failure load depends on the initial fibre misalignment, and on the rotation of the fibers as a function of the applied stresses. In this model a simple non-interacting maximum strain is used:

$$\phi_{L-} = \frac{E_1}{X_C} \langle -\varepsilon_{11} \rangle \quad (12)$$

It is clear that such a simple criterion is unable to account for the effects of the shear stresses on fiber kinking. The development of a more accurate failure criterion for three-dimensional stress states will be addressed in future work.

The transverse loading function defines the onset of transverse failure mechanisms. The loading function has to match the three uniaxial loads that produce matrix cracking: transverse tension, transverse compression and longitudinal-transverse shear. The proposed loading function is:

$$\phi_T = \sqrt{\left\langle \frac{Y_C - Y_T}{Y_C Y_T} (\tilde{\sigma}_{22} + \tilde{\sigma}_{33}) + \frac{1}{Y_C Y_T} (\tilde{\sigma}_{22} - \tilde{\sigma}_{33})^2 + \frac{\tilde{\sigma}_{12}^2 + \tilde{\sigma}_{13}^2}{S_L^2} \right\rangle} \quad (13)$$

where  $\tilde{\sigma}$  are the effective stresses, calculated using the undamaged stiffness tensor,  $\mathbf{H}_0^{-1}$  given by (5) with  $d_i = 0$  ( $i = 1, 2, 3, 6$ ), as  $\tilde{\sigma} = \mathbf{H}_0^{-1} : \varepsilon$ . The transverse loading function has the same form as the criteria presented by Christensen [39].

Figure 1 shows the transverse damage activation function. As previously mentioned, the inter-fiber shear stress produce transverse cracks. Therefore, the transverse damage must be activated under uniaxial shear loads. Furthermore, experimental results and failure criteria developed following the Mohr-Coulomb theory, as such as the Puck [12] and the LaRC [14]-[15] criteria, demonstrate that moderate values of transverse compression increase the shear strength. As shown in Figure 1 c), this effect is accounted for in the proposed loading function.

[Fig. 1 about here.]

## 2.5 Internal variables

Neglecting viscous effects, the damage activation functions must be negative. If  $F_N < 0$  the material is in the elastic regime. When the damage activation criteria is satisfied,  $F_N = 0$ , it is necessary calculate the gradient  $\dot{\phi}_N$ . If  $\dot{\phi}_N$  is negative or zero, the state is one of unloading or

173 neutral loading, respectively. The different states of the material response are mathematically  
 174 represented by the Kuhn-Tucker conditions,  $\dot{r}_N \geq 0$ ;  $F_N \leq 0$ ;  $\dot{r}_N F_N = 0$ . If  $\dot{\phi}_N$  is positive,  
 175 damage increases, and the consistency condition has to be satisfied, i.e.,  $F_N = 0 \Rightarrow \dot{F}_N = 0$ .

176 If the internal variables are exclusively dependent on the damage variables, and if the loading  
 177 functions depends on the strain tensor, the constitutive model can be explicitly integrated [40],  
 178 [41]. Applying the consistency condition, the internal variable  $r_T$  is calculated as:

$$r_T = \max \left\{ 1, \max_{s=0,t} \{ \phi_T^s \} \right\} \quad (14)$$

179 The evolution of the longitudinal elastic domain thresholds for tensile or compressive stresses  
 180 are coupled. The elastic domain threshold defines the level of elastic strains that can be attained  
 181 before the accumulation of additional damage.

182 Under longitudinal tensile stresses, the fracture plane is generally perpendicular to the fiber  
 183 direction. When reversing the load, the cracks close and can still transfer load. However, the  
 184 broken and misaligned fibers do not carry any additional load. Therefore, the compressive  
 185 stiffness is influenced by longitudinal damage. However, the elastic domain is assumed to remain  
 186 unchanged. Under longitudinal compression, damaged material consisting of broken fibers and  
 187 matrix cracks forms a kink band, and there is not a unique orientation for the damage planes.  
 188 When the loads are reversed, the cracks generated in compression open and the elastic domain  
 189 threshold increases. To represent these phenomena, the evolution of the longitudinal internal  
 190 variables is defined as:

$$\begin{aligned} \text{Tension loading:} \quad & \dot{r}_{L+} = \dot{\phi}_{L+} \quad \text{and} \quad \dot{r}_{L-} = 0 \\ \text{Compression loading:} \quad & \dot{r}_{L-} = \dot{\phi}_{L-} \quad \text{and} \quad \dot{r}_{L+} = \begin{cases} \dot{\phi}_{L-} & \text{if } r_{L+} \leq r_{L-} \\ 0 & \text{if } r_{L+} > r_{L-} \end{cases} \end{aligned}$$

191 The integration of the previous expressions results in:

$$\begin{aligned} r_{L+} &= \max \left\{ 1, \max_{s=0,t} \{ \phi_{L+}^s \}, \max_{s=0,t} \{ \phi_{L-}^s \} \right\} \\ r_{L-} &= \max \left\{ 1, \max_{s=0,t} \{ \phi_{L-}^s \} \right\} \end{aligned} \quad (15)$$

## 192 2.6 Damage evolution laws

193 The definition of the damage evolution laws, which relate the internal variables with the damage  
 194 variables  $d_M(r_N)$ , is required to fully define the constitutive model.

195 When the material is undamaged, the internal variables  $r_N$  take the initial value of 1, and  
 196  $d_M(r_N = 1) = 0$ . Equations (14) and (15) define the evolution of the internal variables ensuring  
 197 that  $\dot{r}_N \geq 0$ . As shown in equations (8) and (9), the condition for positive dissipation is

198 satisfied if  $\dot{d}_M \geq 0$ . The condition for positive dissipation is automatically fulfilled if the damage  
 199 evolution law satisfies the condition  $\partial d_M / \partial r_N \geq 0$ . When the material is completely damaged,  
 200 a fracture plane is created, the strains are localized in a plane in which  $r_N \rightarrow \infty$  and the related  
 201 components of the stiffness tensor are zero,  $d_M(r_N \rightarrow \infty) = 1$ .

202 The evolution of internal variables can result in material hardening or softening depending the  
 203 damage law. If the stress-strain response result in a softening relation, the deformations localize  
 204 in a plane, and a localization limiter has to be introduced in the model to correctly compute  
 205 the energy dissipated.

206 The procedure followed in this model to ensure a correct computation of the energy dissipated  
 207 is based on the Crack Band Model proposed by Bažant [42]. Using equation (9) it is possible  
 208 calculate the dissipated energy under an uniaxial test as:

$$g_M = \int_0^\infty Y_M \dot{d}_M dt = \int_1^\infty Y_M \frac{\partial d_M}{\partial r_N} dr_N = \frac{G_M}{\ell}; \quad M = L+, L-, T+, S \quad (16)$$

209 where  $\ell$  is the characteristic length of the finite element, and  $G_M$  is the associated fracture  
 210 toughness. The fracture toughness  $G_{L+}$  corresponds to a crack that propagates in a plane  
 211 perpendicular to the fiber direction under mode I loading and the fracture toughness  $G_{L-}$  is  
 212 related to fibre kinking. There are no standard test methods to measure these properties. How-  
 213 ever, Pinho and co-authors [43] developed new compact-tension (CT) and compact-compression  
 214 (CC) test methods that can be used to measure  $G_{L+}$  and  $G_{L-}$ . The fracture toughness  $G_{T+}$   
 215 and  $G_S$  correspond respectively to matrix cracking for mode I and mode II loading. These  
 216 properties can be measured using standard double-cantilever beam and end-notched flexure  
 217 test specimens.

218 If the characteristic element size ( $\ell$ ) is greater than a critical value the material response results  
 219 in snap-back, and the energy dissipation would be overpredicted. To prevent this problem, the  
 220 characteristic element size must be lower than a critical value given by:

$$\ell = \frac{2E_M G_M}{X_M^2}; \quad M = L+, L-, T+, S \quad (17)$$

221 If the element is larger than the maximum size prescribed, and a mesh refinement is unfeasible,  
 222 the snap-back in the constitutive model can be avoided by reducing the corresponding strength  
 223 according to [44]:

$$X_M = \sqrt{\frac{2E_M G_M}{\ell}}; \quad M = L+, L-, T+, S \quad (18)$$

### 224 2.6.1 Transverse tension damage law

225 Under transverse tension, damage localizes in a fracture plane without any previous inelastic  
 226 material behavior. The linear softening, or cohesive, law shown in Figure 2a), is proposed.

227 [Fig. 2 about here.]

For a linear softening law, the stress strain response is given as:  $\sigma_{22} = H_{T+}E_2\varepsilon_{22} + Y$  or  $\sigma_{22} = (1 - d_{T+})E_2\varepsilon_{22}$ . Using the resulting  $\varepsilon_{22}$  in (13) and (14), the damage law is calculated as:

$$d_{T+} = 1 - H_{T+} - \frac{2A_{T+}(1 - H_{T+})Y_T}{-B_{T+} + \sqrt{B_{T+}^2 - 4A_{T+}(C_{T+} - Y_TY_Cr_T^2)}} \quad (19)$$

where  $H_{T+}E_2$  is the incremental stiffness under uniaxial stress, and the remaining parameters are:

$$\begin{aligned} A_{T+} &= \frac{(1 + \nu_{23}H_{T+})^2}{(1 + \nu_{23})^2} \\ B_{T+} &= \frac{(Y_C - Y_T)(1 - H_{T+}(2\nu_{12}\nu_{21} + \nu_{23}))}{1 - \nu_{23} - 2\nu_{12}\nu_{21}} + 2\frac{(1 + \nu_{23}H_{T+})\nu_{23}(1 - H_{T+})Y_T}{(1 + \nu_{23})^2} \\ C_{T+} &= \left(\frac{\nu_{23}(1 - H_{T+})Y_T}{1 + \nu_{23}}\right)^2 - \frac{(Y_C - Y_T)(1 - H_{T+})Y_T(\nu_{23} + 2\nu_{12}\nu_{21})}{1 - \nu_{23} - 2\nu_{12}\nu_{21}} \end{aligned}$$

The parameter  $H_{T+}$  is calculated by applying the crack band model, equation (16):

$$H_{T+} = \frac{Y_T^2\ell}{Y_T^2\ell - 2G_{T+}E_2} \leq 0 \quad (20)$$

### 2.6.2 Transverse compression damage law

The law proposed to simulate damage evolution under transverse compression is shown in Figure 2 a), and it is given as:

$$d_{T-} = 1 - H_{T-} - \frac{2A_{T-}(1 - H_{T-})Y_C}{B_{T-} + \sqrt{B_{T-}^2 - 4A_{T-}(C_{T-} - Y_TY_Cr_T^2)}} \quad (21)$$

where  $H_{T-}E_2$  is the incremental stiffness under an uniaxial compression load.  $H_{T-}$  defines the hardening in the compressive. The parameters  $A_{T-}$ ,  $B_{T-}$  and  $C_{T-}$  are determined following the procedure outlined in the previous section as:

$$\begin{aligned} A_{T-} &= \frac{(1 + \nu_{23}H_{T-})^2}{(1 + \nu_{23})^2} \\ B_{T-} &= \frac{(Y_C - Y_T)(1 - H_{T-}(2\nu_{12}\nu_{21} + \nu_{23}))}{1 - \nu_{23} - 2\nu_{12}\nu_{21}} - 2\frac{(1 + \nu_{23}H_{T-})\nu_{23}(1 - H_{T-})Y_C}{(1 + \nu_{23})^2} \\ C_{T-} &= \left(\frac{\nu_{23}(1 - H_{T-})Y_C}{1 + \nu_{23}}\right)^2 + \frac{(Y_C - Y_T)(1 - H_{T-})Y_C(\nu_{23} + 2\nu_{12}\nu_{21})}{1 - \nu_{23} - 2\nu_{12}\nu_{21}} \end{aligned}$$

### 2.6.3 Longitudinal tension damage law

Crack propagation in the longitudinal direction involves different energy dissipating mechanisms such as fiber fracture, fiber-matrix pull-out and matrix fracture. When different physical mechanisms are involved in crack propagation, a two-part damage evolution law should be used [45]. To accurately represent the propagation of longitudinal failure mechanisms, the authors have previously proposed a softening law defined by the linear-exponential relation shown in Figure 2b) [26], [27]. It is observed in Figure 2b) that the softening response is linear until the stress reaches the pull-out stress,  $X_{PO}$ , and the corresponding energy dissipation per unit area is  $G_{L+}^L$ . These material parameters can be measured using a recently proposed analysis method for the resistance curve measured in the compact tension test specimens [28].

As the strains continue to increase, the softening response follows an exponential law and the energy dissipated per unit area is  $G_{L+}^E$ . The definition of the damage evolution law used here is explained in detail in previous papers [26],[27], and the resulting equations are:

$$\begin{aligned} d_{L+} &= (1 + H_L) \frac{r_{L+} - 1}{r_{L+}} && \text{if } r_{L+} \leq r_{L+}^F \\ d_{L+} &= 1 - \frac{X_{PO}}{X_T r_{L+}} \exp \left[ A_{L+} \frac{r_{L+}^F - r_{L+}}{r_{L+}^F} \right] && \text{if } r_{L+} > r_{L+}^F \end{aligned} \quad (22)$$

where the parameters  $H_L$ ,  $r_{L+}^F$ ,  $d_{1+}^F$  and  $A_{1+}$  are defined in [26],[27].

### 2.6.4 Longitudinal compression damage law

The compressive stiffness is influenced by both the damage produced under compression and under tension. If the material is damaged in tension and the loads are reversed until the material is loaded in compression, the cracks close allowing the stress transfer. Although the cracks are closed, the fibers lose the alignment and do not transfer additional stresses. The stiffness recovery can be approximated with the parameter  $A_L^\pm$ , defined as [26]:

$$A_L^\pm \approx b \frac{V_f E_f}{V_m E_m + V_f E_f} \approx b \frac{E_1 - E_2}{E_1} \quad (23)$$

where  $V_f$  and  $V_m$  are the fiber and matrix volume fraction, respectively.  $E_f$  and  $E_m$  are the fiber and matrix Young modulus, respectively.  $b$  is an adjustment parameter between 0, if the stiffness is completely recovered, and 1, when the stiffness recovery is only due the matrix.

Under longitudinal compressive stresses the damage variable depends of the damage generated under tension and compression as:

$$d_{L-} = 1 - (1 - d_{L-}^*)(1 - A_L^\pm d_{L+}) \quad (24)$$

The damage variable ( $d_{L-}^*$ ) is assumed to be approximated by an exponential law as:

$$d_{L-}^* = 1 - \frac{1}{r_{L-}} \exp [A_{L-} (1 - r_{L-})] \quad (25)$$

### 2.6.5 Shear damage law

The shear stiffness depends on the longitudinal and transverse damage. It is assumed that if material is only damaged longitudinally the shear damage variable takes the same value of that of the longitudinal tensile variable ( $d_S = d_{L+}$ ). If the damage is due the transverse damage, the damage variable ( $d_S^*$ ) is adjusted with the transverse critical fracture energy in mode II. The coupling of both damage variables takes the following form:

$$d_S = 1 - (1 - d_S^*)(1 - d_{L+}) \quad (26)$$

Under a shear test, the material fails in transverse direction. Although the non-localized damage is important in many fiber reinforced plastics, the definition of a constitutive model representing distributed damage and plasticity is outside the scope of this paper and will be addressed in future work. Therefore, an exponential law that enforce softening of the material response is proposed:

$$d_S^* = 1 - \frac{1}{r_T} \exp [A_S (1 - r_T)] \quad (27)$$

Applying the crack band model, the parameter  $A_S$  results in:

$$A_S = \frac{2\ell S_L^2}{2G_{12}G_S - \ell S_L^2} \quad (28)$$

### 2.7 Tangent constitutive tensor and algorithm

The effective computational implementation of the model in an implicit finite element code requires the definition of the tangent stiffness tensor  $\mathbf{C}_T$ :

$$\frac{d\zeta}{dt} = \dot{\zeta} = \mathbf{C}_T \dot{\epsilon} \quad (29)$$

The first step in the definition of the tangent stiffness tensor is the calculation of the time derivative of equation (4):

$$\dot{\sigma} = \tilde{\mathbf{C}} \dot{\epsilon} \quad \text{with} \quad \tilde{\mathbf{C}} = \mathbf{H}^{-1} (\mathbf{I} - \mathbf{M}) \quad (30)$$

where the matrix  $\mathbf{M}$  is defined as:



$$\mathbf{M} = \begin{bmatrix} \frac{\sigma_{11}}{(1-d_1)^2 E_1} \frac{\partial d_1}{\partial \varepsilon_{11}} & \frac{\sigma_{11}}{(1-d_1)^2 E_1} \frac{\partial d_1}{\partial \varepsilon_{22}} & \frac{\sigma_{11}}{(1-d_1)^2 E_1} \frac{\partial d_1}{\partial \varepsilon_{33}} & \frac{\sigma_{11}}{(1-d_1)^2 E_1} \frac{\partial d_1}{\partial \gamma_{12}} & \frac{\sigma_{11}}{(1-d_1)^2 E_1} \frac{\partial d_1}{\partial \gamma_{13}} \\ \frac{\sigma_{22}}{(1-d_2)^2 E_2} \frac{\partial d_2}{\partial \varepsilon_{11}} & \frac{\sigma_{22}}{(1-d_2)^2 E_2} \frac{\partial d_2}{\partial \varepsilon_{22}} & \frac{\sigma_{22}}{(1-d_2)^2 E_2} \frac{\partial d_2}{\partial \varepsilon_{33}} & \frac{\sigma_{22}}{(1-d_2)^2 E_2} \frac{\partial d_2}{\partial \gamma_{12}} & \frac{\sigma_{22}}{(1-d_2)^2 E_2} \frac{\partial d_2}{\partial \gamma_{13}} \\ \frac{\sigma_{33}}{(1-d_3)^2 E_2} \frac{\partial d_3}{\partial \varepsilon_{11}} & \frac{\sigma_{33}}{(1-d_3)^2 E_2} \frac{\partial d_3}{\partial \varepsilon_{22}} & \frac{\sigma_{33}}{(1-d_3)^2 E_2} \frac{\partial d_3}{\partial \varepsilon_{33}} & \frac{\sigma_{33}}{(1-d_3)^2 E_2} \frac{\partial d_3}{\partial \gamma_{12}} & \frac{\sigma_{33}}{(1-d_3)^2 E_2} \frac{\partial d_3}{\partial \gamma_{13}} \\ \frac{\sigma_{12}}{(1-d_6)^2 G_{12}} \frac{\partial d_6}{\partial \varepsilon_{11}} & \frac{\sigma_{12}}{(1-d_6)^2 G_{12}} \frac{\partial d_6}{\partial \varepsilon_{22}} & \frac{\sigma_{12}}{(1-d_6)^2 G_{12}} \frac{\partial d_6}{\partial \varepsilon_{33}} & \frac{\sigma_{12}}{(1-d_6)^2 G_{12}} \frac{\partial d_6}{\partial \gamma_{12}} & \frac{\sigma_{12}}{(1-d_6)^2 G_{12}} \frac{\partial d_6}{\partial \gamma_{13}} \\ \frac{\sigma_{13}}{(1-d_6)^2 G_{12}} \frac{\partial d_6}{\partial \varepsilon_{11}} & \frac{\sigma_{13}}{(1-d_6)^2 G_{12}} \frac{\partial d_6}{\partial \varepsilon_{22}} & \frac{\sigma_{13}}{(1-d_6)^2 G_{12}} \frac{\partial d_6}{\partial \varepsilon_{33}} & \frac{\sigma_{13}}{(1-d_6)^2 G_{12}} \frac{\partial d_6}{\partial \gamma_{12}} & \frac{\sigma_{13}}{(1-d_6)^2 G_{12}} \frac{\partial d_6}{\partial \gamma_{13}} \end{bmatrix}$$

283 Calculating the time derivative of equations (1) and (7) and using equation (30), results in:

$$\dot{\boldsymbol{\zeta}} = \dot{\mathbf{T}}^T \begin{Bmatrix} \sigma \\ 0 \end{Bmatrix} + \mathbf{T}^T \begin{bmatrix} \tilde{\mathbf{C}} & \mathbf{0} \\ \mathbf{0} & 0 \end{bmatrix} \dot{\mathbf{T}} \boldsymbol{\epsilon} + \mathbf{T}^T \begin{bmatrix} \tilde{\mathbf{C}} & \mathbf{0} \\ \mathbf{0} & 0 \end{bmatrix} \mathbf{T} \dot{\boldsymbol{\epsilon}} \quad (31)$$

284 Consider now a fixed coordinate system that coincides, at given instant, with the moving  
 285 coordinate system. In this fixed coordinate system the transformation matrix is the identity  
 286  $\mathbf{T} = \mathbf{I}$ , and its time derivative is:  $\dot{\mathbf{T}} = \frac{\partial \mathbf{T}}{\partial \epsilon_{23}} \Big|_{\epsilon_{23}=0} \dot{\epsilon}_{23} = \frac{\partial \mathbf{T}}{\partial \theta} \Big|_{\theta=0} \frac{\partial \theta}{\partial \epsilon_{23}} \Big|_{\epsilon_{23}=0} \dot{\epsilon}_{23}$ , i.e.:

$$\dot{\mathbf{T}} = \frac{\dot{\epsilon}_{23}}{\epsilon_{22} - \epsilon_{33}} \begin{bmatrix} 0 & 0 & 0 & 0 & 0 & 0 \\ 0 & 0 & 0 & 0 & 0 & 1 \\ 0 & 0 & 0 & 0 & 0 & -1 \\ 0 & 0 & 0 & 0 & -1 & 0 \\ 0 & 0 & 0 & 1 & 0 & 0 \\ 0 & -2 & 2 & 0 & 0 & 0 \end{bmatrix} \quad (32)$$

287 Using (32) in (31), the tangent stiffness matrix can be expressed as a function of the matrix  $\hat{\mathbf{C}}$ :

$$\hat{\mathbf{C}} = \begin{bmatrix} \tilde{\mathbf{C}} & \mathbf{c} \\ \mathbf{0} & \frac{\sigma_{22} - \sigma_{33}}{2(\epsilon_{22} - \epsilon_{33})} \end{bmatrix}, \text{ with } \mathbf{c} = \frac{1}{\epsilon_{22} - \epsilon_{33}} \begin{bmatrix} \tilde{C}_{15}\epsilon_{12} - \tilde{C}_{14}\epsilon_{13} \\ \tilde{C}_{25}\epsilon_{12} - \tilde{C}_{24}\epsilon_{13} \\ \tilde{C}_{35}\epsilon_{12} - \tilde{C}_{34}\epsilon_{13} \\ \tilde{C}_{45}\epsilon_{12} - \tilde{C}_{44}\epsilon_{13} + \sigma_{13}/2 \\ \tilde{C}_{55}\epsilon_{12} - \tilde{C}_{54}\epsilon_{13} - \sigma_{12}/2 \end{bmatrix} \quad (33)$$

288 To calculate the tangent stiffness tensor ( $\dot{\boldsymbol{\zeta}} = \mathbf{C}_T \dot{\boldsymbol{\epsilon}}$ ) in the global coordinate system it is necessary  
 289 to rotate the matrix  $\hat{\mathbf{C}}$  using the angle  $\theta$  as:  $\mathbf{C}_T = \mathbf{T}^T \hat{\mathbf{C}} \mathbf{T}$ . The constitutive model results in an  
 290 explicit formulation where no iterations are required to update the state variables. The model  
 291 developed was implemented in ABAQUS non-linear finite element code [46] using a user-defined  
 292 subroutine UMAT, according to the following algorithm:

1	-	Strain tensor at current time $t$	$\epsilon^t$
2	-	Main transverse direction	$\theta^t$
3	-	Main transverse strains	$\begin{Bmatrix} \epsilon^t \\ 0 \end{Bmatrix} = \mathbf{T}^t \epsilon^t$
4	-	Effective stress tensor	$\tilde{\sigma}^t = \mathbf{H}_0^{-1} \epsilon^t$
5	-	Loading functions	$\phi_M^t(\tilde{\sigma}^t)$
6	-	Internal variables	$r_M^t(r_M^{t-1}, \phi_M^t)$
7	-	Damage variables	$d_M^t(r_M^t)$
8	-	Nominal stress tensor	$\sigma^t = (\mathbf{H}^t)^{-1} \epsilon^t$
9	-	Rotated nominal stress tensor	$\varsigma^t = (\mathbf{T}^t)^T \begin{Bmatrix} \sigma^t \\ 0 \end{Bmatrix}$
10	-	Tangent constitutive tensor	$\mathbf{C}_T^t = (\mathbf{T}^t)^T \hat{\mathbf{C}}^t \mathbf{T}^t$

293

### 294 3 Model verification

295 To evaluate the accuracy of the model proposed, the numerical predictions are compared with  
 296 published experimental results. The example selected for the assessment of the accuracy of  
 297 the model corresponds to the prediction of the onset and accumulation of transverse matrix  
 298 cracks and of final failure of multidirectional laminates. This is a relevant scenario because the  
 299 transverse matrix cracks that may develop at low strains affect the thermomechanical properties  
 300 of the laminate, create paths for fuel leakage, and may trigger other failure mechanisms.

301 Several analytical solutions have been proposed to predict the effects of transverse matrix  
 302 cracks in the thermomechanical properties of multidirectional laminates [48] -[55]. Generally,  
 303 these analytical solutions are valid for simple boundary conditions and applied loads, and  
 304 for situations where the transverse matrix cracks accumulate in a central 90° ply. When the  
 305 cracked 90° ply is placed at the surface of the laminate the analytical solutions are in general  
 306 no longer valid. In addition, there are situations where delamination develops, either preceding  
 307 transverse matrix cracks or at high densities of such cracks [56]. The model proposed here is  
 308 able to simulate the different failure scenarios where the analytical solutions are no longer valid.

#### 309 3.1 Statistical distribution of properties

310 The stress field of an unnotched laminate is uniform, except in regions close to the free edge  
 311 where a three-dimensional stress field occurs. This means that the damage activation functions  
 312 are satisfied in more than one point simultaneously in the numerical implementation of the

313 model. To overcome this difficulty, and to enforce the localization of damage in a plane, a  
314 random strength field is created.

315 The inclusion of random material properties in the finite element mesh is an active research topic  
316 [57]-[58]. The definition of random material properties must take into account the characteristic  
317 length of the finite element and should be applied to all material properties, not only to the mean  
318 and to the standard deviation, but even to the density function itself. The topic of statistical  
319 finite element analysis is outside the scope of this paper. Therefore, the application of random  
320 material properties is done simply by defining a random strength with a normal distribution.

321 A simple way to define a normal distribution is by means of the Box-Muller algorithm [59].  
322 The Box-Muller algorithm states that if  $a$  and  $b$  are uniformly distributed numbers in  $(0,1]$  a  
323 standard normally distributed random variable is  $X$  given as:  $X = \sqrt{-2 \ln a} \cos(2\pi b)$ .

324 If the maximum and minimum strength values,  $Y_T^{\max}$  and  $Y_T^{\min}$ , respectively are known, the  
325 mean strength value is  $\mu = (Y_T^{\min} + Y_T^{\max})/2$  and the variance is given as  
326  $3\sigma = \mu - Y_T^{\min} = Y_T^{\max} - \mu$ . The random normally distributed strength variable is:  $Y_T =$   
327  $1/2 (Y_T^{\max} + Y_T^{\min}) + 1/6 (Y_T^{\max} - Y_T^{\min}) X$ .

### 328 3.2 Kinematics of crack growth

329 The predictions of the onset and growth of transverse matrix cracks use a  $[0_2/90_4]_s$  laminate,  
330 with the material properties shown in Tables 2 and 3. A typical value of  $G_{L+}$  for glass fibers is  
331 used in the simulations.

332 [Table 2 about here.]

333 [Table 3 about here.]

334 Eight-node solid elements (Abaqus C3D8 elements) are used in the fully three-dimensional nu-  
335 merical models. The models use two elements through the thickness of each ply. The specimen  
336 modeled has all the nodes in one end clamped, whereas the other extremity is subjected to an  
337 uniform displacement.

338 The process of crack propagation in a  $[0_n/90_m]_s$  is qualitatively shown in the Figures 3 and  
339 4. The damage variable  $d_2$  and the principal strain are plotted at different stages of cracking  
340 process in Figure 3. As expected, damage initiates at the free edge of the laminate. When  
341 increasing the external load, the strain localizes and transverse matrix cracks develop. Steps  
342 3-5 shown in Figure 3 represent the evolution of the cracks towards the center of the laminate.  
343 The microcracks in the vicinity of through-the-thickness cracks unload elastically. The process  
344 of crack grow to the center of the laminate is shown in Figure 4. Due the confining effect of  
345 outer plies, the central region of the crack advances faster than the region in the vicinity of the  
346 adjoining plies.

347 [Fig. 3 about here.]

348 [Fig. 4 about here.]

The predictions are consistent with experimental observations [60]-[47] that show that matrix cracks in multiaxial laminates with central  $90^\circ$  plies originate at the free edge and propagate through the specimen width.

When  $[90_n/0_m]_s$  laminates are tested in tension, the matrix cracks appear in the outer plies in an antisymmetrical distribution [48]. Figure 5 shows that antisymmetrical distribution of cracks is correctly captured by the model.

[Fig. 5 about here.]

Figure 6 represents the cracking process at different loading stages. The presence of one crack in the outer ply causes the loss of symmetry of the laminate, and the neutral line moves away from the crack. Therefore the laminate bends in the vicinity of the crack. The strain field in the location where a crack develops is shown in Figure 6.

[Fig. 6 about here.]

The previous results show that the proposed damage model is able to qualitatively represent the process of matrix cracking. This is due the ability of the finite element model to describe the kinematics of cracking process with a reasonable accuracy.

### 3.3 Effects of transverse cracks on the laminate stiffness

Varna *et al.* [49]-[51] presented the response of unnotched  $[\pm\theta/90_4]_s$  ( $\theta = 0^\circ, 15^\circ, 30^\circ, 40^\circ$ ) glass/epoxy laminates loaded in tension. The reduction of the laminate Youngs modulus ( $E_x$ ) and Poisson ratio ( $\nu_{xy}$ ) were reported as a function of the laminate strain ( $\varepsilon_{xx}$ ), where the direction  $x$  coincides with  $\theta = 0^\circ$ . The material properties are obtained from [49]-[51] and summarized in the Tables 2 and 3.

To simulate the thermal residual strains produced due the curing process, a temperature change of  $\Delta T = -105^\circ\text{C}$  is applied. The ply thickness is  $t = 0.144\text{mm}$ . The other parameters required by the model are  $H_{T-} = 0.4$ ,  $X_{PO} = 600\text{MPa}$ ,  $G_L^E = G_L^L = 30\text{N/mm}$ , and  $A_L^\pm = 0$ .

The finite element model has a length of 8mm and, taking advantage of the symmetry, only the one-half of the laminate thickness is modeled. The mesh consists of C3D8 elements with a characteristic length of 0.072mm. To reduce the CPU time the specimen width is modeled with only one row of finite elements. Multi point constraints are introduced in the model as proposed in [65], to represent a state of generalized plane strain. A first thermal step is applied to represent the curing process. A prescribed displacement is applied to one end of the specimen, while the opposite end is clamped.

No transverse damage are considered in the outer plies when  $\theta \neq 90^\circ$  plies are modeled. In these laminates, matrix cracks develop in the direction described by the ply orientation, and the boundary conditions used in the the model are no longer valid.

The maximum transverse strength used is  $Y_T^{\max} = 200\text{MPa}$ . Therefore, the mean strength is 125MPa and the standard variation is 25MPa. The strength value  $S_L$  and  $Y_C$  are also randomized with a mean value of 180MPa and 295MPa, respectively. The standard deviation is

386 of 36MPa and 59MPa, respectively. The determination of the random strength properties was  
387 based on the  $[0_2/90_4]_s$  laminate, and was keep constant in the other models. The influence of the  
388 random properties on the crack pattern is small. The statistical distribution mainly influences  
389 the onset of damage.

390 It should be noted that the response of the material is quite sensitive to the finite element length.  
391 The sensitivity to the finite element length is unrelated to the common problem computing the  
392 energy dissipation as a function of the element length; this problem is solved by virtue of  
393 equation 16. The mesh dependency observed is due to the relation between the element size  
394 and the statistical distribution used. The solution of this problem is outside the scope of this  
395 work.

396 For the  $[0_2/90_4]_s$  laminate, the predicted failure strain is  $\varepsilon_{xx}^u = 0.022\text{mm/mm}$  and the collapse  
397 of the laminate occurs when fibre fracture develops in the the outer  $0^\circ$  plies. The predicted value  
398 is smaller than the one obtained using classical laminate theory, which is  $\varepsilon_{xx}^u = 0.023\text{mm/mm}$ .  
399 This fact is due the stress concentration that the matrix cracks cause in the outer plies, which in  
400 turn leads to laminate failure. The mean stress-strain response up to laminate failure is shown  
401 in Figure 7.

402 [Fig. 7 about here.]

403 Figures 8 to 11 show the internal variable  $r_T$  and the transverse damage variable  $d_{T+}$  at a mean  
404 strain  $\varepsilon_{xx} = 0.01\text{ mm/mm}$ . The pattern of the internal variable clearly shows the localization of  
405 the deformations, which represent transverse cracks. The predicted distribution of the damage  
406 variable indicates that delamination develops at the tip of the transverse matrix crack.

407 At the mean strain of  $\varepsilon_{xx} = 0.01\text{mm/mm}$ , the  $[0_2/90_4]_s$  laminate shows three cracks, cor-  
408 responding to a crack density of 0.375 cracks/mm. The predicted crack density of the other  
409 laminates is 0.25 cracks/mm. These values are in reasonable agreement with the values reported  
410 by Varna [49], which are 0.34 cracks/mm for the  $[0_2/90_4]_s$  laminate, 0.28 cracks/mm for the  
411  $[\pm 15/90_4]_s$  laminate, 0.24 cracks/mm for the  $[\pm 30/90_4]_s$  laminate, and 0.15 cracks/mm for the  
412  $[\pm 40/90_4]_s$  laminate.

413 [Fig. 8 about here.]

414 [Fig. 9 about here.]

415 [Fig. 10 about here.]

416 [Fig. 11 about here.]

417 Figure 12 shows the longitudinal and transverse tension damage variable at the maximum load  
418 and after laminate failure. It is possible to observe that laminate failure is due to fiber tensile  
419 fracture of the adjoining plies, which in turn is triggered by the transverse matrix cracks that  
420 develop in the inner  $90^\circ$  layer.

421 [Fig. 12 about here.]

422 The reduction in the laminate's Young modulus and Poisson ratio are shown in Figures 13 to 16.  
423 The Young modulus is calculated using the predicted load,  $P$ , the predicted end-displacement,  
424  $\delta$ , the specimen's cross-section area,  $A$ , and length,  $L$ , as  $E_x = \frac{PL}{A\delta}$ . It is observed that the crack

grows in the transverse direction until reach a critical length is reached; afterwards, the crack grows unstably with an associated amount of spare energy that produce the oscillations that are visible in the response. The numerical results are in good agreement with the experimental results reported by Varna *et al.* [49]-[51].

[Fig. 13 about here.]

[Fig. 14 about here.]

[Fig. 15 about here.]

[Fig. 16 about here.]

### 3.4 Simulation of delamination

The model is further validated by simulating an unidirectional specimen with a cut across the width of one central ply. When loaded in tension, such type of specimen promotes delamination growth in mode II [66] before the outer plies fail by fiber tensile fracture.

The specimen under investigation was tested at the German Aerospace Centre (DLR) [67], and it consists of a 977-2 HTS [0°] CFRP laminate where the central ply was cut across the entire width of the specimen. The relevant material properties are shown in Tables 4 and 5. The nominal ply thickness is 0.25mm.

[Table 4 about here.]

[Table 5 about here.]

Five specimens were tested and the mean value of the remote stress at delamination propagation, defined as the ratio between the load and the cross section area of the specimen, is 1753MPa.

The modeling strategy used here consists in imposing generalized plane strain conditions to Abaqus C3D8 8-node continuum elements by applying the kinematic relations proposed in [65]. The nodes at one end of the specimen are clamped and a displacement in the longitudinal direction is applied to the nodes at the other end. In addition, symmetry along the 1-2 (longitudinal-transverse) midplane of the specimen is imposed. The ply cut was simulated by a line of elements with all the damage variables set to one. The mesh of the specimen under investigation is shown in Figure 17.

[Fig. 17 about here.]

Figure 18 shows the predicted relation between the end displacement of the specimen and the remote stress. The propagation of delamination corresponds to the horizontal plateau predicted by the model.

[Fig. 18 about here.]

Figures 19 and 20 show the the sequence of the failure mechanisms that occur in the specimen.

[Fig. 19 about here.]

[Fig. 20 about here.]

It is observed that the ply cut triggers a delamination between the central ply and the adjoining plies, that propagates in mode II along the length of the specimen. The specimen is able to sustain increasing loads until it completely fails as a result of the fiber fracture in the adjoining plies. This sequence of events was also observed in the experiments. In addition, the predicted remote stress at delamination propagation, 1782.4MPa, correlates well with the mean value measured in the experiments, 1753MPa.

## 4 Conclusions

A fully three-dimensional continuum damage model able to predict the different failure mechanisms that may occur in laminated composites was proposed. The constitutive model is formulated in the formalism of the thermodynamics of irreversible processes and its numerical implementation ensures a mesh-independent prediction of energy dissipation by using the crack band model.

The preliminary validation examples indicate that the model is able to capture the kinematics of the propagation of transverse matrix cracks for quasi-isotropic laminates with general locations of the  $90^\circ$  plies. The comparison between the model predictions and published experimental data show that the model is able to accurately predict the relation between the applied strain and the residual stiffness of quasi-isotropic laminates, final failure of the laminates, as well as the effect of the stiffness of the adjoining sublaminates on the density of transverse matrix cracks. In addition, the model is able to represent at the constitutive level both delamination and transverse matrix cracks as well as the interaction between these two failure mechanisms that occurs at in glass-epoxy quasi-isotropic laminates at high applied strains.

Based on the results of the simulation of a CFRP specimen with a central cut ply it is concluded that the model accurately represents delamination onset and propagation in mode II, and the final fracture of the laminate as a result of fiber fracture. It should be emphasized that this sequence of events is predicted without recurring to special purpose cohesive elements, but using an appropriate constitutive model for the composite ply.

The future research of the authors will include a further validation of the model presented in this paper for loading scenarios that trigger compression and shear-dominated failure mechanisms.

## Acknowledgements

The research visit of the first author to the University of Porto, Portugal, was funded by the Ministerio de Educación y Ciencia of the Spanish government through the grant "José Castillejo". The first and third authors acknowledge funding from the Spanish government through CICYT under the contract TRA2006-15718-C02-01/TAIR.

The support of the Portuguese Foundation for Science and Technology (FCT) under the project PDCTE/50354/EME/2003 is acknowledged by the second author.

Effort sponsored by the Air Force Office of Scientific Research, Air Force Material Command, USAF, under grant number FA8655-06-1-3072. The U.S. Government is authorized to reproduce and distribute reprints for Governmental purposes notwithstanding any copyright notation thereon.

The authors would like to thank Dipl.-Ing. Axel Fink García and the German Aerospace Center for providing the experimental data used in the simulation of delamination.

## References

- [1] Harris CE, Starnes JH, Shuart MJ. An assessment of the state-of-the-art in the design and manufacturing of large composite structures for aerospace vehicles. NASA TM-2001-210844, 2001.
- [2] Krueger R, Paris IL, O'Brien TK, Minguet PJ. Comparison of 2D finite element modeling assumptions with results from 3D analysis for composite skin-stiffener debonding. *Composite Structures*. 2002;57:161-168.
- [3] Alfano G, Crisfield MA. Finite Element Interface Models for the Delamination Analysis of Laminated Composites: Mechanical and Computational Issues. *International Journal for Numerical Methods in Engineering* 2001; 50:1701-1736.
- [4] Allix O, Corigliano A. Geometrical and interfacial non-linearities in the analysis of delamination in composites. *International Journal of Solids and Structures*. 1999; 36:2189-2216.
- [5] Camanho PP, Dávila CG, Moura MF. Numerical simulation of mixed-mode progressive delamination in composite materials. *Journal of Composite Materials*. 2003; 37(16):1415-1438.
- [6] Turon A, Camanho PP, Costa J, Dávila CG. A damage model for the simulation of delamination in advanced composites under variable-mode loading. *Mechanics of Materials*. 2006; 38:1072-1089.
- [7] de Borst R. Theoretical and computational issues in localisation and failure. *European Congress on Computational Methods in Applied sciences and Engineering*; 2000 Sep; Barcelona. Barcelona: ECCOMAS; 2000: 1-15.
- [8] Jansson NE, Larsson R. A damage model for simulation of mixed-mode delamination growth. *Composite Structures*. 2001; 53:409-417.
- [9] Li X, Hallett SR, Wisnom MR. Predicting the effect of through-thickness compressive stress on delamination using interface elements. *Composites-Part A*. in press.
- [10] Soden PD, Hinton MJ, Kaddour AS. A comparison of the predictive capabilities of current failure theories for composite laminates. *Composites Science and Technology*. 1998; 58:1225-1254.
- [11] Hashin Z. Failure Criteria for Unidirectional Fiber Composites. *Journal of Applied Mechanics*. 1980; 47:329-334.
- [12] Puck A, Schürmann H. Failure analysis of FRP laminates by means of physically based phenomenological models. *Composites Science and Technology*. 1998; 58:1045-1067.
- [13] Liu KS, Tsai SW. A progressive quadratic failure criterion for a laminate. *Composites Science and Technology*. 1998; 58:1023-1032.
- [14] Dávila CG, Camanho PP, Rose CA. Failure criteria for FRP laminates. *Journal of Composite Materials*. 2005; 39:323-345.



- [15] Pinho ST, Dávila CG, Camanho PP, Iannucci L, Robinson P. Failure models and criteria for FRP under in-plane or three-dimensional stress states including shear non-linearity. NASA/TM-2003-213530, 2004.
- [16] Talreja R. Transverse cracking and stiffness reduction in composite laminates. *Journal of Composite Materials*. 1985; 19:355-375.
- [17] Laws N, Dvorak GJ, Hejazi M. Stiffness changes in unidirectional composites caused by crack systems. *Mechanics of Materials*. 1983; 2:123-137.
- [18] Hashin Z. Analysis of stiffness reduction of cracked cross-ply laminates. *Engineering Fracture Mechanics*. 1986; 25(5/6):771-778.
- [19] Mayugo JA, Camanho PP, Maimí P, Dávila CG. A micromechanics-based damage model for  $(\pm\theta/90_n)_s$  laminates. NASA/TM-2006-214285, 2006.
- [20] Nuismer RJ, Tan SC. Constitutive Relations of a Cracked Composite Lamina. *Journal of Composite Materials*. 1988; 22:306-321.
- [21] McCartney LN. Energy-based prediction of progressive ply cracking and strength of general symmetric laminates using an homogenisation method. *Composites-Part A*. 2005; 36:119-128.
- [22] Allen DH, Harris CE, Groves SE. A thermomechanical constitutive theory for elastic composites with distributed damage- I. theoretical development. *International Journal of Solids and Structures*. 1987; 23(9):1301-1318.
- [23] Barbero EJ, De Vivo L. A constitutive model for elastic damage on fibre-reinforced PMC laminae. *Journal of Damage Mechanics*. 2001; 10(1):73-93.
- [24] Camanho PP, Maimí P, Dávila CG. Prediction of size effects in notched laminates using continuum damage mechanics. *Composites Science and Technology*. 2007; 67:2715-2727.
- [25] Ladevèze P, Allix O, Deü JF, Lévêque D. A mesomodel for localisation and damage computation in laminates. *Computer Methods in Applied Mechanics and Engineering*. 2000; 183:105-122.
- [26] Maimí P, Camanho PP, Mayugo JA, Dávila CG. A continuum damage model for composite laminates: part I - constitutive model. *Mechanics of Materials* 2007;39(10):897-908.
- [27] Maimí P, Camanho PP, Mayugo JA, Dávila CG. A continuum damage model for composite laminates: part II - computational implementation and validation. *Mechanics of Materials*. 2007;39(10):909-919.
- [28] Dávila, CG, Rose, CA, Song, K, Determination of traction-displacement laws for representing R-curve toughening effects, *Proceedings of the ABAQUS User's Conference*, Newport, RI, May 19-22, 2008.
- [29] Matzenmiller A, Lubliner J, Taylor RL, A constitutive model for anisotropic damage in fiber-composites. *Mechanics of Materials* 1995;20:125-152.
- [30] William KV, Vaziri R, Poursartip A. A physically based continuum damage mechanics model for thin laminated composite structures. *Int. J. Solids and Structures*. 2003;40:2267-2300.
- [31] Goyal VK, Jaunky N, Johnson ER, Ambur DR. Intralaminar and interlaminar progressive failure analyses of composite panels with circular cutouts. *Composite Structures*. 2004;64(1):91-105.
- [32] Daudeville L, Allix O, Ladevèze P. Delamination Analysis by Damage Mechanics: Some Applications. *Composites Engineering*. 1995; 5(1):17-24.

- [33] Ladevèze P. A Damage Computational Approach for Composites: Basic Aspects and Micromechanical Relations. *Computational Mechanics*. 1995; 17:142-150.
- [34] Green BG, Wisnom MR, Hallet SR. An experimental investigation into the tensile strength scaling of notched composites. *Composites-Part A*. 2007; 38:867-878.
- [35] Hallett SR, Jian WG, Khan B, Wisnom MR. Modelling the interaction between matrix cracks and delamination damage in scaled quasi-isotropic specimens. *Composites Science and Technology*. 2008; 68:89-90.
- [36] Chaboche J-L, Maire JF. A new micromechanics based CDM model and its application to CMC's. *Aerospace Science and Technology* 2002;6: 131-145.
- [37] Jirásek M, Zimmermann T. Rotating crack model with transition to scalar damage. *Journal of Engineering Mechanics*. 1998;124(3):277-284.
- [38] Carol I, Willam K. Spurious dissipation/generation in stiffness recovery models for elastic degradation and damage. *Int. J. Solid Structures* 1996;33:2939-2957.
- [39] Christensen RM. Stress based yield/failure Criteria for fiber composites *International Journal of Solids and Structures*. 1997 34,5:529-543.
- [40] Simo JC, Ju JW. Strain and stress-based continuum damage models-I. Formulation. *International Journal of Solids and Structures*. 1987;23(23): 821-840.
- [41] Simo JC, Ju JW. Strain and stress-based continuum damage models-II. Computational aspects. *International Journal of Solids and Structures*. 1987;23(23):841-869.
- [42] Bažant ZP, Oh BH. Crack band theory for fracture of concrete. *Materials and structures*. 1983;16:155-177.
- [43] Pinho, ST, Robinson P, Iannucci, L. Fracture toughness of the tensile and compressive fibre failure modes in laminated composites. *Composites Science and Technology*. 2006;66:2069-2079.
- [44] Bažant ZP, Planas J. Fracture and Size effect in concrete and other quasibrittle materials. Ed. W. F. Chen, Purdue University, 1998.
- [45] Cox BN, Marshall DB. Concepts for bridged cracks in fracture and fatigue. *Acta Metallurgica Materialia*. 1994; 42(2):341-363.
- [46] ABAQUS 6.5 User's Manual, ABAQUS Inc., Pawtucket, RI, U.S.A. 2005.
- [47] Bailey JE, Parvizi A. On Fiber Debonding Effects and the Mechanism of Transverse-Ply Failure in Cross-Ply Laminates of Glass/Fiber/Thermoset Composites. *J. Mat. Sci*. 1981;16: 649-659.
- [48] Nairn JA. Matrix microcracking in Composites. *Comprehensive Composite Materials* 2000;2(12):403-432.
- [49] Varna J, Joffe R, Talreja R. Mixed micromechanics and continuum damage mechanics approach to transverse cracking in  $[S, 90_n]_s$  laminates. *Mechanics of Composite Materials*. 2001;37(2):115-126.
- [50] Joffe R, Krasnikovs A, Varna J. COD-based simulation of transverse cracking and stiffness reduction in  $[S, 90_n]_s$  laminates. *Composites Science and Technology* 2001;61:637-656.
- [51] Varna J, Joffe R, Talreja R. A synergistic damage mechanics analysis of transverse cracking in  $[\pm\theta, 90_n]_s$  laminates. *Composites Science and Technology* 2001;61:657-665.

- [52] Mayugo JA, Camanho PP, Maimí P, Dávila CG. A micromechanics-based damage model for  $[\pm\theta, 90_n]_s$  composite laminates. NASA/TM-2006-214285. 2006.
- [53] Hashin Z. Finite thermoelastic fracture criterion with application to laminate cracking analysis. J. Mech. Phys. Solids. 1996;44(7):1129-1145.
- [54] Nuismer RJ, Tan SC. Constitutive Relations of a Cracked Composite Lamina. Journal of Composite Materials. 1988;22:306-321.
- [55] McCartney LN, Schoeppner GA, Becker W. Comparison of models for transverse ply cracks in composite laminates. Composites Science and Technology. 2000;60:2347-2359.
- [56] O'Brien TK. Analysis of local delaminations and their influence on composite laminate behavior. Delamination and Debonding of Materials. 1985; 285-297.
- [57] Vořechovský M. Stochastic fracture mechanics and size effect. PhD Thesis. Institute of Structural Mechanics, Brno University of Technology. 2004.
- [58] Bažant ZP, Pang S-D. Activation Energy Based Extreme Value Statistics and Size Effect in Brittle and Quasibrittle Fracture. Journal of the Mechanics and Physics of Solids. 2007;55:91-131.
- [59] Box GEP, Muller ME. A note on the generation of random normal deviates. Annals Math. Stat, 1958;29:610-611
- [60] Garrett KW, Bailey JE. Multiple Transverse Fracture in  $90^\circ$  Cross-Ply Laminates of a Glass Fibre-Reinforced Polyester. J. Mat. Sci. 1977;12:157-168.
- [61] Garrett KW, Bailey JE. The Effect of Resin Failure Strain on the Tensile Properties of Glass Fiber-Reinforced Cross-Ply Laminates. J. Mat. Sci. 1977;12:2189-2194.
- [62] Parvizi A, Garrett KW, Bailey JE. Constrained Cracking in Glass Fiber-Reinforced Epoxy Cross-Ply Laminates. J. Mat. Sci. 1978;13:195-201.
- [63] Bader MG, Bailey JE, Curtis PT, Parvizi A. The Mechanisms of Initiation and Development of Damage in Multi-Axial Fibre-Reinforced Plastics Laminates. Proc. 3rd Int'l Conf. on Mechanical Behavior of Materials 1979;3:227-239.
- [64] Bailey JE, Curtis PT, Parvizi A. On the Transverse Cracking and Longitudinal Splitting Behavior of Glass and Carbon Fibre Epoxy Cross-Ply Laminates and the Effect of Poisson and Thermally Generated Strains. Proc. R. Soc. Lond. A 1979;366:599-623.
- [65] König M, Krüger R, Kohler E, Kurz M, Ruckstuhl T. Analytical and numerical analysis of a specimen containing a delamination caused by a ply cut. Institute for Statics and Dynamics of Aerospace Structures, University of Stuttgart, 1999; ISD-Report.97(2) Rev. B.
- [66] Wisnom, MR, On the increase of fracture energy with thickness in delamination of unidirectional glass fibre-epoxy with cut central plies. J. Reinforced Plastics and Composites, 1992;11:897-909.
- [67] Fink A, Private Communication, DLR - German Aerospace Center, Institute of Composite Structures and Adaptive Systems, Braunschweig, Germany.

## List of Figures

1	Transverse damage activation function, $F_T = 0$ .	26
2	Transverse and longitudinal stress strain response.	27
3	Propagation of transverse matrix cracks.	28
4	Propagation of transverse crack.	29
5	Distribution of transverse matrix cracks in a $[90/0]_s$ laminate. Deformed scale: 30x.	30
6	Cracking process in a $[90/0]_s$ laminate. Deformed scale: 30x.	31
7	Mean stress strain response of the $[0_2/90_4]_s$ laminate.	32
8	Internal variable $r_T$ and transverse tension damage variable ( $d_{T+}$ ) for a $[0_2/90_4]_s$ laminate. Mean laminate deformation of $\varepsilon_{xx}=0.01$ . Deformed scale: 10x.	33
9	Internal variable $r_T$ and transverse tension damage variable $d_{T+}$ for a $[\pm 15/90_4]_s$ laminate. Mean laminate deformation of $\varepsilon_{xx}=0.01$ . Deformed scale: 10x.	34
10	Internal variable $r_T$ and transverse tension damage variable $d_{T+}$ for a $[\pm 30/90_4]_s$ laminate. Mean laminate deformation of $\varepsilon_{xx}=0.01$ . Deformed scale: 10x.	35
11	Internal variable $r_T$ and transverse tension damage variable $d_{T+}$ for a $[\pm 40/90_4]_s$ laminate. Mean laminate deformation of $\varepsilon_{xx}=0.01$ . Deformed scale: 10x.	36
12	Longitudinal $d_{L+}$ and transverse tension damage variable $d_{T+}$ for a $[0_2/90_4]_s$ laminate at failure load and when the specimen is completely broken. Deformed scale 10x.	37
13	$E_x$ and $\nu_{xy}$ as functions of the applied strain for a $[0_2/90_4]$ laminate. Experimental results from Varna <i>et al.</i> [49]-[51].	38
14	$E_x$ and $\nu_{xy}$ as functions of the applied strain for a $[\pm 15/90_4]_s$ laminate. Experimental results from Varna <i>et al.</i> [49]-[51].	39
15	$E_x$ and $\nu_{xy}$ as functions of the applied strain for a $[\pm 30/90_4]_s$ laminate. Experimental results from Varna <i>et al.</i> [49]-[51].	40
16	$E_x$ and $\nu_{xy}$ as functions of the applied strain for a $[\pm 40/90_4]_s$ laminate. Experimental results from Varna <i>et al.</i> [49]-[51].	41
17	Mesh of the unidirectional specimen.	42
18	Predicted relation between the remote stress and the end displacement.	43
19	Damage variable $d_6$ at 1782.4MPa. Deformed scale: 2x.	44



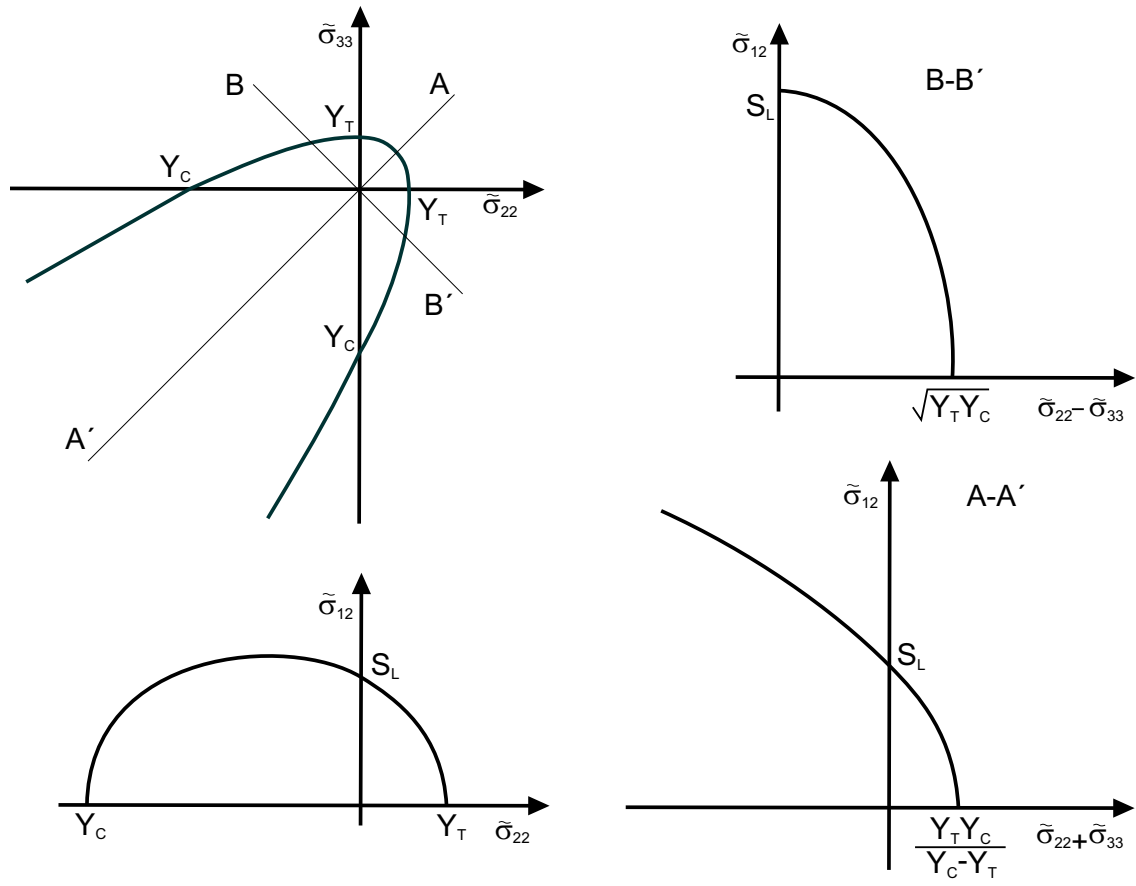


Fig. 1. Transverse damage activation function,  $F_T = 0$ .

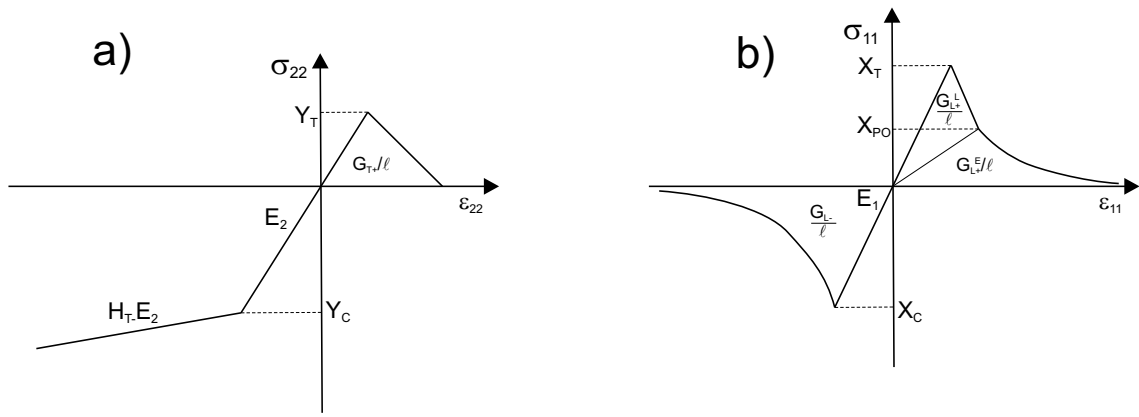


Fig. 2. Transverse and longitudinal stress strain response.

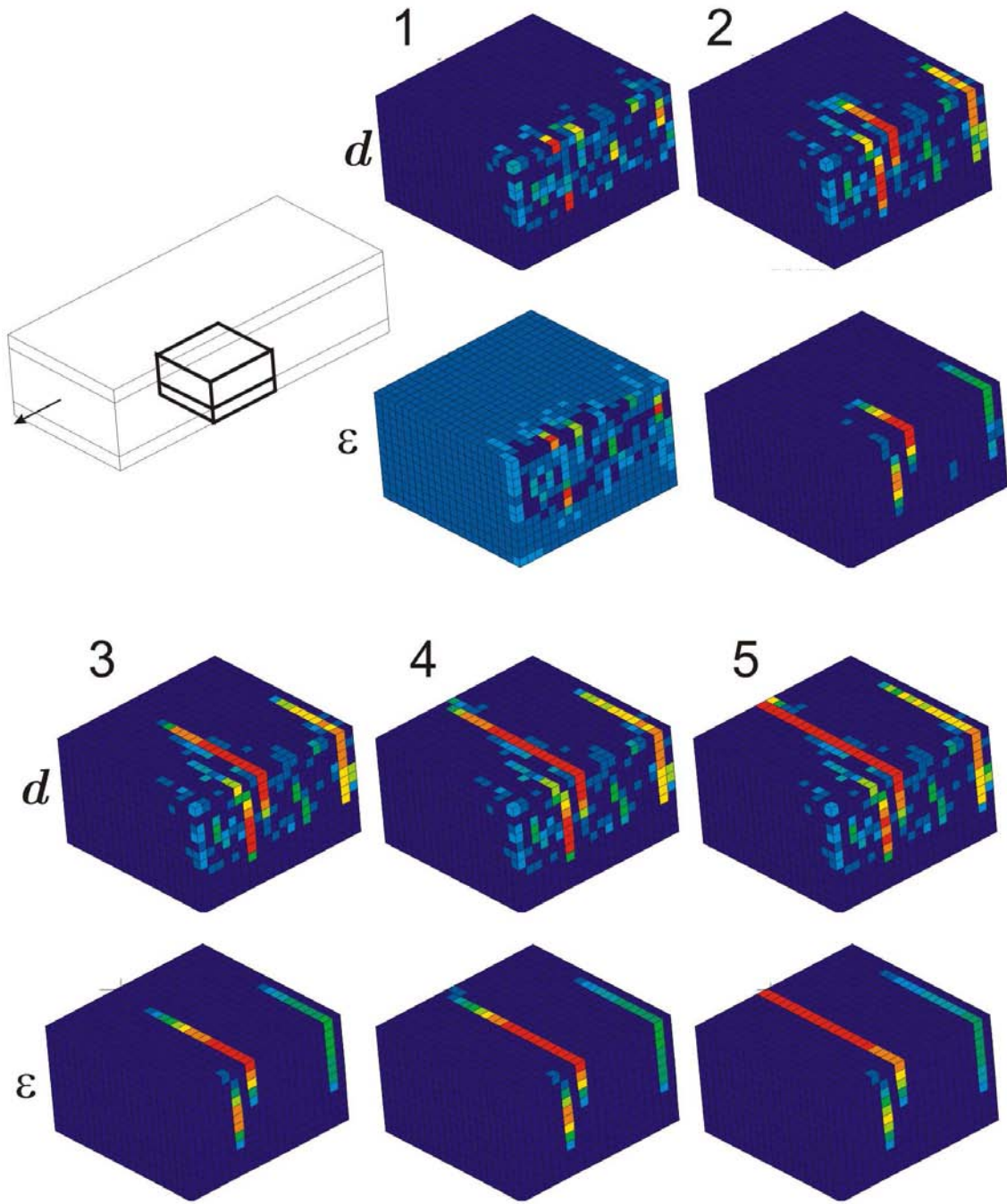


Fig. 3. Propagation of transverse matrix cracks.



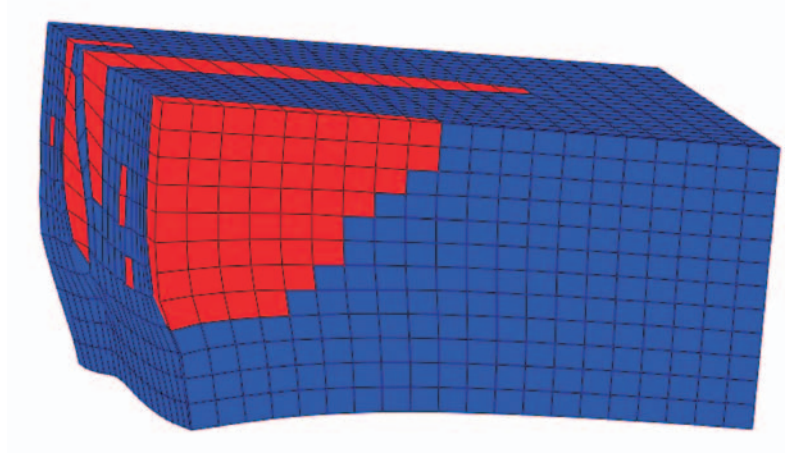
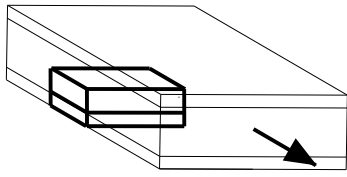


Fig. 4. Propagation of transverse crack.



Fig. 5. Distribution of transverse matrix cracks in a  $[90/0]_s$  laminate. Deformed scale: 30x.

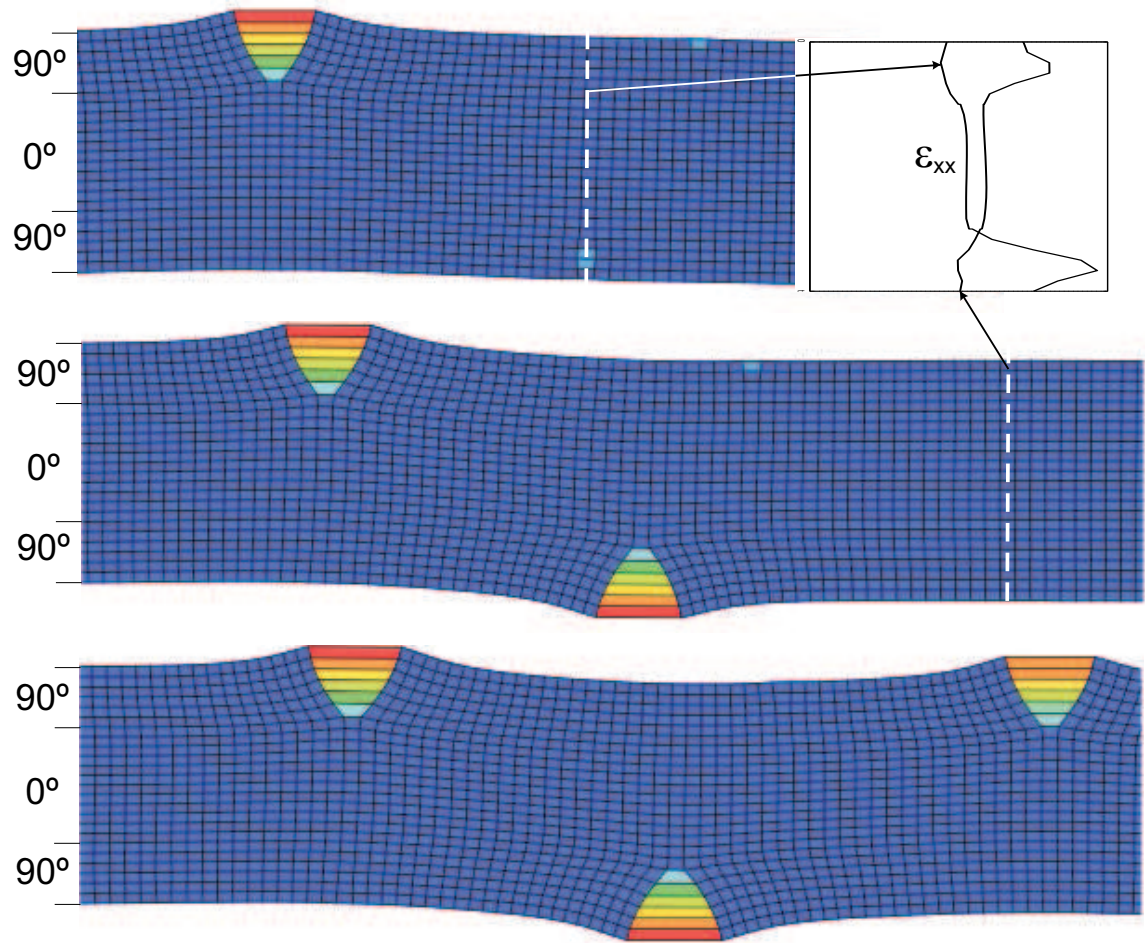


Fig. 6. Cracking process in a  $[90/0]_s$  laminate. Deformed scale: 30x.

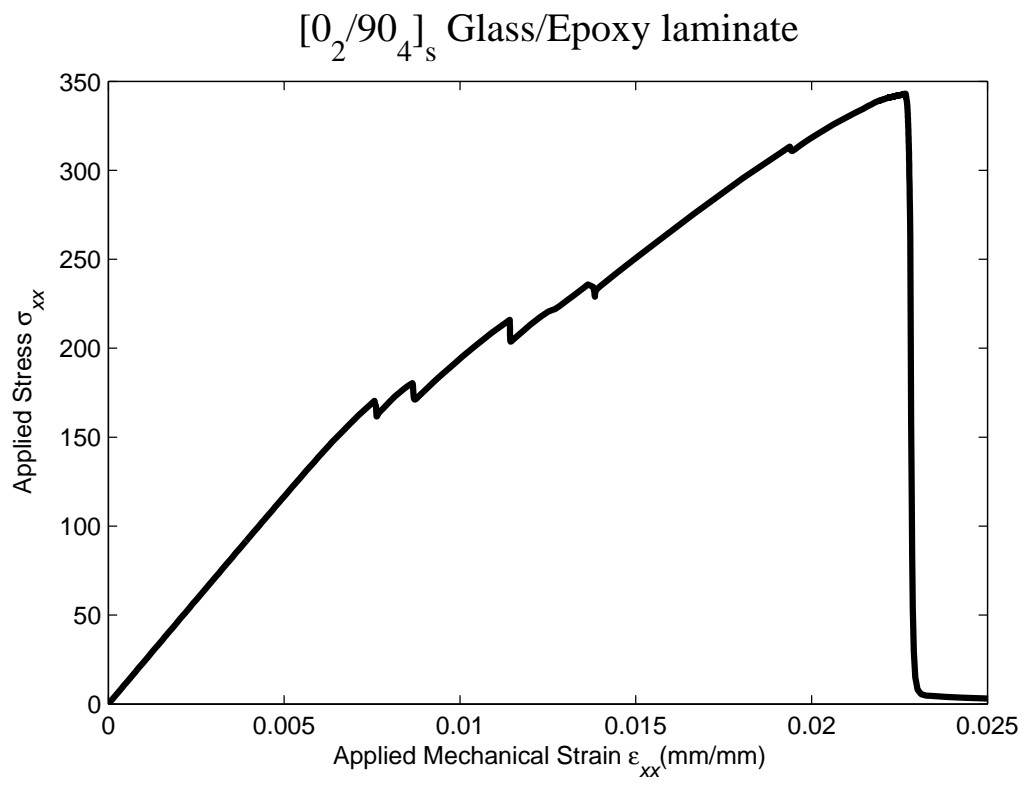


Fig. 7. Mean stress strain response of the  $[0_2/90_4]_s$  laminate.

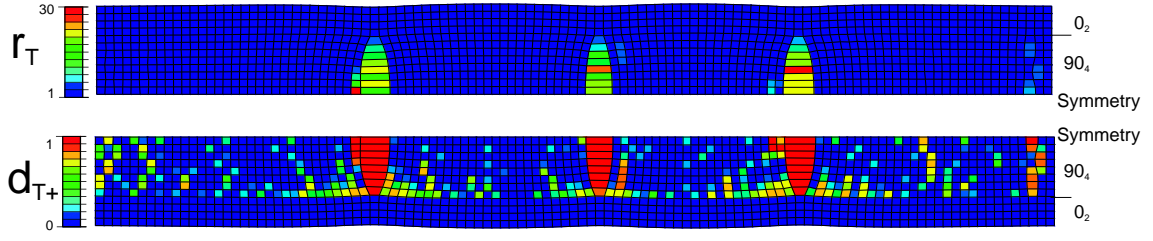


Fig. 8. Internal variable  $r_T$  and transverse tension damage variable ( $d_{T+}$ ) for a  $[0_2/90_4]_s$  laminate. Mean laminate deformation of  $\varepsilon_{xx}=0.01$ . Deformed scale: 10x.

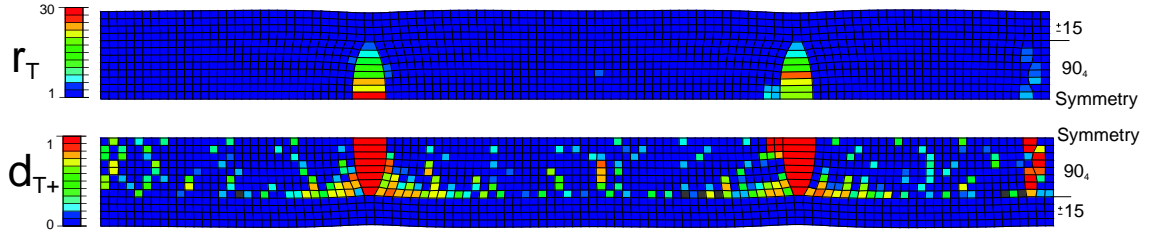


Fig. 9. Internal variable  $r_T$  and transverse tension damage variable  $d_{T+}$  for a  $[\pm 15/90_4]_s$  laminate. Mean laminate deformation of  $\varepsilon_{xx}=0.01$ . Deformed scale: 10x.

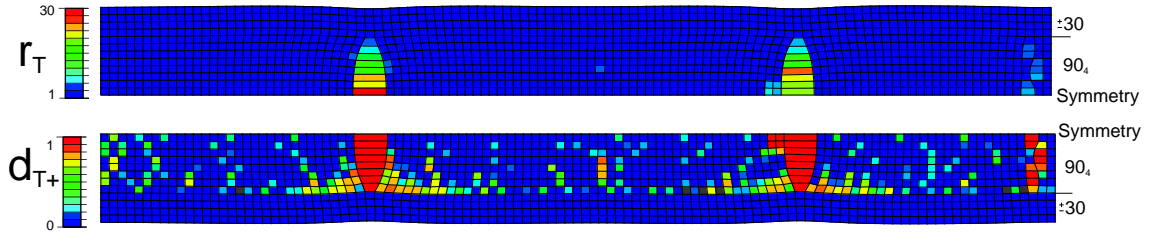


Fig. 10. Internal variable  $r_T$  and transverse tension damage variable  $d_{T+}$  for a  $[\pm 30/90_4]_s$  laminate. Mean laminate deformation of  $\varepsilon_{xx}=0.01$ . Deformed scale: 10x.

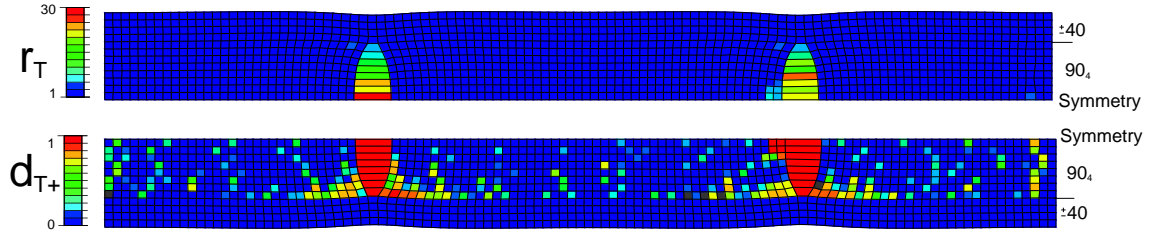


Fig. 11. Internal variable  $r_T$  and transverse tension damage variable  $d_{T+}$  for a  $[\pm 40/90_4]_s$  laminate. Mean laminate deformation of  $\varepsilon_{xx}=0.01$ . Deformed scale: 10x.



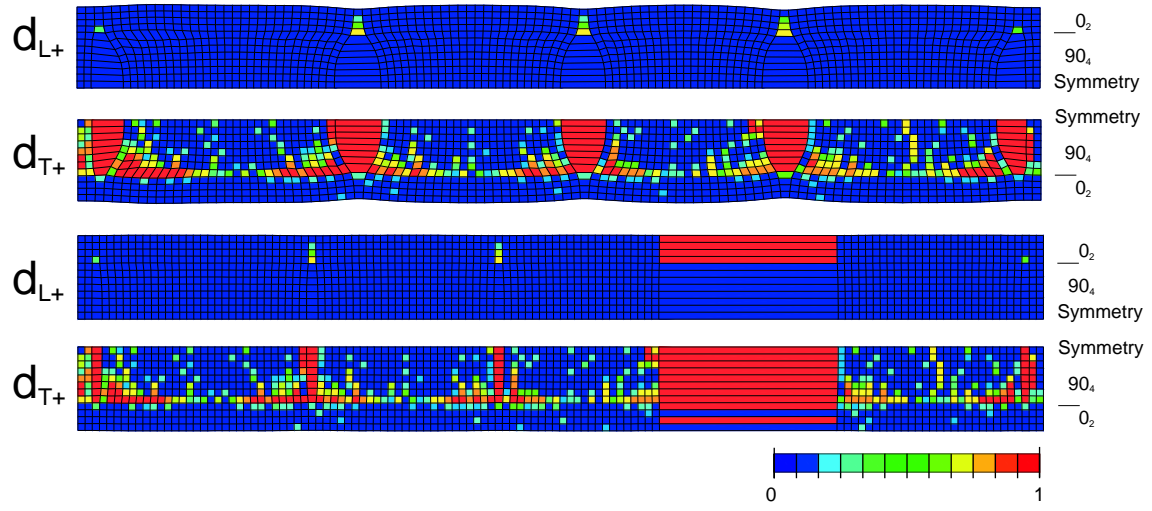


Fig. 12. Longitudinal  $d_{L+}$  and transverse tension damage variable  $d_{T+}$  for a  $[0_2/90_4]_s$  laminate at failure load and when the specimen is completely broken. Deformed scale 10x.

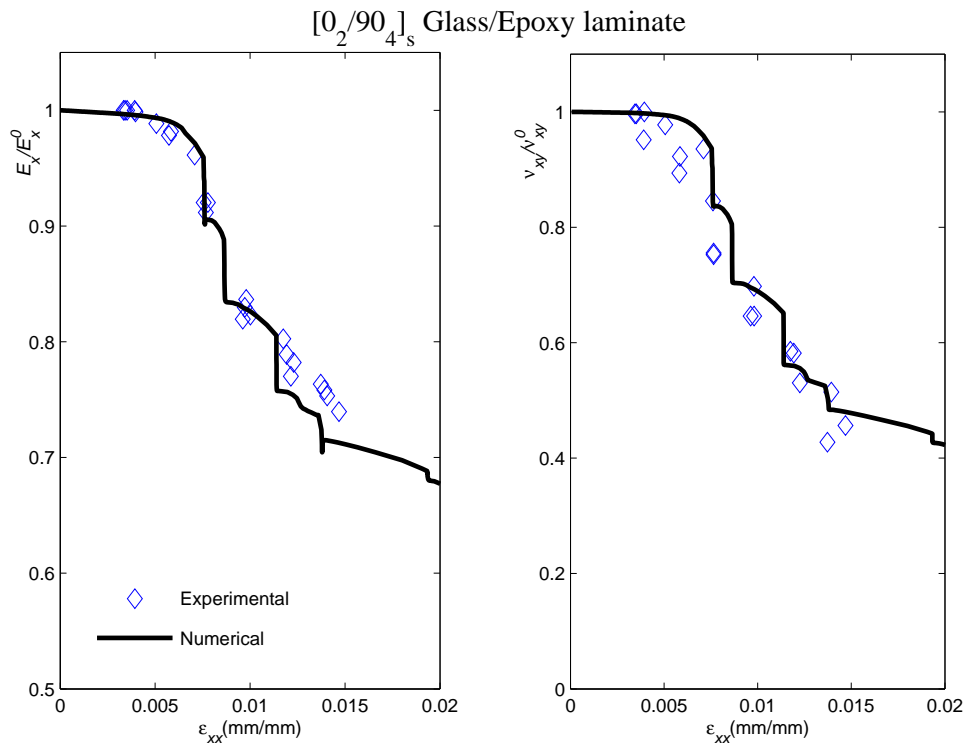


Fig. 13.  $E_x$  and  $\nu_{xy}$  as functions of the applied strain for a  $[0_2/90_4]$  laminate. Experimental results from Varna *et al.* [49]-[51].

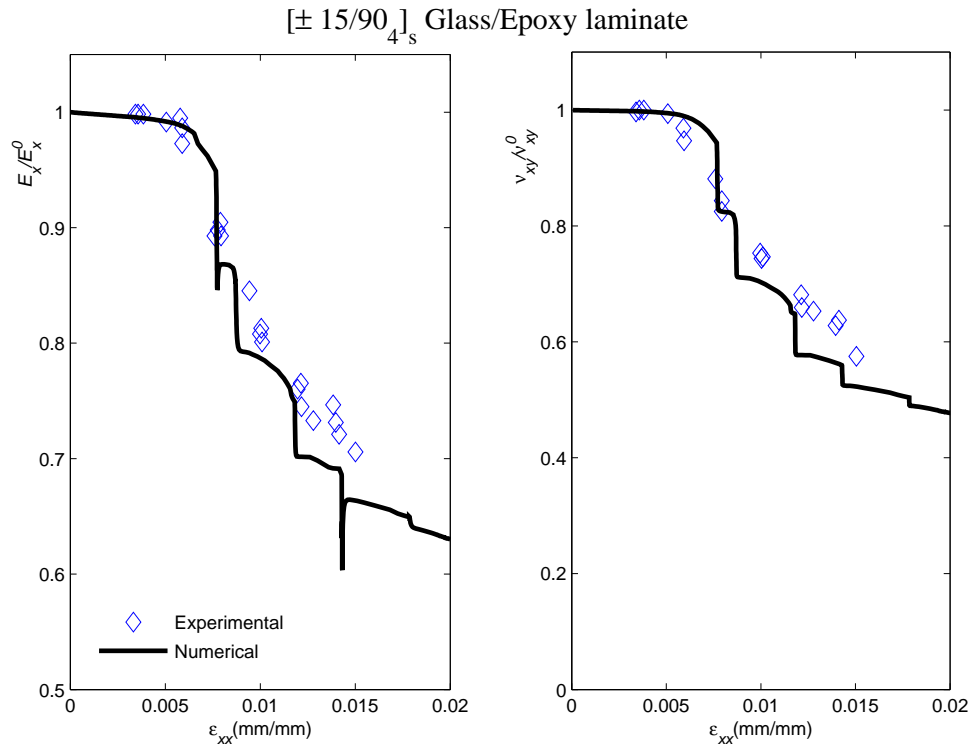


Fig. 14.  $E_x$  and  $\nu_{xy}$  as functions of the applied strain for a  $[\pm 15/90_4]_s$  laminate. Experimental results from Varna *et al.* [49]-[51].

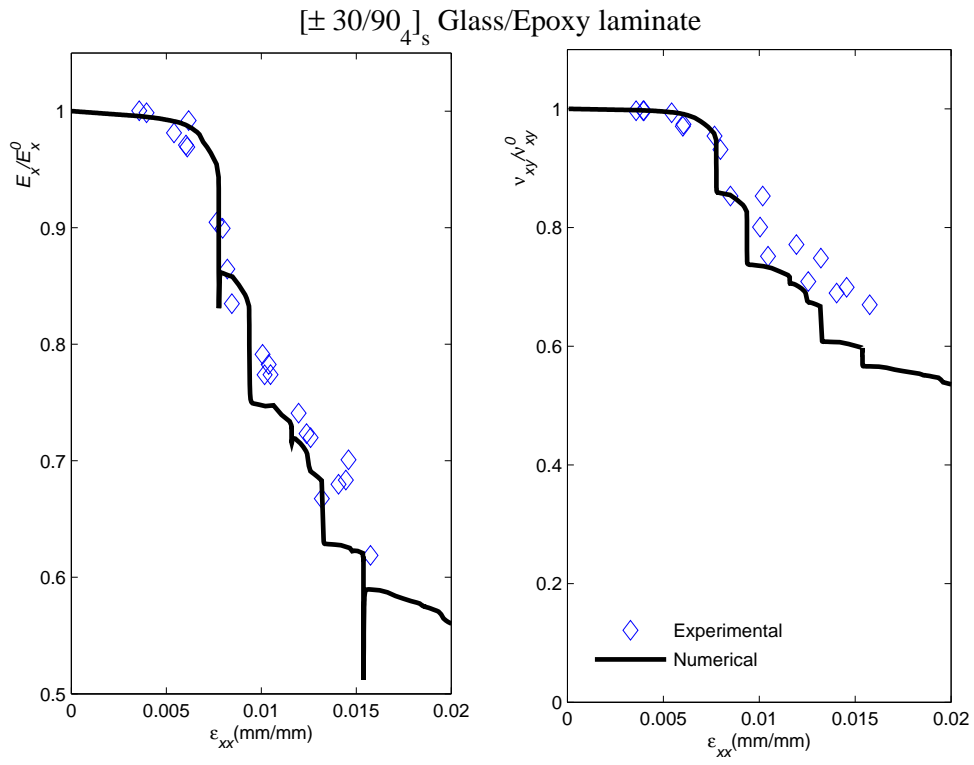


Fig. 15.  $E_x$  and  $\nu_{xy}$  as functions of the applied strain for a  $[\pm 30/90_4]_s$  laminate. Experimental results from Varna *et al.* [49]-[51].

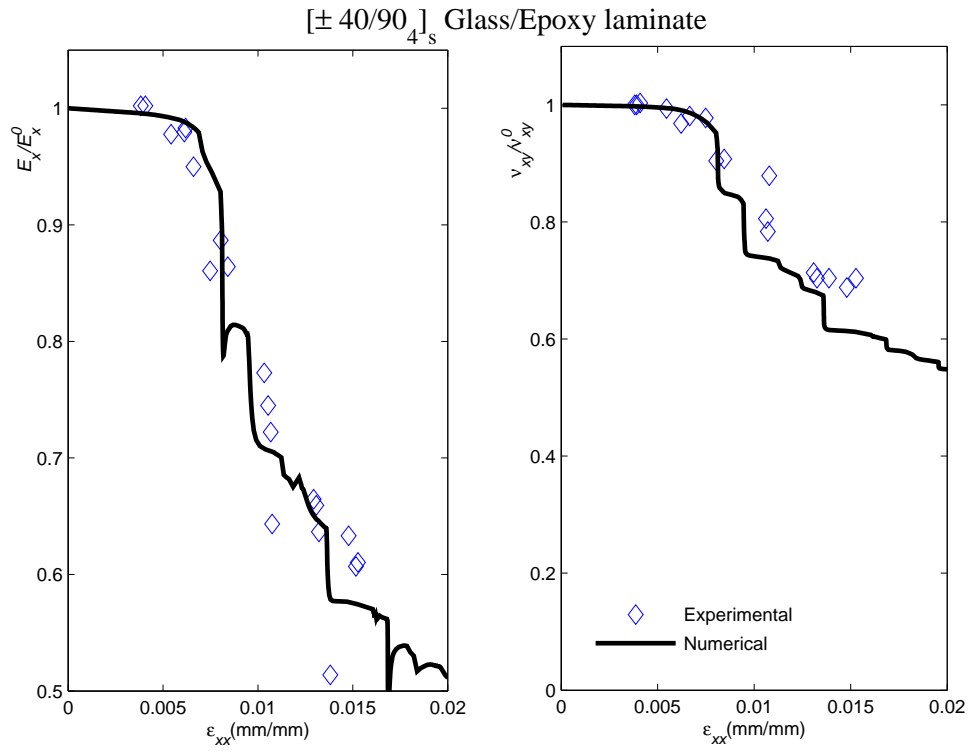


Fig. 16.  $E_x$  and  $\nu_{xy}$  as functions of the applied strain for a  $[\pm 40/90]_4$  laminate. Experimental results from Varna *et al.* [49]-[51].

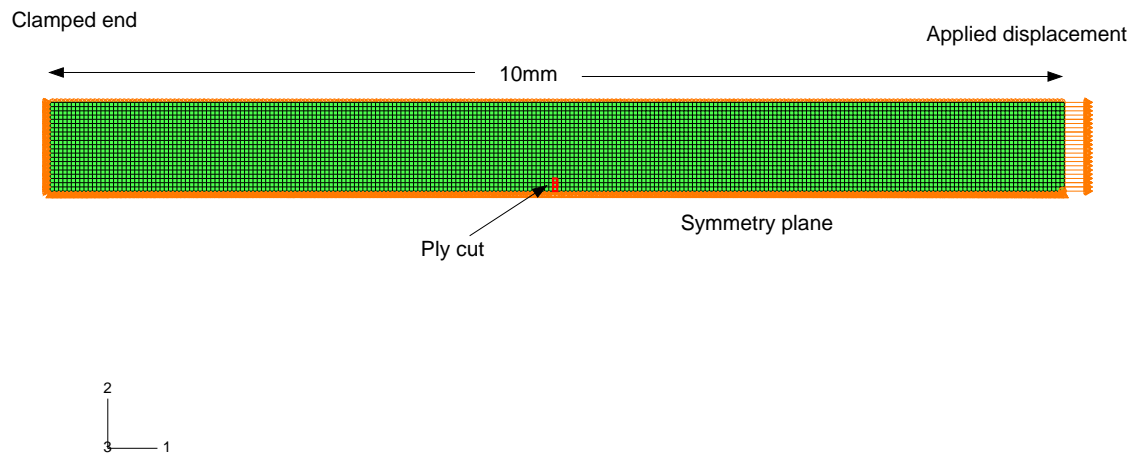


Fig. 17. Mesh of the unidirectional specimen.

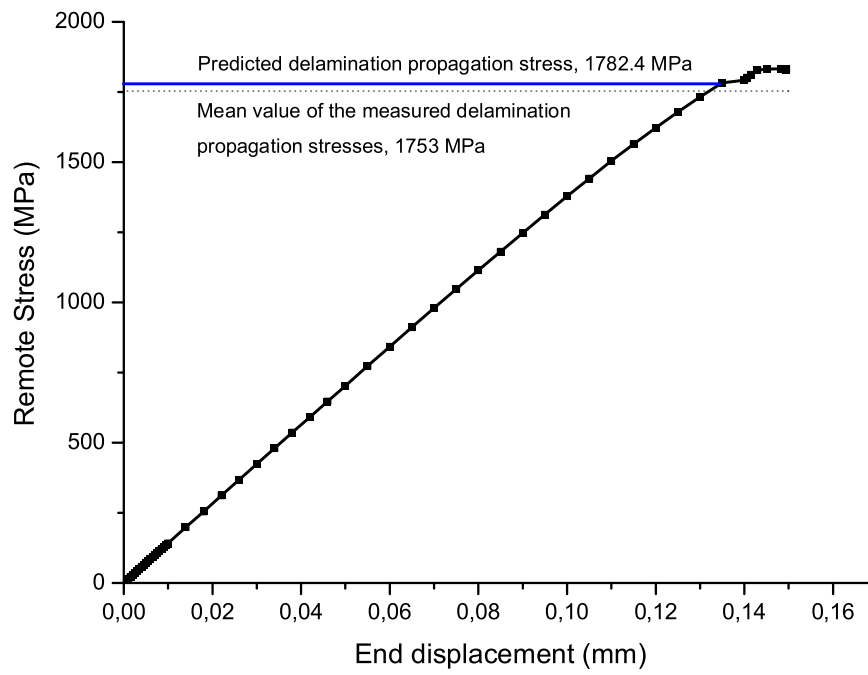


Fig. 18. Predicted relation between the remote stress and the end displacement.

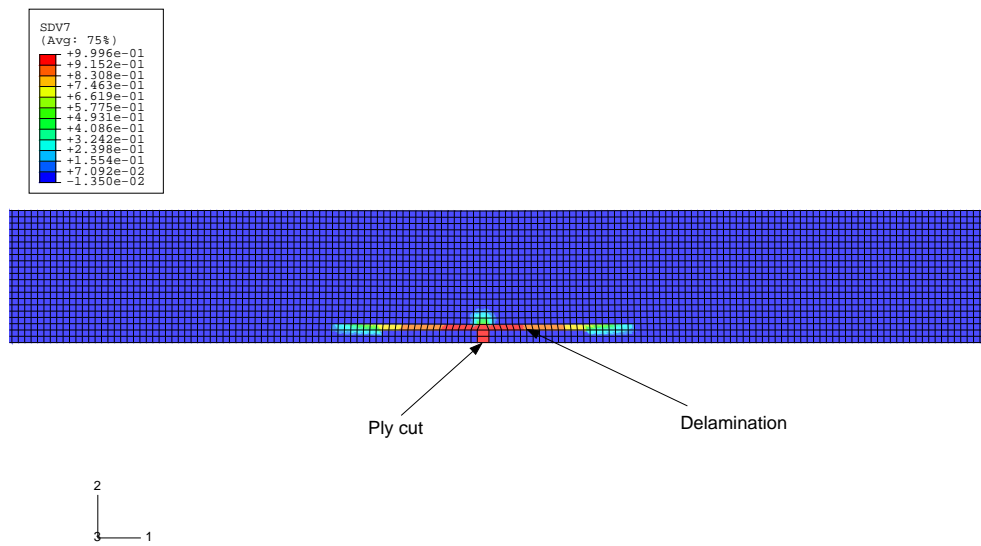


Fig. 19. Damage variable  $d_6$  at 1782.4MPa. Deformed scale: 2x.



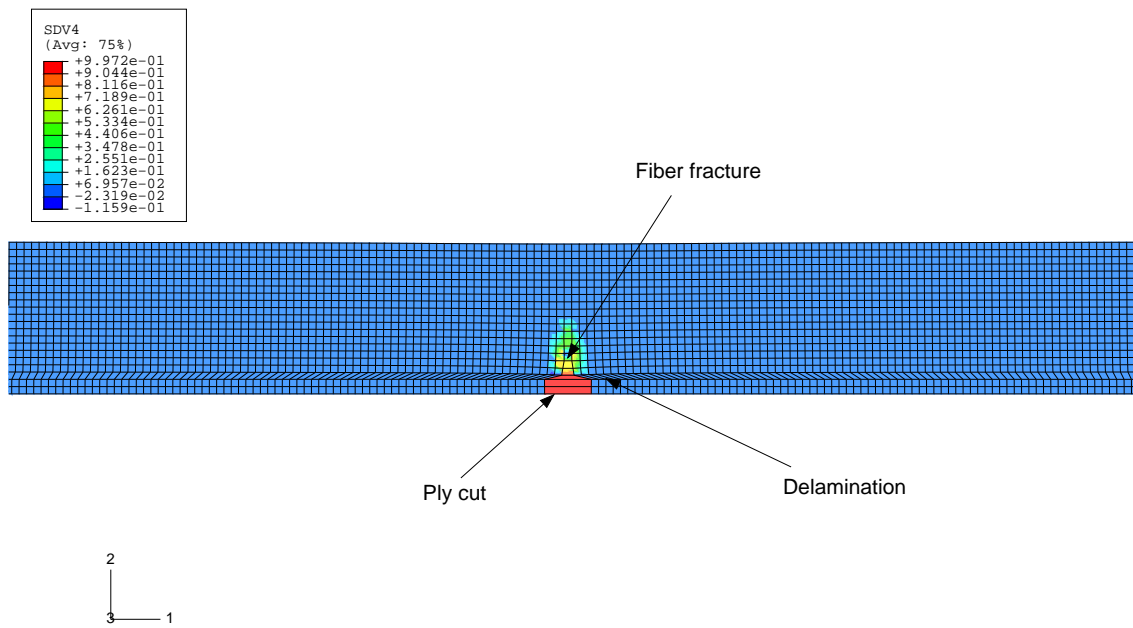


Fig. 20. Damage variable  $d_1$  at peak load, 1829MPa. Deformed scale: 2x.

## List of Tables

1	List of symbols.	47
2	Elastic properties of glass-epoxy [49]-[51].	48
3	Strength and fracture energy of glass-epoxy.	49
4	Elastic properties of 977-2 HTS.	50
5	Strengths and fracture toughness of 977-2 HTS.	51

Table 1  
List of symbols.

$\epsilon_{ij}$	Strain in the material coordinate system.
$\varsigma_{ij}$	Nominal stress in the material coordinate system.
$\varepsilon_{ij}$	Principal strain in the transversely isotropic plane.
$\sigma_{ij}$	Principal nominal stress in the transversely isotropic plane.
$\tilde{\sigma}_{ij}$	Principal effective stress in the transversely isotropic plane.
$\mathbf{T}(\theta)$	Transformation matrix between $\epsilon_{ij}$ and $\varepsilon_{ij}$ .
$\psi$	Complementary free energy per unit volume.
$\Delta T$	Difference in temperature.
$\Delta M$	Difference in moisture content.
$\alpha$	Coefficients of thermal expansion.
$\beta$	Coefficients of hygroscopic expansion.
$d_I$	Active damage variables ( $I = 1, 2, 3, 6$ ).
$d_M$	Damage variables ( $M = L+, L-, T+, T-, S$ ).
$E_1, E_2, G_{12}, \nu_{12}, \nu_{23}$	Ply engineering elastic constants.
$E_x, \nu_{xy}$	Laminate engineering elastic constants.
$\mathbf{H}$	Compliance tensor.
$Y_I$	Thermodynamic forces associated to active damage variable.
$\Xi$	Rate of dissipation.
$F_N$	Damage activation functions ( $N = L+, L-, T$ ).
$\phi_N$	Loading functions ( $N = L+, L-, T$ ).
$r_N$	Elastic domain thresholds ( $N = L+, L-, T$ ).
$X_T, X_C, Y_T, Y_C, S_L$	Uniaxial strengths.
$\ell$	Characteristic element size.
$G_M$	Fracture toughness ( $M = L+, L-, T+, S$ ).
$g_M$	Dissipated energy per unit volume ( $M = L+, L-, T+, S$ ).
$H_{T-}$	Transverse compression damage parameter.
$X_{PO}$	Pull-out strength.
$G_{L+}^E$	Pull-out fracture energy.
$A_L^\pm$	Longitudinal tension-compression coupling parameter.

Table 2

Elastic properties of glass-epoxy [49]-[51].

$E_1$ (MPa)	$E_2$ (MPa)	$G_{12}$ (MPa)	$\nu_{12}$	$\nu_{23}$	$\alpha_{11}$ ( $1/^{\circ}\text{C}$ )	$\alpha_{22}$ ( $1/^{\circ}\text{C}$ )
44730	12760	5800	0.28	0.42	$8.6 \times 10^{-6}$	$22.1 \times 10^{-6}$

Table 3

Strength and fracture energy of glass-epoxy.

$X_T$ (MPa)	$Y_T$ (MPa)	$S_L$ (MPa)	$G_{T+}$ (N/mm)	$G_S$ (N/mm)	$G_{L+}$ (N/mm)
1060	50	72	0.4	0.8	60

Table 4

Elastic properties of 977-2 HTS.

$E_1$ (MPa)	$E_2$ (MPa)	$G_{12}$ (MPa)	$\nu_{12}$	$\nu_{23}$
144000	7500	5030	0.29	0.50

Table 5

Strengths and fracture toughness of 977-2 HTS.

$X_T$ (MPa)	$Y_T$ (MPa)	$S_L$ (MPa)	$G_S$ (N/mm)
2290	47	67	1.55